

Laser Diodes Integrated with Electroabsorption Modulators for 40 Gb/s Data Transmission



Ph.D. Dissertation

accepted by the
Faculty of Engineering Science,
University of Ulm,
Germany

for the degree of
Doktor-Ingenieur (Dr.-Ing.)

by

Dipl.-Ing. Martin Peschke

Dean of Faculty:	Prof. Dr.-Ing. H.-J. Pfeiderer
First Referee:	Prof. Dr. rer. nat. K.-J. Ebeling
Second Referee:	Prof. Dr.-Ing. M.-C. Amann
Submitted on:	October 18 th , 2005
Oral Examination:	March 17 th , 2006

In memory of
Bernhard Stegmüller

Contents

1	Introduction	1
2	Qualitative Approach	4
2.1	Electroabsorption Modulation Basics	4
2.2	Integration Concepts of Laser and Modulator	6
2.3	Material Systems for Communication Application	8
3	Absorption Spectra	11
3.1	Two-Dimensional Electron and Hole States	12
3.2	Analytic Expression for the Absorption Coefficient	14
3.3	Fit Algorithm	18
3.4	Combined Photocurrent and Transmission Measurement	21
3.5	Kramers-Kronig Relation and Chirp Parameter	23
4	Gain Spectra	26
4.1	Quantum Well Gain	27
4.2	Injection and Carrier Transport	30
4.3	Simplified Injection Model for AlGaInAs QWs	32
4.4	Comparison to Broad Area Laser Experiments	36
4.5	Ridge Waveguide Gain Spectra	37
5	Laser Modulator Ridge Waveguides	39
5.1	Fundamentals	41
5.1.1	Scalar Wave Equation	42
5.1.2	Method of Effective Index	43
5.1.3	Confinement Factor	44
5.1.4	Coupled Wave Equation and DFB Spectra	45
5.2	Single-Mode Yield Analysis	49
5.3	Optical Feedback	51
5.3.1	Facet Reflection and Coating	51
5.3.2	Internal Waveguide Reflections	52
5.4	Surface Roughness Scattering	53

6	Design and Fabrication of EMLs with Shared Active Area	55
6.1	Optical Standard	56
6.2	Epitaxial Layer Design	58
6.2.1	EAM Static Figure of Merit	62
6.2.2	Choice of Detuning	63
6.2.3	Epitaxial Layout I: Single QW Type Structure	65
6.2.4	Epitaxial Layout II: Double QW Type Structure	67
6.3	Device Geometry Design	68
6.3.1	Grating Technology	70
6.3.2	Substrate Influence	72
6.3.3	Modulator Section with and without Second Mesa Step	74
6.3.4	Device Geometry Layouts A, B, C and D	75
7	Static Device Performance	76
7.1	Effective Index of Laser Modulator Waveguides	78
7.2	Device A	80
7.3	Device B	80
7.4	Device C	82
7.5	Device D	82
7.6	On-Wafer Testing	83
8	Thermal Properties	85
8.1	Heat Generation in Modulator and Laser	85
8.2	Thermal Crosstalk	87
8.3	Measurement Results	89
8.3.1	Temperature Dependent Absorption Characteristics	89
8.3.2	Thermally Induced Wavelength Shift	90
8.3.3	Enhanced Thermal PI Roll-Over	92
9	Modulation Behavior	93
9.1	Dynamics of the Active Region	94
9.2	Stationary PIN Capacitance	95
9.3	Small Signal Equivalent Circuit Model	97
9.4	Initial Small Signal Measurements	98
9.5	High-Speed Results after Redesign	100
10	Conclusion	101
A	Material Fundamentals	104
A.1	III-V Compound Semiconductors	105
A.2	Strained Semiconductor Layers	106
A.3	Two-Dimensional Electron States	109

A.4	Excitonic Transitions	112
A.5	Determination of QW Composition	114
B	Absorption and Transition Probability	115
C	Method of Finite Differences	118
D	Semiconductor Drift/Diffusion Equations	120
D.1	Unknowns and Boundary Conditions	122
D.2	Layer Dependent Input Parameters	123
D.3	Input Parameters for the whole Structure	124
D.4	Auxiliary Variables	125
D.5	Algorithm	125
E	List of Symbols	126
F	List of Acronyms	133
G	Material Data	135
G.1	InP	135
G.2	GaAs	136
G.3	AlAs	137
G.4	InAs	138
G.5	Bowing Parameter	138
G.6	Material Refractive Indices	139

Chapter 1

Introduction

Due to the ongoing expansion in the data communication market, the demand for high bandwidth applications is ever increasing. Today, this market is about to overtake the classical telecommunication industry. Multimedia applications like music and video on demand or video telephony require data rates in the range of tens of megabits per second (Mbps) at the consumer end. Numerous electrical and optical transceiver systems are struggling to dominate the communication market. Traditional electrical systems like Integrated Services Digital Network (ISDN)¹, Digital Subscriber Line (DSL)² and electrical Ethernet^{3,4} are usually less expensive as their infrastructures are already available, but their physical limitations demand massive error correction measures. Optical solutions like optical Ethernet or fiber to the home have a much better intrinsic bandwidth length product and associated market potential, but their price restricts them to niche markets these days. Cheaper multi-mode technology⁵ limits this benefit and possible applications. Yet, it is not obvious at which bandwidth and link distance the border between electrical and optical solutions will settle. For a breakthrough in the datacom market, inexpensive and reliable optical single-mode products are a must.

Today, there is a variety of optical transmitters available on the market or undergoing research and development. Concerning bandwidth, light emitting diodes (LEDs) are limited to a few hundred megahertz (MHz) [1]. Directly modulated semiconductor lasers such as distributed feedback (DFB) and vertical cavity surface emitting lasers (VCSELs) exceed this value by a factor of ten or more, reaching up to 10 GHz [2, 3, 4]. However, strong chirp and restricted extinction ratio limit the maximum link distance of those devices to approximately 10 km due to dispersion and noise [5]. Long distance and high-end bandwidth applications of 40 GHz and more are dominated by external modulators. In contrast to directly modulated lasers, they can be designed to exhibit both, zero chirp and high extinction ratio. Today,

¹ISDN standard, 128 kbps

²ADSL2+ standard, on telephone cable, 25 Mbps, up to 1 km

³IEEE 802.3ab Ethernet standard, on twisted pair cable category 5, 1 Gbps, up to 100 m

⁴IEEE 802.3an Ethernet standard, on shielded cable category 6, 10 Gbps, up to 100 m

⁵step profile fiber, bit rate length product 50 Mbps·km, gradient profile fiber up to 1 Gbps·km [1]

Mach-Zehnder (MZ) devices [6] are commonly used due to their intrinsic low chirp behavior, optical input power and temperature insensitivity, and the possibility of modulation formats other than amplitude switching.

Another modulator concept is the electroabsorption modulator (EAM) [7, 8]. Here, the optical power is controlled by variable waveguide attenuation rather than the constructive and destructive interference in a MZ device. Besides a small driver voltage swing (1 to 2 V compared to typically 2 to 10 V), EAMs have the potential of reducing production costs by a factor of more than ten compared to conventional MZ modulators. This is due to their very small footprint (100 μm length compared to a few mm), yielding 30 times more devices per wafer, simple device technology and the possibility of monolithic integration with a laser light source. The latter avoids coupling losses, polarization control and sophisticated packaging, which are the predominant expense factors of today's products. On the other hand, absorption modulators suffer from high-temperature sensitivity, a decrease in bandwidth with modulated optical power, and a chirp parameter that is only small for high residual absorption. Integrated devices have to overcome the limitations of optical feedback into the laser and certain design trade-offs depending on the integration principle.

This thesis will evaluate the potential of electroabsorption modulated lasers (EMLs) with the most simple integration concept of a shared active area. Comparable to standard DFB lasers in terms of epitaxy, chip technology and packaging, they have the potential to replace both, directly modulated lasers and MZ modulators, due to a better 10 Gbps performance and lower costs, respectively. Other integration concepts allow for individual optimization of laser and modulator active material and promise much better device performance. However, all such approaches suffer from problems of reliability and production complexity.

Until now, fast EMLs with shared active area were only realized in the GaInAsP on InP material system [9]. For the first time, the integration concept was transferred to the aluminum containing material system AlGaInAs on InP yielding devices capable of 40 Gbps operation. In addition, the very first single growth EMLs including metal grating DFB lasers were manufactured. They have high potential in further reducing chip costs, considerably lowering the production effort by rendering the overgrowth process unnecessary, and boosting the single-mode yield from 20% to 100%.

This advancement was achieved by the implementation of multiple design tools within this thesis. They cover absorption, gain and waveguiding as well as temperature and dynamic modulation behavior. During the development process of the simulation tools, emphasis was put on the incorporation of fast and simple models that are suitable for reproducing measured effects with a high degree of accuracy. For that purpose, every simulation result was carefully compared to experimental findings. In contrast to many commercial all-in-one solutions, this tailored approach enables the identification of predominant mechanisms and target-oriented device design.

The thesis is organized as follows. It starts with a brief overview of the predominant physical mechanisms of semiconductor optical lasers and modulators as well as concepts and material systems for the integration of both devices in Chapter 2. The sequence chosen to analyze the final EML device is to proceed from its intrinsic to its extrinsic parameters. Beginning with basic semiconductor material properties, the interaction of the aluminum containing active QW with light is derived in terms of absorption and gain in Chapters 3 and 4, respectively. Chapter 5 discusses optical waveguides based on the evaluated material. In all three initial chapters, simulation approaches are introduced and confirmed by experiments on individual test structures like vertical incident absorption samples and Fabry-Perot broad area (BA) and ridge waveguide lasers. These simple test devices were manufactured prior to the integrated EMLs. Once the fundamental characteristics are known, design rules for EMLs with shared active area are derived in Chapter 6. The last three Chapters 7, 8 and 9 present experimental results on static, thermal and dynamic properties of EMLs in comparison to previously performed simulations.

Chapter 2

Qualitative Approach

This chapter is intended to give an overview of integrated electroabsorption modulated laser (EML) concepts and their potentials and drawbacks compared to other approaches. It explains physical effects, design challenges and device properties in a qualitative manner.

2.1 Electroabsorption Modulation Basics

Bulk semiconductor electroabsorption modulators (EAMs) make use of the Franz-Keldysh effect [10]. Although polarization independent and temperature stable, it will not be considered here due to its low absorption modulation efficiency with applied bias voltage.

In an active quantum well (QW) area, the fundamental principle of absorption change is the quantum confined Stark effect (QCSE) [11]. It is described in a semi-classical picture in the following paragraph.

Figure 2.1(a) illustrates two particles in a box. The upper is a ball-like electron ($-$), the

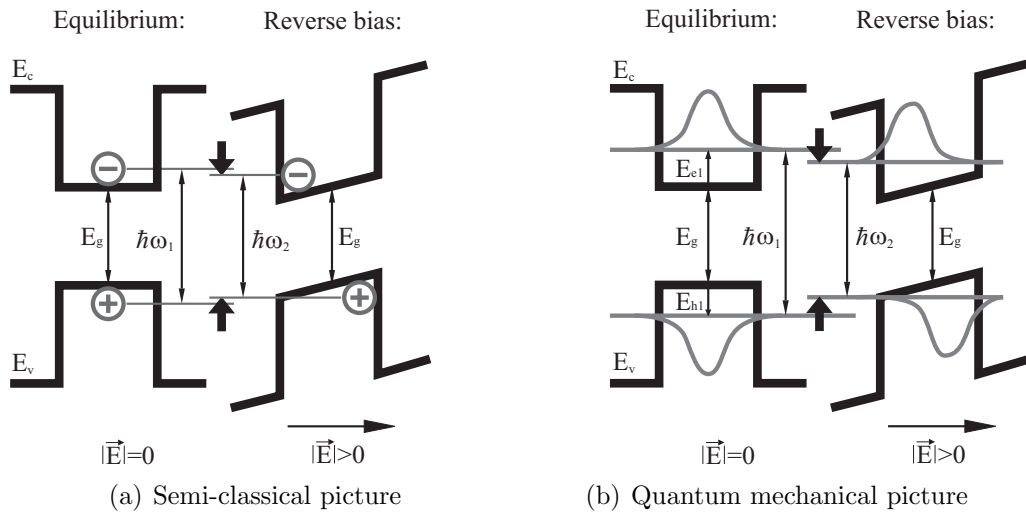


Fig. 2.1: Schematic picture of the quantum confined Stark effect in semi-classical and quantum mechanical view. The confined quantum mechanical particle features discrete energy levels E_{e1} and E_{h1} .

lower a bubble-like hole (+). The energy $\hbar\omega_1$ necessary to lift the lower particle to the position of the upper one is directly proportional to their height difference. This is the minimum photon energy required for an absorption process. Applying an additional linear potential of a constant electric field $|\vec{E}|$ across the boxes, both energy bands are tilted. The particles are spatially separated but move closer to each other in terms of height or energy difference. This happens as balls roll down and bubbles slide up an inclined surface. Now, photons with less energy $\hbar\omega_2$ are sufficient to overcome the gap although the box separation E_g stays constant. The same picture is valid in the quantum mechanical world of Fig. 2.1(b), with ‘balls’ and ‘bubbles’ replaced by wavefunctions and ‘boxes’ by semiconductor QWs in conduction and valence band E_c and E_v , respectively.

A typical absorption characteristic over wavelength for two different bias points is illustrated in Fig. 2.2. Under reverse bias, the absorption edge shifts to longer wavelengths (lower

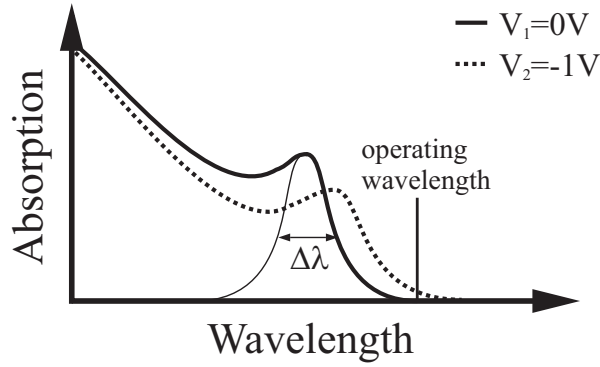


Fig. 2.2: Equilibrium (0 V) and reverse (−1 V) driven absorption spectra of a direct semiconductor QW structure.

energies) as the energy separation between electrons and holes is diminished. Also, the absorption amplitude decreases as the spatial carrier separation lowers the possibility to find electron and hole coinciding as expressed by a reduced wavefunction overlap (Fig. 2.1(b)). The absorption edge is characterized by a sharp peak. It originates from an absorption process with photon energy slightly below the bandgap. This energy is not sufficient for a complete excitation. It creates an exciton composed of an electron and a hole orbiting each other [12]. Similar to a satellite orbiting a planet (or similar to a hydrogen atom), the system’s binding energy is the energy needed to separate the two entities completely. All transitions are blurred by inhomogeneity broadening and Heisenberg’s energy uncertainty principle [13]. The latter relates the range of possible energies ΔE or corresponding wavelengths $\Delta\lambda$ of a quantum mechanical state to its time of occupation Δt by a Fourier transform:

$$\Delta E \Delta t \geq \hbar \quad (2.1)$$

$$\Delta\lambda \propto 1/\Delta t \quad (2.2)$$

High temperatures, weak confinement and strong electric fields shorten the carrier lifetime in the well, degrading the steepness of the absorption edge and resulting in high residual absorption.

Stand-alone EAMs are usually designed to work at an operating wavelength with low residual absorption. Residual absorption not only affects the average output power of an EAM, but also deteriorates its high-speed dynamics in the presence of optical input. In contrast to Mach-Zehnder (MZ) devices that simply vary the refractive index of a waveguide structure, electroabsorption based devices have to address the issue of carriers created during the absorption process. These carriers will remain trapped in the active area if the generation rate is high and the sweeping out electric field is low. The carrier separation of electrons and holes leaving the active area to opposite terminals is equal to the local polarization of electron cloud and atomic core in a dielectric, see Fig. 2.3. They increase the effective permittivity of the switching capacitor and thereby diminish the system's RC bandwidth.

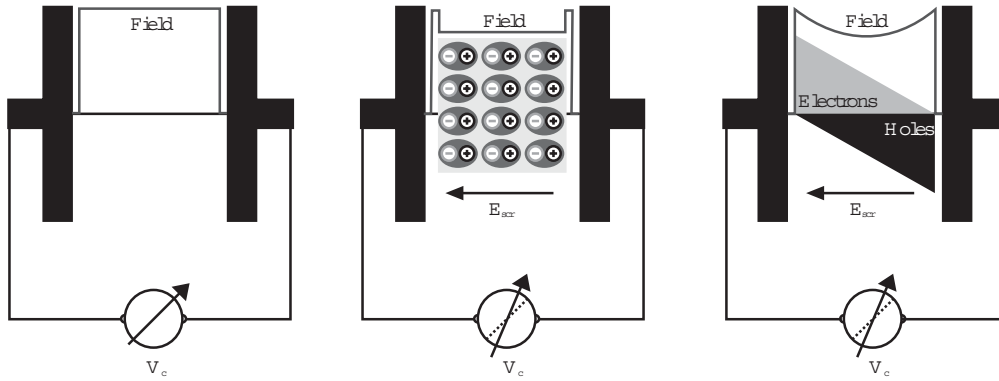


Fig. 2.3: Comparison of a dielectric and a carrier generation process within a capacitor. The first capacitor is empty. The second and third contain a neutral but polarized charge density due to the presence of a dielectric and a carrier generation process, respectively. In both cases, the voltage $V_c = \int |\vec{E}| ds$ across the capacitor decreases and its capacitance $C = Q/V_c$ increases due to a generated screening field.

2.2 Integration Concepts of Laser and Modulator

While the modulator is characterized by the reverse driven active material absorption behavior, a laser relies upon the material gain under current injection. For forward bias, the structure is electrically pumped with carriers, which increases the probability of a photon creating ‘downward’ transition compared to an absorbing ‘upward’ one. The absorption becomes negative and is called optical gain. Figure 2.4 summarizes absorption and gain characteristics of a QW active area. Similar to the case of reverse bias, the gain spectrum is red shifted compared to the equilibrium case, although the cause is quite different. The

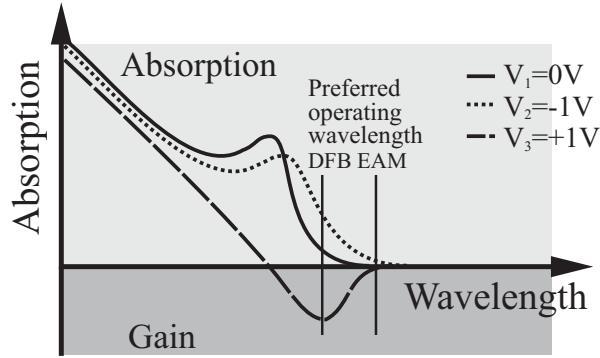


Fig. 2.4: Equilibrium (0 V), reverse (−1 V) and forward (+1 V) driven absorption and gain spectra of a direct semiconductor QW structure.

numerous charged particles screen and weaken the lattice periodic potential of the semiconductor crystal. This is comparable to a semiconductor with lower binding energy, larger lattice constant and smaller energy bandgap.

The figure indicates that the preferred operating wavelengths for distributed feedback (DFB) laser and modulator differ from each other since the former favors high optical gain and the latter low residual absorption. To overcome this restriction, two QWs with different bandgap energies are used in most laser modulator integration schemes. These schemes range from twin guide coupling [14], epitaxial growth on non-planar substrates [15] and QW regrowth [16] to selective area epitaxy [17] and QW intermixing by ion implantation [18]. A schematic of the different integration strategies is given in Fig. 2.5.

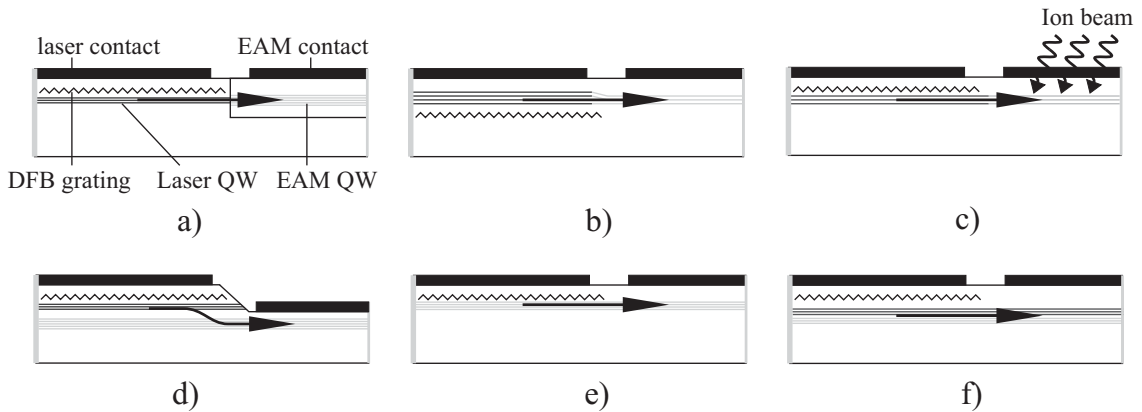


Fig. 2.5: Strategies for laser and EAM integration. (a) QW regrowth, (b) selective area epitaxy, (c) ion implantation and QW intermixing, (d) twin guide coupling, identical active area with single QW type (e) and multi QW stack (f). The arrow indicates the guiding of the optical wave.

Within this work, the most simple approach of an identical active layer throughout all sections is chosen. It may consist of a single [9] or multiple [19] QW types. A top view of the wafer and its corresponding epitaxial layer schematic suitable for all investigated devices

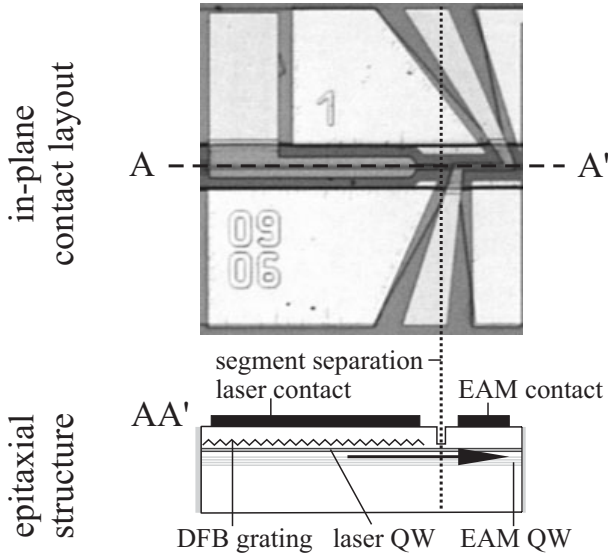


Fig. 2.6: Schematic of the concept of an identical active layer with in-plane device layout (top) and epitaxial layer structure (bottom). The laser contact on the lefthand side is a lumped element contact that is sufficient for direct current (DC) operation. The modulator (right) features a traveling wave contact with tapers and an electrical input and output. The electrical segment separation is an etched trench. The epitaxial layer is common for both sections and may consist of one or two QW types. A local DFB grating is introduced in the laser section.

is given in Fig. 2.6. While all other concepts impose additional stringent requirements on epitaxy and chip technology, the fabrication complexity for EMLs using a shared active area is comparable to that of a standard DFB laser. Furthermore, the coupling efficiency between laser and modulator is high and reproducible. This enables multi-stage integration of additional elements like a semiconductor optical amplifier (SOA).

On the other hand, the QW structures of laser and modulator cannot be optimized individually. A trade-off between optimal laser and modulator performance is necessary. The operating wavelength is limited to a small window in which gain and absorption are sufficient. This in turn restricts the bias voltage at the EAM, limiting its static and dynamic performance under high optical input power.

2.3 Material Systems for Communication Application

Two primary wavelength windows for fiber-optic communication applications are 1310 nm and 1550 nm due to the dispersion and absorption minima in standard single-mode fibers (SSMF), respectively. Semiconductor lasers for these wavelengths are traditionally composed of gallium indium arsenide phosphide (GaInAsP) and, more recently, aluminum gallium indium arsenide (AlGaInAs) on an indium phosphide (InP) substrate [4]¹. The main difference between the two material systems lies in the distribution of conduction and valence band offsets as illustrated in Fig. 2.7(a) [20]. In the phosphorus system, the energy offset of a trapping QW potential is smaller in the conduction band than in the valence band. The opposite is true for the aluminum system for identical bandgap energies of QW and barrier material.

¹Today, GaInNAs on a GaAs substrate is not of interest for EMLs due to the lack of a simple ridge waveguide technology and grating process.

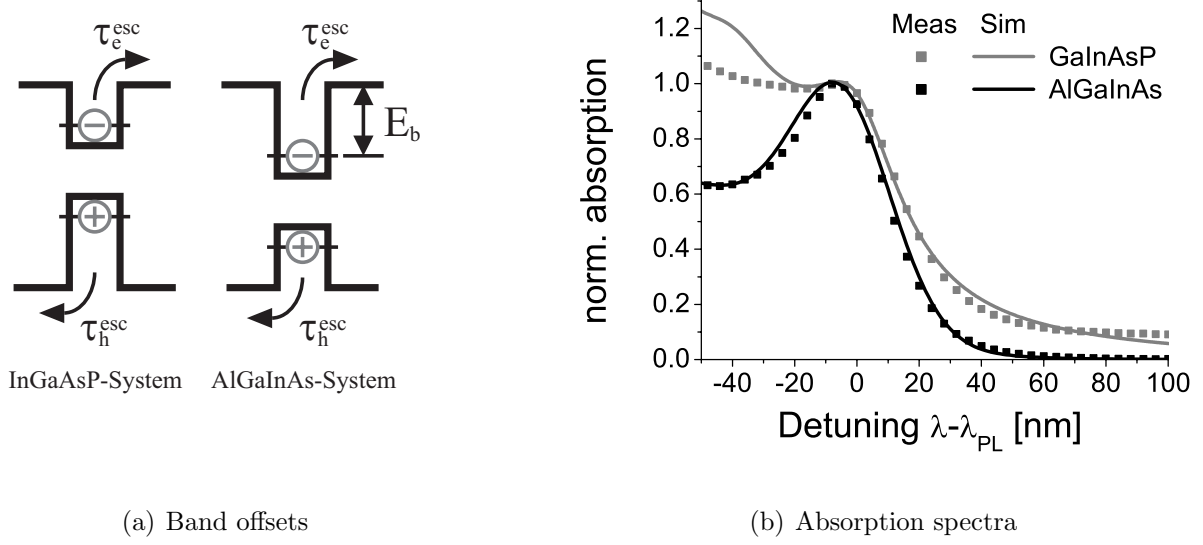


Fig. 2.7: Comparison of aluminum and phosphorus system escape times (a) and measured and simulated residual absorption spectra (b). The carrier ground state is indicated by a horizontal line. Both devices contain a nominal identical active region of 8×5 nm thick QWs.

Captured inside a well, the mass m of a carrier and the energy barrier E_b between its bound and free states determine its thermal escape time constant $\tau^{\text{esc}} \propto \sqrt{m} \exp(E_b/k_B T)$. This carrier lifetime has a profound impact on the sweepout speed and the absorption edge steepness. While the former is obvious, the latter is explained by the linewidth broadening due to Heisenberg's uncertainty relation (2.2). The smaller of the two escape time constants, usually for the lighter electrons, determines the linewidth broadening, whereas the larger one, usually for the heavier holes, limits the sweepout times. The aluminum system ($\tau_e^{\text{esc}} \approx \tau_h^{\text{esc}}$) is superior for both. Its steeper absorption slope is shown in Fig. 2.7(b). It enables higher extinction ratio, less residual absorption and higher optical input power. Another positive feature of the aluminum system is a better epitaxial homogeneity, further increasing the absorption edge slope. Including only one group V element, the epitaxial composition can be better controlled in a group V rich environment [21]. This thesis will theoretically and experimentally investigate if these principle advantages of the aluminum system can be exploited for fabrication of high-speed EML devices.

Concerning forward pumping carrier injection, the impact of escape time constants manifests itself in different carrier distributions among the active QWs. In the phosphorus system, holes are trapped effectively in the QWs on the p-side of the active region and electrostatic forces attract the more mobile electrons. As both escape time constants are approximately equal in the aluminum system, its QWs are pumped homogeneously. The carrier distributions for both systems are compared in Fig. 2.8. Uniform pumping is beneficial for laser active material, as more QWs efficiently contribute to the modal gain. In Fig. 2.8, the average threshold carrier density is much smaller for the aluminum system.

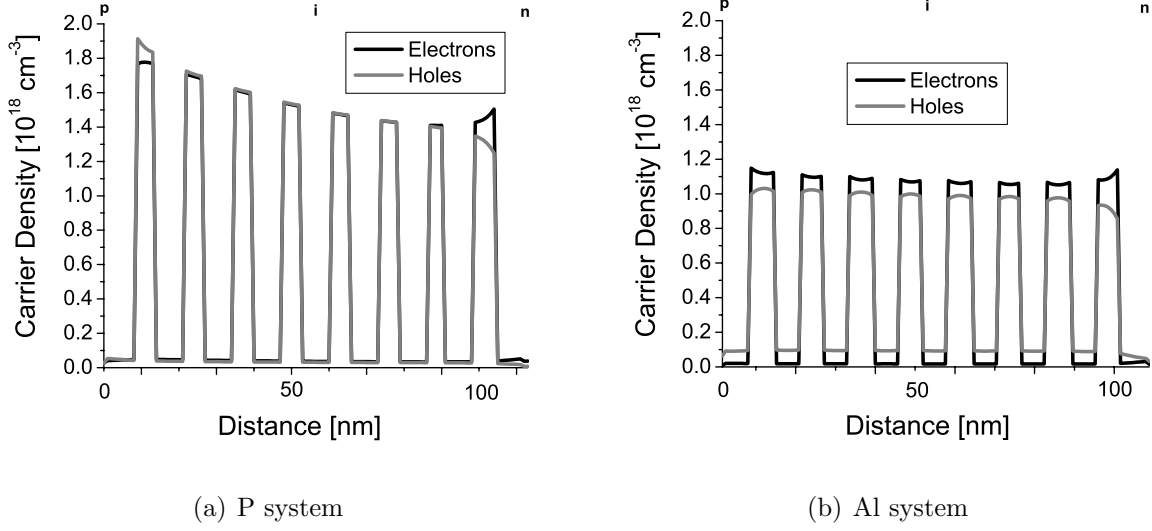


Fig. 2.8: Simulation results on the carrier distribution among 8×5 nm thick QWs and 9×8 nm thick barriers in the phosphorus and aluminum system at laser threshold. Simulation parameters are given in Appendix D.

However, EMLs with identical active area may benefit from non-uniformity when using a double QW type stack. Within this approach, two or three ‘laser’ QWs with lower bandgap are placed on the p-side of the active area. If pumping is strongly inhomogeneous, only these QWs will deliver optical gain, allowing the DFB wavelength to be chosen close to the preferred EAM operation point.

Finally, a general disadvantage of the aluminum system is its affinity for oxidization under atmospheric conditions, imposing challenges on facet coating and mesa etching as well as preventing the intrinsic waveguide region from acting as an etch stop layer. The resulting lateral conductivity can degrade the modulator’s high-speed performance.

Chapter 3

Absorption Spectra

The absorption behavior of the active material is the most essential characteristic of an electroabsorption modulator. Residual absorption in the ON-state and absorption change to the OFF-state determine insertion loss, maximum output power, switching speed and extinction ratio of the device. Due to their unique energy band structure, semiconductors feature a transparent and an absorbing regime for photon energies smaller and larger than the bandgap energy, respectively. For direct semiconductors, the transition between these two regions is very steep. Due to the quantum confined Stark effect (QCSE), the energy position of this absorption edge is shifted by applying an electric field across a quantum well active material. Both, steep slope and field dependent shift, favor direct semiconductors for the fabrication of electroabsorption modulators.

In physical terms, absorption is the destruction of a photon, transferring its energy to an electron and lifting it to a higher energy state. A brief overview of such processes in the quantum mechanical picture is given in Appendix B, providing insight into terms like transition, state overlap or occupation probability. However, these universal equations are not very convenient to use and cannot predict measured absorption spectra quantitatively. This is due to the inclusion of a linewidth broadening term that, besides the particle lifetime, strongly depends on the material quality of the individual production process. Therefore, this term usually has to be fitted to experimental data after each and every measurement, rendering any prediction of absolute absorption figures of future devices impossible [22]. In this work, an *a priori* semi-empirical approach was favored. The idea is to calibrate the absorption expression to a number of test structures once and use these data to predict the absorption spectra of future designs.

In Section 3.2, a simple analytical absorption expression tailored to the specific structures used in this work is presented. This semi-empirical term is derived from the physical model in Appendix B. Emphasis is put on determining linewidth broadening that is matched to experimental data of different epitaxial structures in Section 3.3. After this calibration process, the prediction of quantitative absorption spectra without any further fitting was possible with a high degree of accuracy. This is a necessary prerequisite for the design of electroabsorption modulators.

3.1 Two-Dimensional Electron and Hole States

Figure 3.1 illustrates the energy levels of the band edges along the growth axis z of conduction band E_c and heavy and light hole subbands E_{hh} , E_{lh} , respectively. Energy positions and energy separations of the dominant electron to hole transitions close to the bandgap are included.

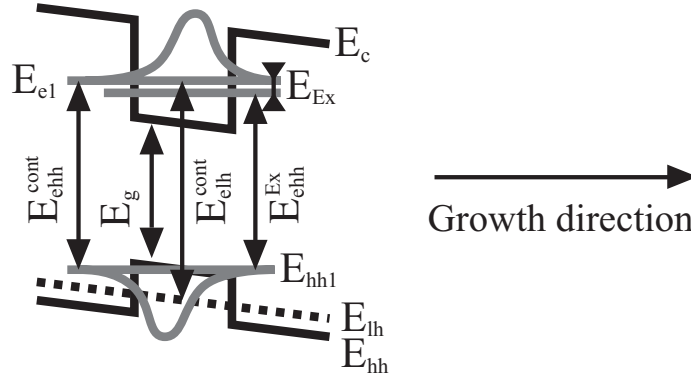


Fig. 3.1: Schematic band diagram showing the energy separations of the three dominant electron to hole transitions close to the bandgap.

For the investigated devices, the composition of the QW layers generates a strong compressive strain. To compensate this strain, barrier layers are chosen to exhibit a comparable amount of tensile strain. This strain configuration increases and decreases the energy levels of the heavy hole subband in QW and barrier, respectively. The light hole subband undergoes a strain induced shift opposite to that of the heavy hole subbands. Thus, the energy offset between QW and barrier is increased for the heavy holes, while it becomes negligible for the light holes.

In a well-designed QW active material, light interaction mainly takes place within the QW layers. The contribution of barrier or cladding layers is usually negligible. In the QW itself, there is a discrete ladder of possible electron and hole energy states¹ due to the well-known particle-in-a-box phenomenon. For the investigated structures, the energy levels of these states are derived in Appendix A. They depend on the bulk material properties of QW and barrier, the layer strain and the internal electric field. Close to the bandgap, the ground states of electron E_{e1} , heavy hole E_{hh1} and light hole $E_{lh1} \approx E_{lh}$ make the predominant absorption contribution. A special feature of most QW absorption characteristics is the presence of an exciton state [12]. Slightly below the electron state and separated by the exciton binding energy E_{Ex} , this transition has the smallest energy separation and dominates the low energy or long wavelength spectral regime. The exciton state is restricted to one discrete energy level. This is in contrast to the continuum states E_{e1} , E_{hh1} and E_{lh1} that actually mark the

¹Strictly speaking, the expression ‘states’ has to be replaced by ‘subbands’ for three-dimensional problems as there exists a dispersion relation for the unconfined movement in the QW layer plane.

energy edge of a whole QW subband due to the quasi-free movement of the particles in the perpendicular QW layer plane.

The energy separations of the three major transitions are identified as the difference between the ground states of electron and heavy hole ($E_{\text{ehh}}^{\text{cont}}$) and electron and light hole ($E_{\text{elh}}^{\text{cont}}$) continuum, respectively, as well as electron and heavy hole ground state exciton ($E_{\text{ehh}}^{\text{Ex}}$). They are referred to as ehk and elh continuum and ehk exciton transition. Appendix A contains a brief overview of the steps to calculate the band structure of III-V compound semiconductors that finally leads to the extraction of these transition energies. For the following chapters, it is more convenient to describe the energy separations in terms of wavelength rather than energy. Both are related by:

$$\lambda_{\text{ehh,elh}}^{\text{Ex,cont}} = \frac{1240 \text{ eV nm}}{E_{\text{ehh,elh}}^{\text{Ex,cont}}} \quad (3.1)$$

$\lambda_{\text{ehh}}^{\text{cont}}$	transition wavelength electron to heavy hole continuum ground state in [nm]
$\lambda_{\text{elh}}^{\text{cont}}$	transition wavelength electron to light hole continuum ground state in [nm]
$\lambda_{\text{ehh}}^{\text{Ex}}$	transition wavelength electron to heavy hole exciton ground state in [nm]
$E_{\text{ehh}}^{\text{cont}}$	transition energy electron to heavy hole continuum ground state in [eV]
$E_{\text{elh}}^{\text{cont}}$	transition energy electron to light hole continuum ground state in [eV]
$E_{\text{ehh}}^{\text{Ex}}$	transition energy electron to heavy hole exciton ground state in [eV]

Figure 3.2 shows the simulated wavelengths of the three dominant transitions for two typical QWs designed for 1310 nm operating wavelength as a function of the internal electric field. Obviously, quadratic fits are a good approximation for all wavelength shifts induced by the QCSE. This behavior is in good agreement with perturbation calculations presented by [12]. As the electric field across the pin-junction increases, the absorption edge shifts to longer wavelengths into the spectral region that was previously transparent. The exciton binding energy is equivalent to the gap between heavy hole continuum and exciton transitions and remains approximately constant for all fields. The red shift in the 7.5 nm QW is stronger since the carrier separation is more efficient for wider wells. Additionally, the figure includes the overlap between the electron and heavy hole ground states that is defined as:

$$| \langle \Psi_e | \Psi_{\text{hh}} \rangle |^2 = \left| \int \Psi_e(z) \Psi_{\text{hh}}(z) dz \right|^2 \quad (3.2)$$

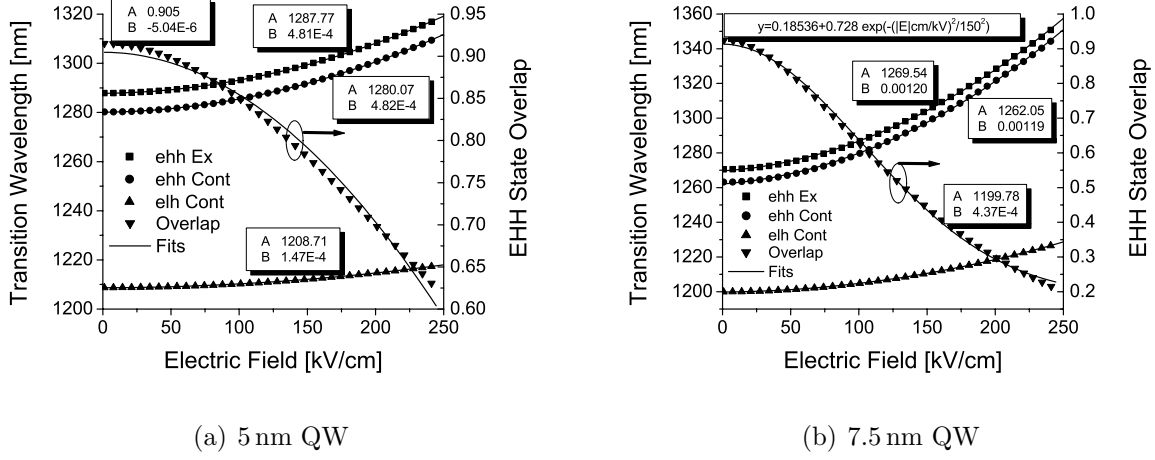


Fig. 3.2: Calculated transition wavelengths and state overlap of two typical QWs. The intrinsic layer stack is $d_{pn} = 300$ nm thick in total and the QW photoluminescence (PL) wavelengths are $\lambda_{PL} = 1290$ nm and 1270 nm, respectively. An equilibrium quantum confined Stark shift due to the $|\vec{E}_{bi}| = 44$ kV/cm built-in pin-junction field is included in the PL wavelengths. The barriers have a PL wavelength of 1100 nm and +0.5% tensile strain compared to -0.95% compressive strain in the wells. Quadratic fits are included for reproduction purpose:

$$\lambda_{ehh,elh}^{Ex,cont} = A \text{ nm} + B \left(|\vec{E}| \frac{\text{cm}}{\text{kV}} \right)^2 \text{ nm} \quad \text{and} \quad |\langle \Psi_e | \Psi_{hh} \rangle|^2 = A + B \left(|\vec{E}| \frac{\text{cm}}{\text{kV}} \right)^2.$$

$\Psi_e(z)$	electron envelope function in growth direction, 1D in $[\text{m}^{-\frac{1}{2}}]$
$\Psi_{hh}(z)$	heavy hole envelope function in growth direction, 1D in $[\text{m}^{-\frac{1}{2}}]$

As detailed knowledge of particle wavefunctions is not necessary to understand the principle of absorption modulation, they are treated in Appendix A.3. At this point, it is sufficient to know that an electric field across the QW tears the two particles apart due to their opposite electric charges. This manifests itself in a reduced wavefunction overlap. In the 7.5 nm QW, the overlap diminishes faster since the carrier separation is more efficient for wider wells. Figure 3.3 illustrates electron and heavy hole ground state envelope functions calculated according to Appendix A.3 for various external voltages.

3.2 Analytic Expression for the Absorption Coefficient

In the last section, transition wavelengths and envelope wavefunction overlaps of the ground states were derived for two typical QWs used in integrated laser modulators. According to semiconductor theory [12], the total semiconductor absorption spectrum is composed of the contributions of these individual transitions, each with a spectral position determined by its transition wavelength and an amplitude proportional to its wavefunction overlap. Finally, every transition has a spectral shape that is governed by the spatial dimensionality of its

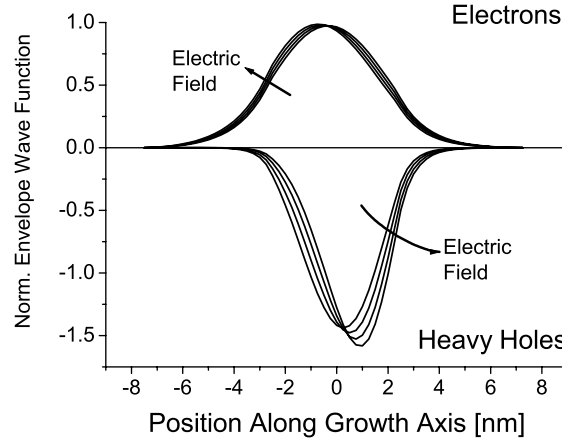


Fig. 3.3: Calculated envelope wavefunctions for the electron and heavy hole (here with negative sign) ground states of the QW introduced in Fig.3.2(a) for 44, 77, 110 and 143 kV/cm internal electric field corresponding to 0, 1, 2 and 3 V external voltage across a 300 nm thick intrinsic layer stack in a highly doped InP pin-junction.

initial and final state and a broadening term. A rigorous derivation of absorption spectra in terms of quantum mechanics is found in Appendix B. The absorption profile for 0D transitions, as is the case for an exciton, is a sharp peak while for a 2D continuum transition it resembles a step-like function. This is explained by the fact that 0D transitions have a discrete final energy state rather than an energy subband with a continuum of states above the subband edge energy. Exemplary absorption spectra are shown in Fig.3.4 as a function of both, energy and wavelength. Table 3.1 lists the corresponding nomenclature.

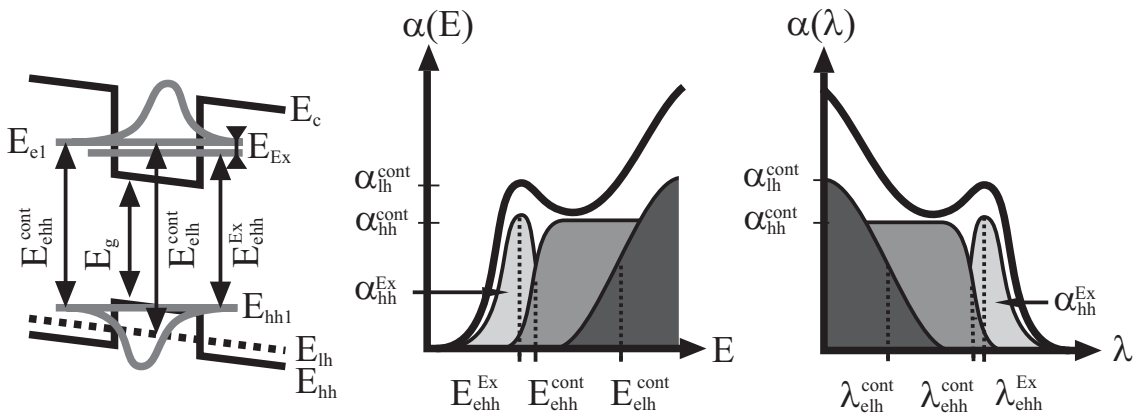


Fig. 3.4: Schematic of the absorption contribution of the three major transitions and the resulting absorption spectrum as a function of energy E and wavelength λ .

The figure indicates that the absorption spectra are expected to feature a relatively sharp peak between the absorbing and transparent spectral regimes. This peak originates from the excitonic transition that is closest to the bandgap. It is followed by a gentle ascent due to

Transition	Transition energy difference	Transition wavelength	Absorption amplitude	Linewidth broadening
Electron to heavy hole 2D ground states	$E_{\text{ehh}}^{\text{cont}} = E_g + E_{\text{e1}} - E_{\text{hh1}}$	$\lambda_{\text{ehh}}^{\text{cont}}$	α_{HH}	$\Delta\lambda_{\text{ehh}}^{\text{cont}}$
Electron to heavy hole 1S exciton state	$E_{\text{ehh}}^{\text{Ex}} = E_g + E_{\text{e1}} - E_{\text{hh1}} + E_{\text{Ex}}$	$\lambda_{\text{ehh}}^{\text{Ex}}$	α_{EX}	$\Delta\lambda_{\text{ehh}}^{\text{Ex}}$
Electron to light hole ground states	$E_{\text{elh}}^{\text{cont}} = E_g + E_{\text{e1}} - E_{\text{lh}}$	$\lambda_{\text{elh}}^{\text{cont}}$	α_{LH}	$\Delta\lambda_{\text{elh}}^{\text{cont}}$

Tab. 3.1: Nomenclature of the three major transitions.

the superposition of the step-like contributions of the electron to heavy hole and electron to light hole continua.

Even with very sophisticated calculations, it is not possible to determine the exact spectral shape of the transitions including a broadening term. This is due to the fact that, in addition to a variety of contributions, linewidth broadening depends on data that are difficult to measure, such as material and surface quality and homogeneity. A practical approach is to choose an appropriate expression by comparison to experimental absorption spectra. The following equation (3.3) was assumed:

$$\alpha(\lambda) = \alpha_0 \left[\frac{\alpha_{\text{HH}}}{1 + \exp\left(\frac{\lambda - \lambda_{\text{ehh}}^{\text{cont}}}{\Delta\lambda_{\text{ehh}}^{\text{cont}}}\right)} + \frac{\alpha_{\text{LH}}}{1 + \exp\left(\frac{\lambda - \lambda_{\text{elh}}^{\text{cont}}}{\Delta\lambda_{\text{elh}}^{\text{cont}}}\right)} + \alpha_{\text{EX}} \exp\left[-\frac{1}{2} \left(\frac{\lambda - \lambda_{\text{ehh}}^{\text{Ex}}}{\Delta\lambda_{\text{ehh}}^{\text{Ex}}}\right)^2\right] \right] \quad (3.3)$$

$$\alpha_0 = C_0 M_b^2 \frac{1}{\pi \hbar^2 d_{\text{QW}}} \frac{3}{2} m_{\text{ehh}}^r = 7.8 \cdot 10^3 \frac{1}{\text{cm}} \cdot \frac{5 \text{ nm}}{d_{\text{QW}}} \quad (3.4)$$

$\lambda_{\text{ehh}}^{\text{cont}}, \lambda_{\text{elh}}^{\text{cont}}, \lambda_{\text{ehh}}^{\text{Ex}}$	transition wavelengths in [nm]
$\Delta\lambda_{\text{ehh}}^{\text{cont}}, \Delta\lambda_{\text{elh}}^{\text{cont}}, \Delta\lambda_{\text{ehh}}^{\text{Ex}}$	linewidth broadening in [nm]
$\alpha_{\text{HH}}, \alpha_{\text{LH}}, \alpha_{\text{EX}}$	relative absorption amplitudes, no [unit]
α_0	absorption amplitude in [cm^{-1}], summary of equations (B.4) to (B.6)
d_{QW}	QW width in [nm]

The analytic expression includes broadening in terms of a Gaussian exciton function and a Fermi-like continuum step [23], which itself is similar to the convolution of a step-like function and a Gaussian pulse. The Gaussian line shape functions represent a statistical process indicating that broadening is mainly due to inhomogeneity of the epitaxial layers. Thermal broadening is weak due to the strong electron confinement in the aluminum containing material system. The absorption amplitude of equation (3.4) contains fundamental physical and semiconductor specific constants explained in Appendix B. Note that the expression is only

valid under the assumption of low excitation. In this case, the bands are not occupied by free carriers.

In contrast to the implicit convolution broadening terms presented in many literature sources [12], the explicit absorption expression is very convenient in use. Figure 3.5 proves that it fits the experimental data perfectly with $\Delta\lambda_{\text{ehh}}^{\text{cont}}$, $\Delta\lambda_{\text{elh}}^{\text{cont}}$, $\Delta\lambda_{\text{ehh}}^{\text{Ex}}$, α_{EX} and α_{LH} as independent fit parameters. Transition wavelengths $\lambda_{\text{ehh}}^{\text{cont}}$, $\lambda_{\text{ehh}}^{\text{Ex}}$ and $\lambda_{\text{elh}}^{\text{cont}}$ and absorption amplitude α_{HH} are simulated according to Appendices A and B. It should be mentioned that the absorp-

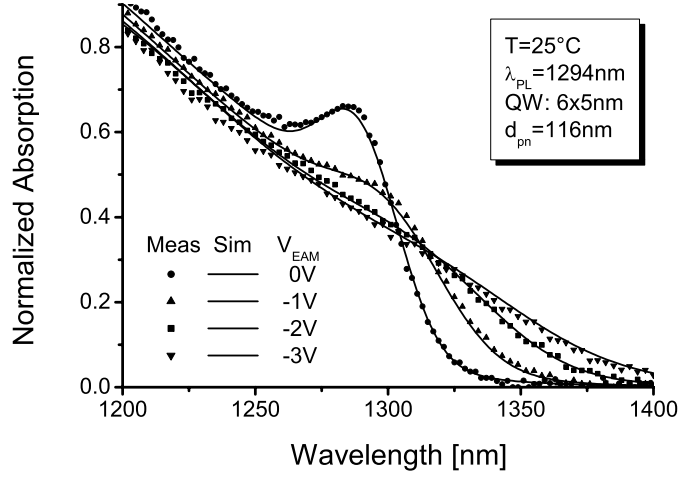


Fig. 3.5: Calculated spectra according to equation (3.3) with independent parameters α_{LH} , α_{EX} , $\Delta\lambda_{\text{ehh}}^{\text{cont}}$, $\Delta\lambda_{\text{elh}}^{\text{cont}}$, $\Delta\lambda_{\text{ehh}}^{\text{Ex}}$ in comparison to experimental results.

tion amplitudes for ehh exciton and elh continuum given by semiconductor theory did not yield satisfactory results to explain experimental observations. As the aim of the thesis is to provide a quantitative optimization tool, an empirical approach was favored.

Although equation (3.3) satisfactorily explains absorption spectra, fitting the parameters independently after every measurement is not a practical method for the prediction of absorption spectra in the modulator design process. A relation between linewidth broadening and data available from the QW simulation, such as state overlap or electric field, has to be identified. It must be suitable for various test structures containing QWs differing in number, thickness and photoluminescence (PL) wavelength and for a wide range of applied voltages. This ‘Fit Algorithm’ is presented in the following section. Once calibrated, it will predict absorption spectra without any further measurement input.

3.3 Fit Algorithm

The last section proved that the spectral shape of the proposed absorption expression will be in good agreement with the experimental results if the broadening and amplitude parameters are calibrated individually for each and every epitaxial structure and bias point. Now, an algorithm must be developed that identifies a physical relation between these parameters and data available from the QW calculation.

The method is sketched in Fig. 3.6. Prior to execution, a variety of absorption measurements

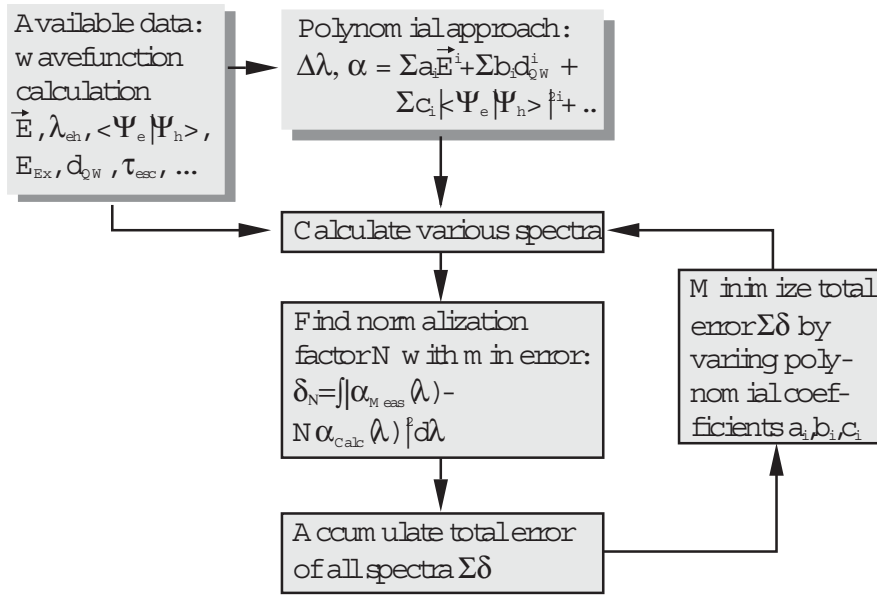


Fig. 3.6: Fit algorithm.

were performed on different test structures. The four devices cover a wide range of QW designs ranging from six to ten QWs, 5 nm to 7.5 nm QW widths and 1273 nm to 1297 nm PL wavelengths embedded in 116 nm to 192 nm intrinsic layer stacks. Each structure was biased with 0, −1 and −2 V. This is equivalent to a total number of twelve experimental absorption spectra under different conditions.

The basic idea of the Fit Algorithm is to start with a Taylor expansion for the $\Delta\lambda$ and α terms as a function of electric field, QW width, state overlap and other parameters:

$$\Delta\lambda_i, \alpha_i = \sum_i \hat{a}_i |\vec{E}|^i + \sum_i \hat{b}_i d_{QW}^i + \sum_i \hat{c}_i |<\Psi_e|\Psi_e>|^{2i} + \dots \quad (3.5)$$

$\hat{a}_i, \hat{b}_i, \hat{c}_i$ polynomial coefficients, different for each $\Delta\lambda$ and α , fit parameters

In the following sequence, \hat{a} , \hat{b} and \hat{c} parameters are determined using a fitting process. The aim is an optimal reproduction of all twelve experiments with a constant set of coefficients. Rather than calibrating each experiment with individual $\Delta\lambda$ values, a general relation is derived that can be interpolated to yield consistent results for unknown structures. Thus, a prediction of absorption spectra is possible for future devices that fall within the range covered by the test devices once the polynomial coefficients are known.

The Fit Algorithm starts with a good initial guess for the \hat{a} , \hat{b} and \hat{c} coefficients and features two loops. In the outer loop, the polynomial coefficients are varied until the integrated and accumulated error between theoretical and experimental graphs is minimal for all test devices and bias voltages. This error is defined as:

$$\delta(\hat{a}_i, \hat{b}_i, \hat{c}_i) = \sum_{12 \text{ experiments}} \int |\alpha_{\text{meas}}(\lambda) - N \alpha_{\text{calc}}(\lambda, \hat{a}_i, \hat{b}_i, \hat{c}_i)|^2 d\lambda \quad (3.6)$$

δ	total square error
$\alpha_{\text{meas}}(\lambda)$	experimental absorption characteristic
$\alpha_{\text{calc}}(\lambda)$	corresponding calculated absorption characteristic
N	normalization factor

Obviously, the total square error δ depends on the choice of the coefficients \hat{a} , \hat{b} and \hat{c} . A practical problem of the routine is a tendency toward chaotic behavior if the amplitudes of calculated and measured spectra do not agree. For instance, infinite linewidths will occur if the algorithm tries to fit different absolute figures by increasing the linewidth broadening. Thus, in every iteration an inner normalization routine is included that determines an optimal normalization factor N .

The Fit Algorithm result is a simple relation between linewidth broadening, electric field and QW width as well as a simple relation between absorption amplitude and state overlap. All other polynomial coefficients are approximately zero.

$$\Delta\lambda_{\text{ehh}}^{\text{cont}} / \text{nm} = 4.453 + 0.0688 \cdot |\vec{E}| \frac{\text{cm}}{\text{kV}} \quad (3.7)$$

$$\Delta\lambda_{\text{ehh}}^{\text{Ex}} / \text{nm} = 4.453 + 0.0688 \cdot |\vec{E}| \frac{\text{cm}}{\text{kV}} + 0.58864 \cdot \frac{d_{\text{QW}}}{\text{nm}} \quad (3.8)$$

$$\Delta\lambda_{\text{elh}}^{\text{cont}} / \text{nm} = 30.21 + 0.04136 \cdot |\vec{E}| \frac{\text{cm}}{\text{kV}} \quad (3.9)$$

$$\alpha_{\text{HH}} = |\langle \Psi_e | \Psi_{\text{hh}} \rangle|^2 \quad (3.10)$$

$$\alpha_{\text{LH}} = 1.7706 \quad (3.11)$$

$$\alpha_{\text{EX}} = 16.6625 \cdot |\langle \Psi_e | \Psi_{\text{lh}} \rangle|^4 / (\Delta\lambda_{\text{ehh}}^{\text{Ex}} / \text{nm}) \quad (3.12)$$

Equations (3.7) to (3.9) indicate that a stronger internal electric field results in enhanced linewidth broadening. This accounts for the fact that the field efficiently separates the carriers, enhancing QW escape processes and shortening the carrier lifetime in the well. The exciton linewidth additionally depends on the QW width. A narrow QW stabilizes the exciton by confining the two carriers close to each other. Without this stabilization, the exciton is destroyed rapidly by thermal forces and appears extremely broadened. Thus, excitons are usually not observed in bulk materials at room temperature. The relative electron to heavy hole continuum amplitude equals the state overlap as predicted by theory. The exciton strength expression includes the oscillator strength model.

Experimental and simulated graphs for all test devices are plotted in Fig. 3.7 (with normalization factor $N = 1$).

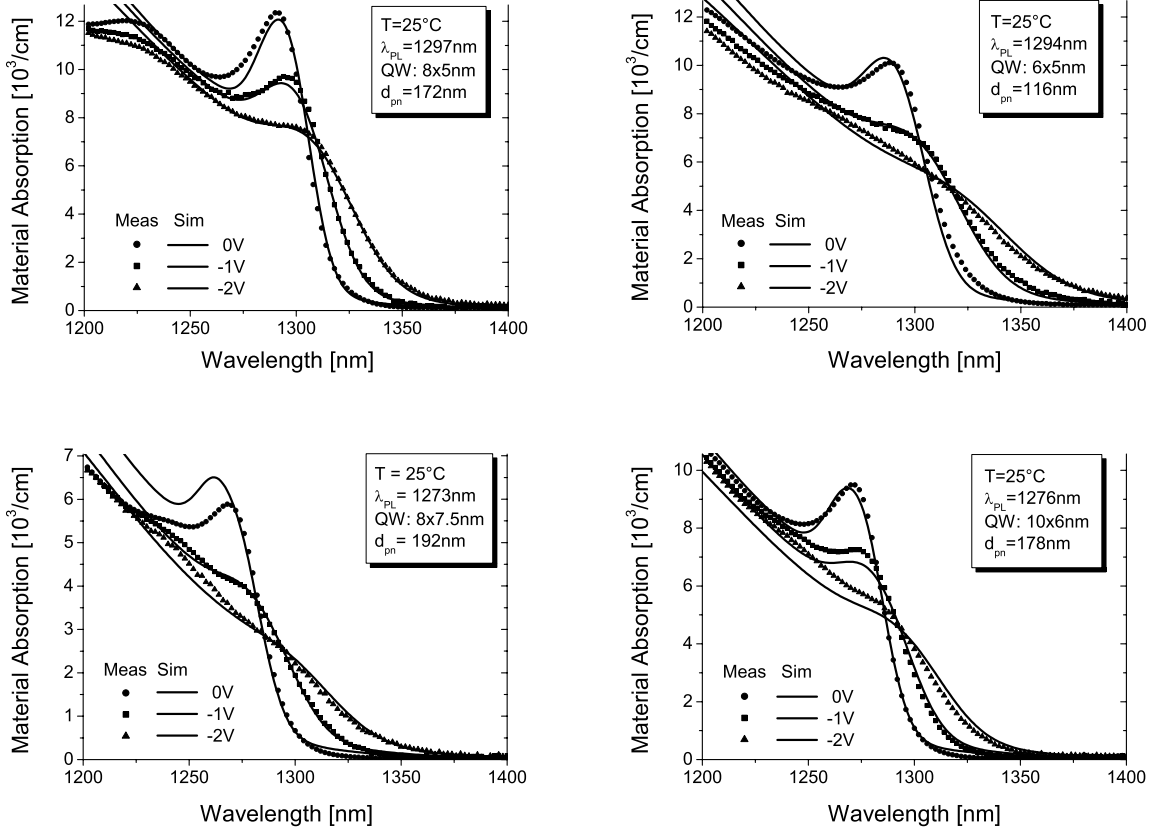


Fig. 3.7: Experimental and calibrated simulation results of the Fit Algorithm for various bias voltages V_{EAM} . All QWs are -0.95% compressively strained, all barriers are 8 nm thick, have a PL wavelength of 1100 nm and are 0.5% tensile strained.

All devices show a steep absorption slope at the band edge that favors the performance of integrated EMLs with common active layer and limited detuning. Without bias voltage, samples with thick intrinsic layers show a steeper absorption slope due to their weaker built-in equilibrium field. As predicted by Fig. 3.2, the 7.5 nm thick QW exhibits a stronger band edge shift, but at the same time a faster decrease in absorption amplitude proportional to the faster decrease in the ground state overlap with applied electric field.

As predicted by theory, the amplitude of the material absorption coefficient, for example at the exciton peak, is inversely proportional to the QW thickness. However, the light interaction length or the QW confinement factor are directly proportional to its thickness for vertical light incident or guided waves, respectively. Thus, the absolute light absorption of a QW transition does *not* depend on the thickness of the QW!

In the following chapters, the calibrated absorption expression will be used to predict optimal QW structures and identify design rules for integrated EMLs.

3.4 Combined Photocurrent and Transmission Measurement

The last section featured several experimental graphs to calibrate the analytic absorption expression. These spectral absorption characteristics were obtained on large-area test devices with light incident perpendicular to the wafer surface. Thus, no waveguide coupling is needed, avoiding sophisticated coupling optics and excluding any uncertainty of fiber coupling efficiency. On the other hand, the interaction length is short, usually in the range of 30 nm to 100 nm, and light absorption is low. In principle, there are two experimental approaches available. The transmission method yields the change in optical power P_{out} transmitted for different bias voltages directly. The photocurrent method extracts the absorption coefficient from the current I_{ph} flowing in the test structure. The basic equations for both techniques are:

Transmission:

$$P_{\text{out}}(\lambda, V) = P_{\text{in}}(\lambda) \cdot e^{-\alpha_{\text{SUB}}(\lambda)d_{\text{SUB}}} \cdot e^{-\alpha(\lambda, V)d_{\text{QW}}} \quad (3.13)$$

$$\Delta\alpha(\lambda, V_1, V_2)d_{\text{QW}} = [\alpha(\lambda, V_2) - \alpha(\lambda, V_1)]d_{\text{QW}} \approx 1 - \frac{P_{\text{out}}(\lambda, V_2)}{P_{\text{out}}(\lambda, V_1)} \quad (3.14)$$

Photocurrent:

$$P_{\text{abs}}(\lambda, V) = \frac{\hbar\omega}{e} \frac{1}{\eta_i} I_{\text{ph}}(\lambda, V) = P_{\text{in}}(\lambda) (1 - e^{-\alpha(\lambda, V)d_{\text{QW}}}) \quad (3.15)$$

$$\alpha(\lambda, V)d_{\text{QW}} \approx \frac{\hbar\omega}{e} \frac{1}{\eta_i P_{\text{in}}(\lambda)} I_{\text{ph}}(\lambda, V) \quad (3.16)$$

I_{ph}	photocurrent of absorption sample in [A]
$P_{\text{in}}, P_{\text{out}}$	incident and transmitted optical power in [W]
$\hbar\omega/e$	conversion to energy, $=1240 \frac{\text{W nm}}{\text{A}} \frac{1}{\lambda} \approx 0.95 \frac{\text{W}}{\text{A}}$ for 1310 nm wavelength
η_i	absorption process internal quantum efficiency, ≈ 1

The Taylor expansion $e^x \approx 1 + x$ valid for short absorption lengths has been used. Both methods possess certain advantages and disadvantages summarized in Table 3.2. The photocurrent measurement determines the absorption coefficient α directly, whereas the transmission method only accounts for absorption changes $\Delta\alpha$ as the substrate contribution α_{SUB} is usually unknown. On the other hand, the transmission method enables complete calibration of the setup and yields the absorption change in absolute figures. The photocurrent measurement always includes an unknown internal quantum efficiency η_i of the absorption process, representing the fraction of absorbed photons and electron hole pairs leaving the active area without prior recombination.

Transmission	Photocurrent
$\Delta\alpha(\lambda, V_1, V_2) d_{\text{QW}} \approx 1 - \frac{P_{\text{out}}(\lambda, V_2)}{P_{\text{out}}(\lambda, V_1)}$	$\alpha(\lambda, V) d_{\text{QW}} \approx \frac{\hbar\omega}{e} \frac{1}{\eta_i P_{\text{in}}(\lambda)} I_{\text{ph}}(\lambda, V)$
(-) includes unknown substrate contribution when absolute values are measured	(+) only contributions of absorption in intrinsic area
(-) only absorption changes $\Delta\alpha$ between two voltages (substrate contribution constant) measured reliably	(+) absorption measured directly
(+) $\Delta\alpha$ measurement in absolute figures	(-) includes unknown quantum efficiency η_i , only ratios are measured
(+) all disturbances (lamp, monochromator, lens, mirror and detector spectra, surface and multiple reflections) are calibrated	(-) absolute setup calibration ($P_{\text{in}}(\lambda)$) with standard detector necessary; detector sensitivity must be known
(+) good signal to noise ratio (SNR)	(-) small photocurrents for vertical measurement, low SNR, leakage current problem

Tab. 3.2: Comparison of both measurement methods for determination of absorption coefficient or field induced absorption change.

The very effective solution to this problem performed in this thesis is the combination of both methods in one setup. Photocurrent and transmission are measured simultaneously during the wavelength sweep. By comparison of the directly measured absolute absorption change using the transmission method and the absorption change calculated from two photocurrent graphs for different voltages, the photocurrent response is calibrated. Figure 3.8(b) depicts

the superimposed experimental results of both approaches. Depending on the device, the resulting internal quantum efficiency of the absorption process η_i was between 0.8 and 1 and usually close to unity. The absorption coefficient is now available in absolute figures.

Figure 3.8(a) outlines the whole measurement setup. Light is emitted from a white light source and a particular wavelength is selected by a monochromator grating. To eliminate the influence of the ambient light, the incident beam is chopped at a certain frequency that is detected by a lock-in amplifier. The photocurrent generated in the device under test (DUT) is monitored as well as the transmitted optical power. The bias voltage is applied using a bias-T. As neither the light source intensity nor the monochromator filtering or the light path are wavelength independent, a setup calibration is mandatory prior to performing the measurements. The sample is anti-reflection coated on both facets to avoid multiple reflections and Fabry-Perot modes.

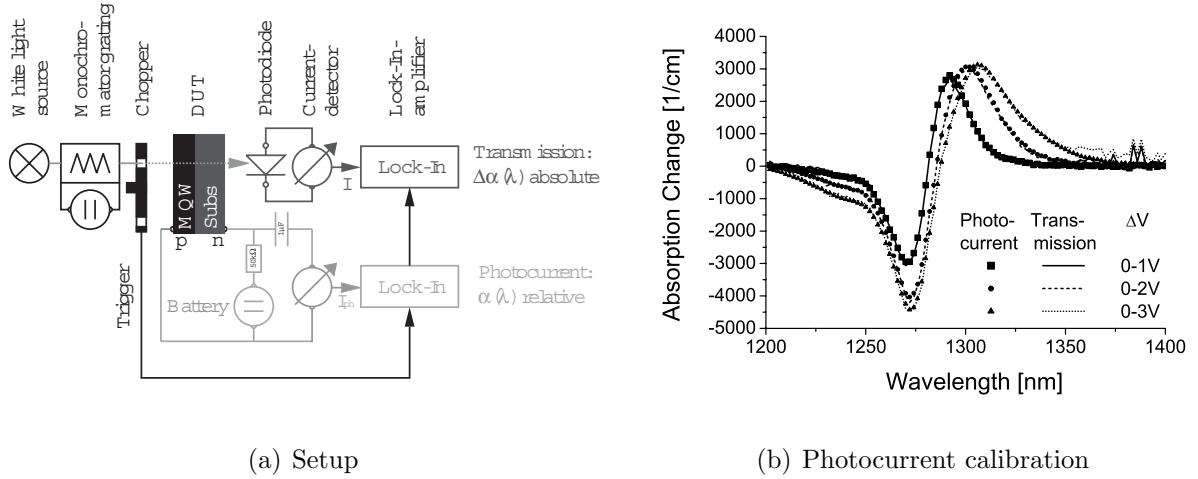


Fig. 3.8: Transmission and photocurrent measurement. The absorption change is depicted for both methods and different voltage swings ΔV . The device consists of 10×5 nm thick, -0.95% compressively strained QWs with a PL wavelength of 1280 nm. The intrinsic layer stack is 300 nm thick.

3.5 Kramers-Kronig Relation and Chirp Parameter

In every material, the real and imaginary parts of the refractive index are coupled via the Kramers-Kronig relation. The ratio of real to imaginary index change is defined as the chirp parameter α_H . A change in absorption or gain is always accompanied by a corresponding change in refractive index. Or in other words, with every amplitude modulation there is phase or frequency modulation. Both frequency and phase modulation create additional frequencies in the optical spectrum. In general, an optical pulse is subject to additional broadening along a dispersive link where every frequency has its own propagation velocity. A higher positive chirp parameter degrades this behavior on a standard single-mode fiber.

The Kramers-Kronig relation is derived from basic mathematics considering an infinite integral path along the holomorphic complex function $\varepsilon_r + i\varepsilon_i$ [12]:

$$\Delta n_r(\lambda) = \frac{\lambda^2}{2\pi^2} \mathcal{P} \int_0^\infty \frac{\Delta\alpha(\lambda')}{\lambda^2 - \lambda'^2} d\lambda' \quad (3.17)$$

Δn_r	(material) real refractive index change, maximum $\approx 0.02/\text{V}$
$\mathcal{P} \int f(x, x') dx'$	Cauchy principal value, $= \lim_{\epsilon \rightarrow 0} \left(\int_{-\infty}^{x-\epsilon} f(x, x') dx' + \int_{x+\epsilon}^{\infty} f(x, x') dx' \right)$

A typical Kramers-Kronig result is given in Fig. 3.9. The refractive index change is negative at the exciton peak, zero close to the bandgap and positive in the long wavelength regime where the residual absorption approaches zero.

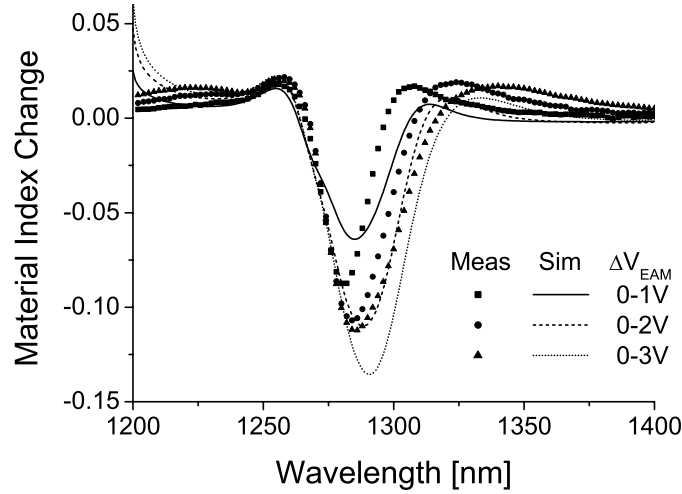


Fig. 3.9: Kramers-Kronig calculations of simulated and measured absorption spectra for the absorption changes presented in Fig. 3.8(b).

The Henry factor or chirp parameter α_H is defined as [10]

$$\alpha_H = \frac{\Delta n_r}{\Delta n_i} = \frac{4\pi}{\lambda} \frac{\Delta n_r}{\Delta\alpha} \quad (3.18)$$

Figure 3.10 shows a chirp parameter calculation. The parameter lies between -2 and $+2$ in the typical operation regime between 1300 nm and 1310 nm wavelength. Fabry-Perot interferometer measurements show a time resolved chirp parameter of approximately $+0.4$ for $V_{pp}=2\text{ V}$ driver voltage swing and $V_{EAM} = -1.1\text{ V}$ bias (i.e. modulation between 0.1 V and

−2.1 V) at 1310 nm operating wavelength [24]. The simulated result is slightly larger with a predicted chirp parameter of $\alpha_H = 1$ for these operating conditions. For application purposes, a zero or negative chirp parameter is desired to compensate a positive link dispersion.

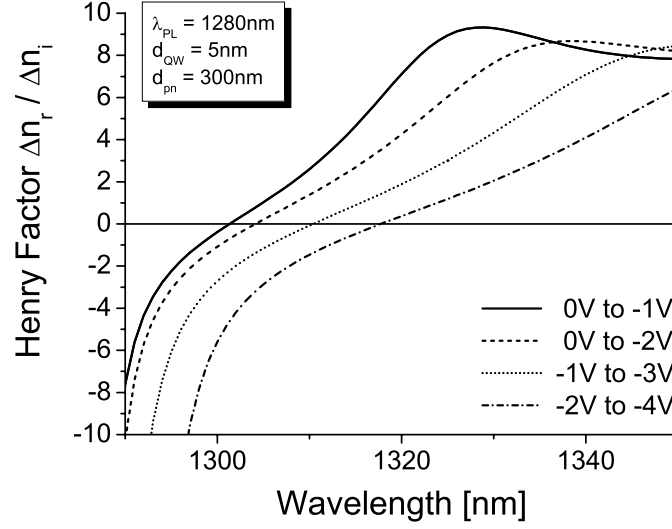


Fig. 3.10: Simulated Henry factors for the absorption changes presented in Fig. 3.8(b) according to equations (3.17) and (3.18).

Chapter 4

Gain Spectra

In the integration concept for electroabsorption modulated lasers presented in this thesis, laser and modulator sections share a common active material. While its reverse absorption characteristic is of interest for the modulator section, its gain behavior under forward current injection is crucial for the laser part. It determines both the laser threshold and the detuning range between distributed feedback (DFB) and photoluminescence (PL) wavelengths. Although large detuning is desired for optimal modulator performance, laser threshold current and modulator residual absorption have to be counterbalanced. To determine the optimal operating wavelength, gain calculations and measurements have to be applied apart from the absorption considerations of the previous chapter. In principle, gain is simply negative absorption and described by the same formalism that is presented in Chapter 3 with an additional occupation term ($f_c - f_v$). Thus, absorption may change its sign under carrier inversion, i.e., when the occupation probability of the high energy state f_c exceeds that of the low energy state f_v .

When carriers are injected into the active area, they pile up until the injection rate equals the loss rate governed by recombination terms. As the recombination rate increases superlinearly with carrier density, a higher carrier level must be supported by a higher injection current. Therefore, strong pumping results in high carrier densities yielding wide gain spectra. Below the laser threshold, photons are generated by spontaneous emission processes. They are amplified by the active material until they exit the laser cavity. As soon as the amplification equals the cavity loss rate, an undamped feedback process is started. The corresponding injection current is the laser threshold current.

The chapter is organized as follows. In Section 4.1, the material gain of a quantum well under carrier injection is examined. Most parameters can be extracted from the absorption results of the last chapter according to the equivalence of gain and absorption. However, there are some important differences caused by many-body effects. They include band filling effects with free electrons and holes, the disappearance of the exciton peak and the shrinkage of the material bandgap under carrier injection. Without including the above effects, gain spectra will not be predicted with sufficient accuracy.

In contrast to absorption, material properties of the QW itself are not sufficient to describe the waveguide's modal gain. While all quantum wells contribute equally to modal absorption under reverse bias, the carriers do not *a priori* distribute homogeneously among the wells for forward current injection. Thus, the occupation probability varies and hence the material gain of the individual QWs. Section 4.2 provides insight into the nature of physical transport processes of electrons and holes, while the underlying mathematical formalism is presented in Appendix D. The calculations prove that a homogeneous carrier distribution is a good approximation for 1310 nm AlGaInAs quantum wells, rendering simple but effective gain calculations feasible. The resulting model tailored to the special properties of the AlGaInAs material system is presented in Section 4.3. With its fast execution time, the model is a valuable means for designing shared active area EMLs.

Finally, simulated threshold currents and gain spectra are compared to broad area laser test devices and Hakki-Paoli gain experiments on ridge waveguide lasers in Section 4.4 and 4.5.

4.1 Quantum Well Gain

Gain is equivalent to negative absorption under carrier injection. In principle, it is described by equation (3.3) derived for the absorption process. However, there are three fundamental effects that have to be taken into account due to the presence of numerous charged particles:

- Band filling. A term representing the occupation probability of the valence and conduction band has to be added. For fast intraband relaxation processes, electrons and holes follow an individual Fermi-Dirac distribution $f_c(\lambda)$ and $f_v(\lambda)$ described by two separate quasi-Fermi levels E_{fc} and E_{fv} . The occupation probability is written as $[f_v(\lambda) - f_c(\lambda)]$. It equals 1 for a low excitation condition.
- The exciton vanishes ($\alpha_{EX} = 0$). The high carrier density shortens the mean carrier scattering time and thus the exciton lifetime. The exciton broadening tends to infinity as pointed out by equation (2.2). This is equivalent to the disappearance of the spectral lines in a hot vapor lamp.
- Bandgap shrinkage or bandgap renormalization ($E_g \rightarrow \tilde{E}_g$, $E_{ehh}^{cont} \rightarrow \tilde{E}_{ehh}^{cont}$, $\lambda_{ehh}^{cont} \rightarrow \tilde{\lambda}_{ehh}^{cont}$). Band structure simulations make use of the Kröning-Penny model that assumes a single electron in a lattice periodic potential. This model does not account for many-body effects like electron-electron interaction and is thus unable to explain features like excitonic states lying in the bandgap. An additional many-body effect comes into play at high electron N and hole P densities. They screen the lattice potential, effectively weakening it and reducing the bandgap energy. This is similar to a material with an increased lattice constant and thus weaker binding energy. The effect is described by

an empiric bandgap shrinkage or renormalization formula [10].

$$\tilde{E}_g = E_g - 32 \text{ meV} \left(\frac{N + P}{2 \cdot 10^{18} / \text{cm}^3} \right)^{\frac{1}{3}} \quad (4.1)$$

\tilde{E}_g	renormalized bandgap, in [eV]
E_g	equilibrium bandgap, in [eV]
N, P	electron and hole densities, in [cm^{-3}]

Note that the bandgap shrinkage is not transferred to the transition energies directly. Instead, new ground state energy levels have to be calculated for the deeper well. Thus, the decrease in transition energy is always smaller than the bandgap renormalization itself.

The transition from the PL wavelength $E_{\text{PL}}, \lambda_{\text{PL}}$ in a low excitation condition to the emission wavelength $E_{\text{BA}}, \lambda_{\text{BA}}$ in a high excitation condition of a broad area laser is illustrated in Fig. 4.1.

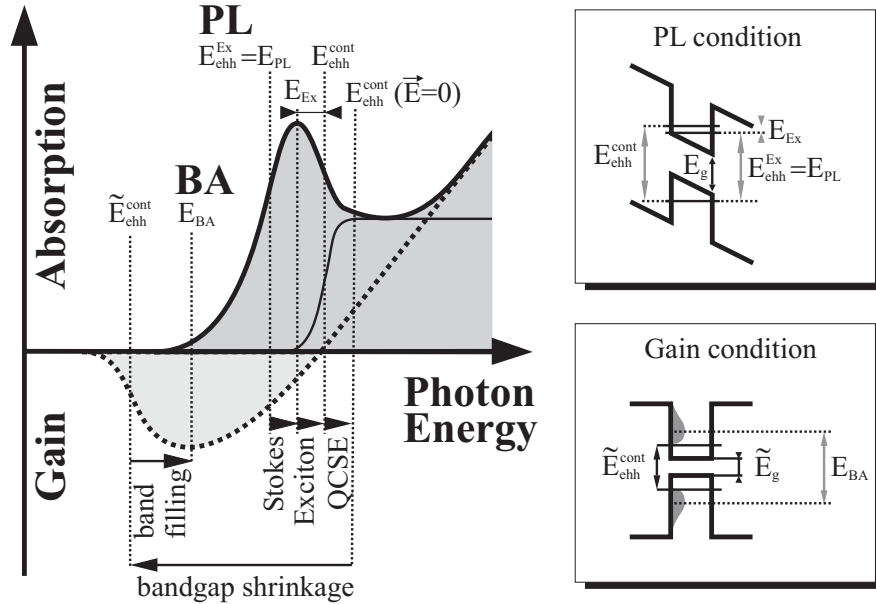


Fig. 4.1: Schematic transition from low excitation absorption to high excitation gain spectra. The PL wavelength is equivalent to the exciton peak, the broad area (BA) laser emission wavelength to the gain maximum.

The transition energy in a low excitation condition includes a Stokes' shift, the QCSE of the internal field of the pin-junction and the exciton binding energy. The Stokes' shift accounts for the fact that a small carrier density relaxes to local bandgap minima before recombining.

If carriers are injected, all three contributions will vanish until the flat band case is established. At the same time, high carrier densities are responsible for bandgap shrinkage and band filling. Unfortunately, there is no simple model that can explain the transition between low excitation and strong pumping conditions. It is still unclear at which carrier density the exciton peak of the absorption spectrum starts to disappear and at which carrier density it has completely vanished.

The gain expression chosen for the investigated samples is written as:

$$g(\lambda) = \alpha_0 \left[\frac{\alpha_{\text{HH}}}{1 + \exp\left(\frac{\lambda - \tilde{\lambda}_{\text{ehh}}^{\text{cont}}}{\Delta\lambda_{\text{ehh}}^{\text{cont}}}\right)} + \frac{\alpha_{\text{LH}}}{1 + \exp\left(\frac{\lambda - \tilde{\lambda}_{\text{elh}}^{\text{cont}}}{\Delta\lambda_{\text{elh}}^{\text{cont}}}\right)} \right] \cdot [f_{\text{c}}(\lambda) - f_{\text{v}}(\lambda)] \quad (4.2)$$

$$f_{\text{c}}(\lambda) = \frac{1}{1 + \exp\left(\frac{E_1(\lambda) - E_{\text{fc}}}{k_{\text{B}}T}\right)} \quad (4.3)$$

$$f_{\text{v}}(\lambda) = \frac{1}{1 + \exp\left(\frac{E_2(\lambda) - E_{\text{fv}}}{k_{\text{B}}T}\right)} \quad (4.4)$$

$$E_1(\lambda) = \frac{1240 \text{ eV nm}}{E_{\text{c}} + E_{\text{e1}} + \frac{m_{\text{ehh}}^{\text{r}}}{m_{\text{e}}} \left(\frac{2\pi\hbar c_0}{\lambda} - \tilde{E}_{\text{ehh}}^{\text{cont}} \right)} \quad (4.5)$$

$$E_2(\lambda) = \frac{1240 \text{ eV nm}}{E_{\text{v}} - E_{\text{hh1}} - \frac{m_{\text{ehh}}^{\text{r}}}{m_{\text{hh}}^{\text{t}}} \left(\frac{2\pi\hbar c_0}{\lambda} - \tilde{E}_{\text{ehh}}^{\text{cont}} \right)} \quad (4.6)$$

α_0	gain amplitude, $= 7.8 \cdot 10^5 \text{ m}^{-1} \cdot d_{\text{QW}}/5 \text{ nm}$
$\alpha_{\text{HH}}, \alpha_{\text{LH}}$	relative gain amplitudes, $= 1, = 1.76$
$\tilde{\lambda}_{\text{ehh}}^{\text{cont}}, \tilde{\lambda}_{\text{elh}}^{\text{Ex}}$	renormalized transition wavelengths in [nm]
$\tilde{E}_{\text{ehh}}^{\text{cont}}, \tilde{E}_{\text{elh}}^{\text{Ex}}$	renormalized transition energies in [eV]
$\Delta\lambda_{\text{ehh}}^{\text{cont}}, \Delta\lambda_{\text{elh}}^{\text{cont}}$	gain linewidth broadening, $= 7.4 \text{ nm}$ at 1310 nm , $= 10.5 \text{ nm}$ at 1550 nm
$f_{\text{c,v}}(\lambda)$	Fermi occupation probability, given in [12]
$E_{\text{fc}}, E_{\text{fv}}$	quasi-Fermi levels in [eV]
m_{e}	electron mass, typically $0.0469 m_0$ in this thesis
m_{hh}^{t}	averaged transversal heavy hole mass, typically $0.0840 m_0$ in this thesis
$m_{\text{ehh}}^{\text{r}}$	reduced effective mass, typically $0.0300 m_0$ in this thesis
T	temperature

Under carrier injection conditions, the bias voltage across the active area compensates the built-in diffusion potential and the internal field vanishes. For a 5 nm thick QW, zero field

linewidth broadening is 7.4 nm according to equation (3.8). This broadening figure was chosen as spectral gain broadening for all QWs within this thesis. Under flat band conditions, state overlaps are close to unity and therefore set to 1.

4.2 Injection and Carrier Transport

For reverse bias operation, the material absorption is similar for all QWs of a kind. An equal contribution of each QW to the modal absorption weighted by its confinement factor is a reasonable approximation. For forward current injection, the carrier distribution among the wells may be inhomogeneous, resulting in different quasi-Fermi level separations and material gains for each well. The distribution of electrons and holes among the QWs is calculated by the semi-classical drift/diffusion/Poisson approach presented in Appendix D. The standard layer structure for this injection calculation is shown in Table 4.1. Other samples differ in number, thickness and photoluminescence wavelength of the active layers 2 to 24 while the surrounding layer structure remains the same. The contact layers are omitted for the injection simulation. A detailed explanation of the layer structure is provided in Section 6.2 on the epitaxial design.

#	Function	Material	Thickness [nm]	Bulk λ_{PL} [μm]	Strain ε_{xx} [%]	x	y	Doping N_D $10^{18}/\text{cm}^3$
	Contact		boundary					
30	Cladding	InP	1600					-0.5 (p)
29	Etchstop	$\text{Ga}_x\text{InAs}_y\text{P}$	45	1.05	0	0.137	0.301	-0.5 (p)
28	Grating 1	InP	45					-0.5 (p)
27	Grating 2	$\text{Ga}_x\text{InAs}_y\text{P}$	130	1.05	0	0.137	0.301	-0.5 (p)
26	Spacer	InP	10					-0.5 (p)
25	El.stop	Al_xInAs	18	0.87	0	0.47		-0.5 (p)
24	SCH	$\text{Al}_x\text{Ga}_y\text{InAs}$	80	1.05	0	0.315	0.157	
	11 \times Bar	$\text{Al}_x\text{Ga}_y\text{InAs}$	8	1.10	+0.5(t)	0.265	0.278	
	10 \times QW	$\text{Al}_x\text{Ga}_y\text{InAs}$	5	1.29 ¹	-0.95(c)	0.170	0.159	
2	SCH	$\text{Al}_x\text{Ga}_y\text{InAs}$	80	1.05	0	0.315	0.157	
1	Spacer	InP	1000					+1.0 (n)
	Contact		Boundary					

Tab. 4.1: Structure for gain calculations. It represents broad area lasers corresponding to epitaxial structure I in Section 6.2.3. ¹ QW PL includes confinement energy, pin QCSE and exciton energy.

Simulation results are plotted in Fig. 4.2 for a 400 μm long and 50 μm wide uncoated BA laser at threshold. The proposed threshold gain is 47/cm at room temperature under pulsed operation. All graphs are plotted versus the z -position along the growth axis.

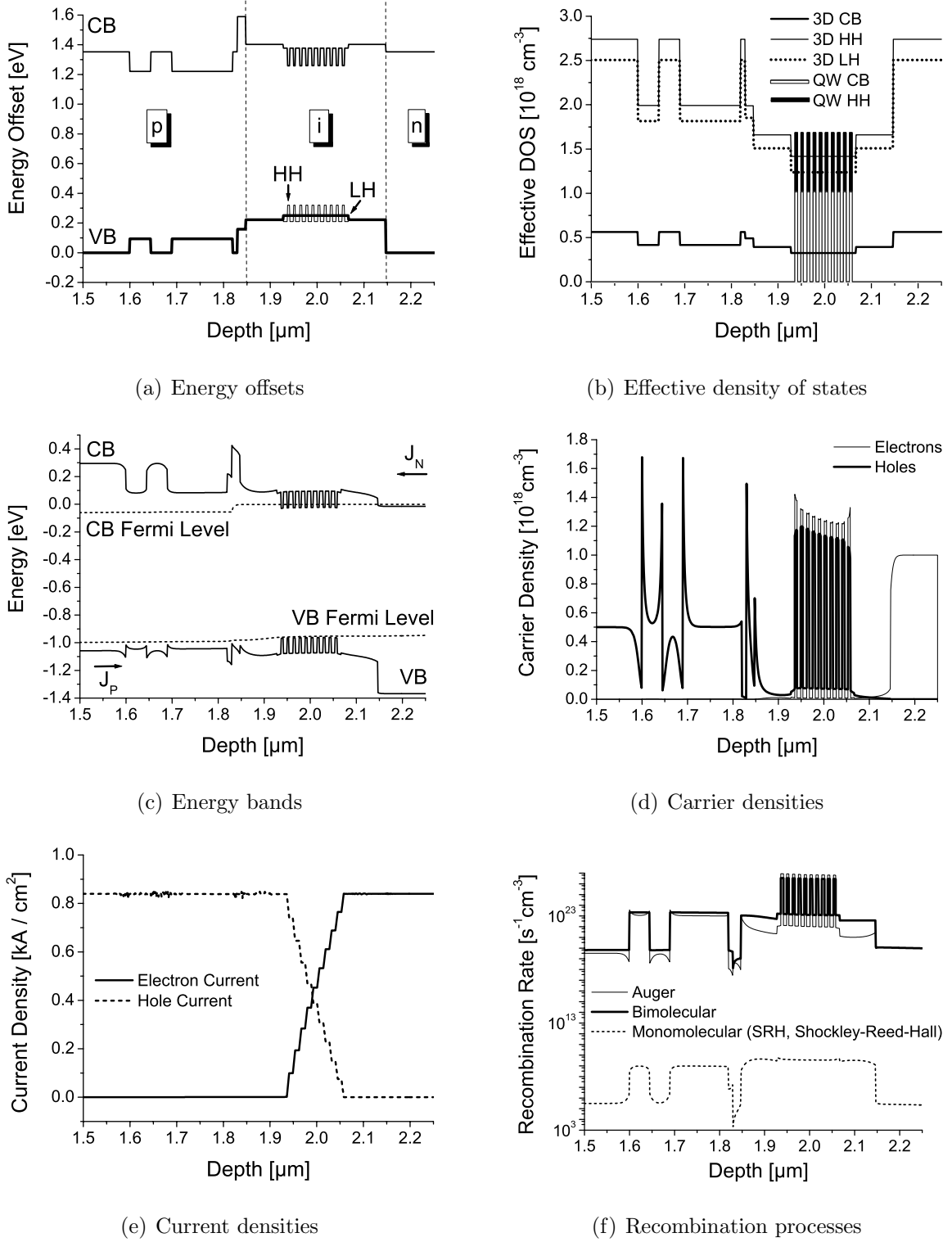


Fig. 4.2: Drift/diffusion simulation inputs (a,b) and results (c-f) at laser threshold. The corresponding layer structure is given in Table 4.1.

Figures 4.2(a) and 4.2(b) show various input parameters of the simulation. They are interpolated from binary semiconductor literature values according to Appendix A. Figure 4.2(a) includes the band energy offsets of the different layers compared to the InP cladding material of conduction band and both hole subbands, respectively. In the QW layers, the ground state energy is plotted rather than the band edge energy. Due to strain in barriers and QWs, heavy and light hole subbands split up and have to be treated individually. Fig. 4.2(b) shows the effective density of states (DOS) for the various bands. Two-dimensional states are represented as pillars. Hole bands feature an increased density of states due to their heavier carrier mass.

The next four graphs contain selected simulation results at laser threshold current. Figure 4.2(c) and 4.2(d) show the band diagram and the corresponding carrier density. For the AlGaInAs band offsets, an almost uniform carrier distribution arises [25]. The high hole density in the barrier level P^{3D} is due to the shallow valence band offset. This hole density is high enough to support a hole current $J_P = \mu_P P^{3D} \nabla E_{fv}$ equal to the electron current J_N with negligible Fermi level slope, although the carrier mobility is much smaller for the holes μ_P than for the electrons μ_N . The result is a uniform carrier distribution in the active area. However, the development of a homogeneous carrier distribution ($\mu_P P^{3D} \approx \mu_N N^{3D}$) strongly depends on the barrier height and recombination parameters.

The electron stop layer reduces the electron overshoot into the p-cladding layer as indicated by a step in the conduction band quasi-Fermi level. Over- and undershoots of the carrier densities occur at heterojunction interfaces.

Finally, Fig. 4.2(e) and 4.2(f) show the current densities and their derivative expressed by the recombination processes. Steps in the current density correspond to the recombination peaks in the QWs. Auger recombination is the dominant non-radiative current path in the active area, whereas monomolecular Shockley-Reed-Hall (SRH) recombination is only important close to the contacts. At threshold current and room temperature, there is no significant current overshoot, i.e. electron current in the p- and hole current in the n-region, respectively. The broad area laser characteristics in Fig. 4.3 indicate a laser threshold current of 840 A/cm², a turn-on voltage of 0.92 V and an emission wavelength of 1315 nm at the resulting total gain maximum. Although the carrier distribution is very homogeneous, small fluctuations are sufficient to reduce the QW gain on the n-side of the active area.

4.3 Simplified Injection Model for AlGaInAs QWs

The sophisticated drift/diffusion approach of the last section revealed an almost uniform carrier distribution among the QWs of an AlGaInAs active material. This is equivalent to flat band edges and Fermi levels at laser threshold. Therefore, a simplified algorithm with flat band edges and Fermi levels $d\varphi/dx = 0$, $dE_{fc,fv}/dx = 0$ *a priori* will agree with the complex drift/diffusion approach. The simplified boundary conditions are outlined in Fig. 4.4. With flat conduction $E_c(z)$ and valence band $E_{hh}(z)$, flat Fermi levels and a Fermi level separation according to the applied voltage V_{LD} , i.e., $E_{fc} = E_{fv} + e V_{LD}$, the problem is simplified to

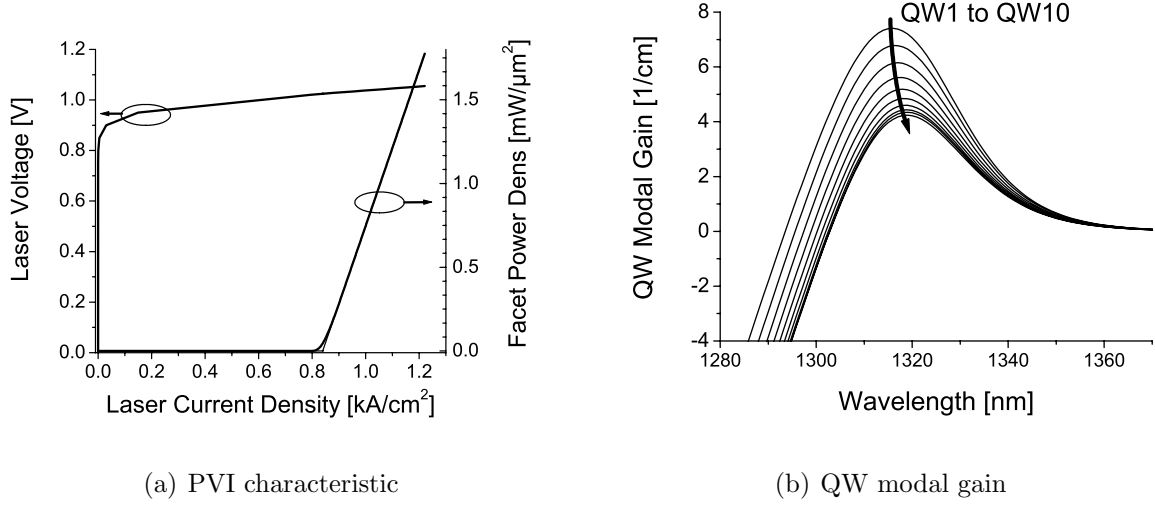


Fig. 4.3: Simulated electrical and optical broad area laser characteristic and individual QW gain.

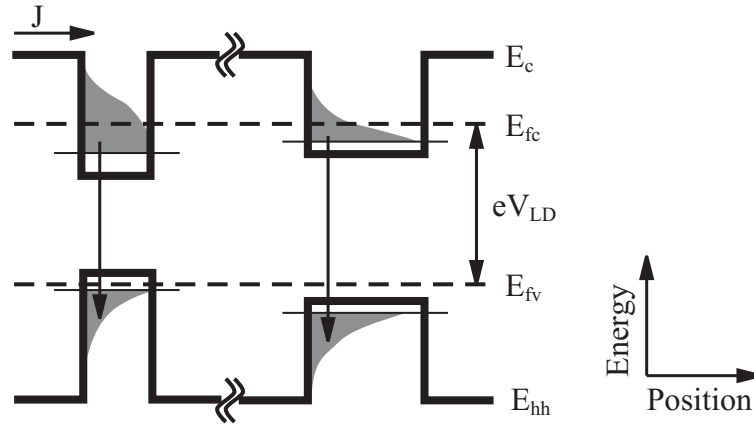


Fig. 4.4: Simplified band lineup of AlGaInAs active area under forward pumping.

one scalar unknown, the absolute Fermi level position E_{fv} . It is determined by the following procedure (neglecting the voltage drop at the series resistance):

1. Initial condition: The valence band (VB) Fermi level lies at the VB QW band edge, the conduction band (CB) Fermi level is separated according to the external voltage: $E_{fv} = E_{hh,QW}$, $E_{fc} = E_{fv} + eV_{LD}$.
2. Electron and hole carrier densities N and P for each well and barrier layer are calculated by:

$$N = \underbrace{N_c^{3D} e^{\frac{E_{fc}-E_c}{k_B T}}}_{N^{3D}} + \underbrace{N_c^{2D} \sum_i \ln \left(e^{\frac{E_{fc}-E_c-\tilde{E}_{ei}}{k_B T}} + 1 \right)}_{\text{Additional term in QW layers}} \quad (4.7)$$

$$P = \underbrace{N_{\text{lh}}^{3\text{D}} e^{\frac{E_{\text{lh}} - E_{\text{fv}}}{k_{\text{B}} T}} + N_{\text{hh}}^{3\text{D}} e^{\frac{E_{\text{hh}} - E_{\text{fv}}}{k_{\text{B}} T}}}_{P^{3\text{D}}} + \underbrace{N_{\text{hh}}^{2\text{D}} \sum_i \ln \left(e^{\frac{E_{\text{hh}} - \tilde{E}_{\text{hhi}} - E_{\text{fv}}}{k_{\text{B}} T}} + 1 \right)}_{\text{Additional term in QW layers}} \quad (4.8)$$

Variable	Description	Ref	Typical Value	
			bulk InP	Al _{0.17} Ga _{0.16} In _{0.67} As QW
$N_{\text{c}}^{3\text{D}}(z)$	CB effective DOS	[26]	$5.63 \cdot 10^{17} \text{ cm}^{-3}$	$3.25 \cdot 10^{17} \text{ cm}^{-3}$
$N_{\text{lh}}^{3\text{D}}(z)$	LH band effective DOS	[26]	$2.51 \cdot 10^{18} \text{ cm}^{-3}$	$1.24 \cdot 10^{18} \text{ cm}^{-3}$
$N_{\text{hh}}^{3\text{D}}(z)$	HH band effective DOS	[26]	$2.74 \cdot 10^{18} \text{ cm}^{-3}$	$1.42 \cdot 10^{18} \text{ cm}^{-3}$
$N_{\text{c}}^{2\text{D}}(z)$	CB-QW effective DOS	[26]	-	$1.02 \cdot 10^{18} \text{ cm}^{-3}$
$N_{\text{hh}}^{2\text{D}}(z)$	HH-QW effective DOS	[26]	-	$1.69 \cdot 10^{18} \text{ cm}^{-3}$
$\tilde{E}_{\text{e1}}(z)$	Electron confinement energy	A.3	-	0.0786 eV
$\tilde{E}_{\text{hh1}}(z)$	1st HH confinement energy	A.3	-	0.0207 eV
$\tilde{E}_{\text{hh2}}(z)$	2nd HH confinement energy	A.3	-	0.0775 eV

The three-dimensional terms $N^{3\text{D}}$ and $P^{3\text{D}}$ are present in both barrier and QW layers, the two-dimensional terms in the QW layers only.

3. Bandgap shrinkage and the resulting ground state renormalization $\tilde{E}_{\text{ei}}(N, P)$, $\tilde{E}_{\text{hhi}}(N, P)$ is computed for each well.
4. Charge neutrality is obtained by iterating E_{fv} with $E_{\text{fc}} = E_{\text{fv}} + eV_{\text{LD}}$ and recalculating the carrier densities until the condition $\int N dz = \int P dz$ is met.
5. Steps 2, 3 and 4 are repeated until \tilde{E}_{ei} , \tilde{E}_{hhi} , E_{fv} and N and P converge.

Since the energy levels stay constant, all integrals can be evaluated as a summation of contributions of the individual layers. After convergence, the simulation results are extracted:

- the individual QW material gain spectra g_{QWi} according to equation (4.2)
- the modal gain \tilde{g} :

$$\tilde{g} = \max_{\lambda} \left[\sum_i \Gamma_{\text{QWi}} g_{\text{QWi}}(\lambda) \right] \quad \text{for BA laser} \quad (4.9)$$

$$\tilde{g} = \sum_i \Gamma_{\text{QWi}} g_{\text{QWi}}(\lambda_{\text{DFB}}) \quad \text{for DFB laser} \quad (4.10)$$

- the injection current density

$$J = e \int \hat{A} \frac{NP - N_{\text{i}}^2}{N + P + 2N_{\text{i}}} + \hat{B} (NP - N_{\text{i}}^2) + \hat{C} (N + P) (NP - N_{\text{i}}^2) dz \quad (4.11)$$

\hat{A}	SRH recombination parameter, $= 5 \cdot 10^{-7}/\text{s}$ in this thesis
\hat{B}	bimolecular recombination parameter, $= 2.13 \cdot 10^{-10} \text{ cm}^3/\text{s}$ in this thesis
\hat{C}	Auger recombination parameter, $= 2.13 \cdot 10^{-28} \text{ cm}^6/\text{s}$ in this thesis
N_i	intrinsic carrier density, $= 8.65 \cdot 10^6 \text{ cm}^{-3}$ for InP

In an external loop, the bias voltage is varied to identify the threshold current. Due to its negligible execution time, the simplified algorithm is a valuable tool for optimization purposes, especially when QW types differing in PL wavelength, width or strain are included in a laser diode.

Side note: A homogeneous carrier distribution is not a suitable model for all active materials. Figure 4.5 shows carrier distributions of other common material systems for 1310 nm emission wavelength with different valence band offsets. Here, the balance between electron

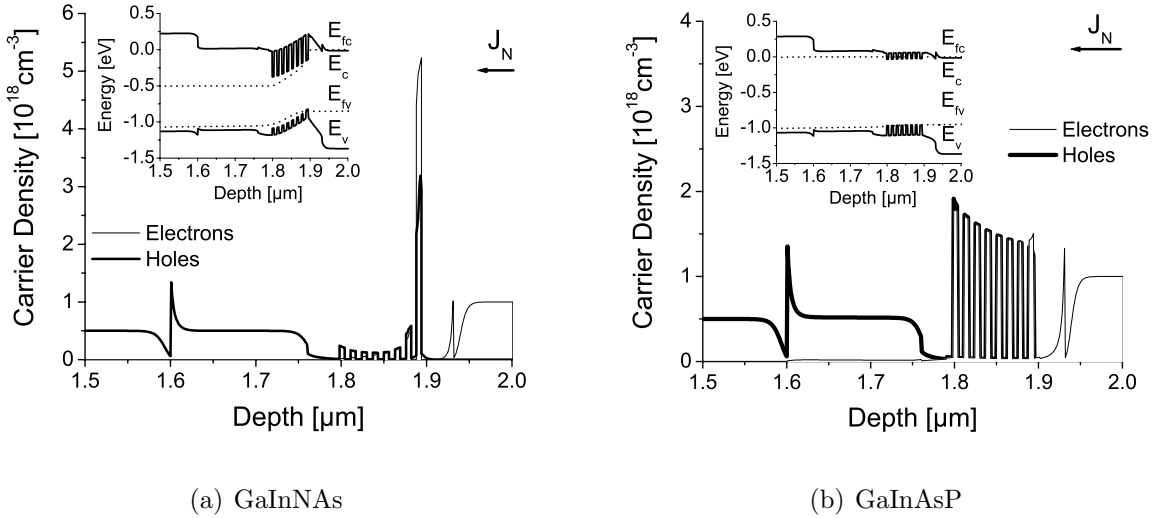


Fig. 4.5: Simulated carrier distributions and band diagrams (inset) of other common 1310 nm emission material systems at laser threshold.

and hole band offsets and effective masses is destabilized to either side. In the GaInNAs system, electron mobility suffers from an extraordinarily high effective mass along with very strong conduction band confinement. Injected from the n-cladding, most of the electrons become stuck in the first QW. The more mobile holes are torn across the active area by electrostatic force. The QW filling is very inhomogeneous. In experiments, GaInNAs broad area lasers show the best performance for a single QW [27]. Note the voltage drop in front of the first QW, which manifests itself in a higher turn-on voltage measured in GaInNAs compared to InP based devices [28]. Although not as significant, GaInAsP suffers from inhomogeneous pumping as well. Here, hole trapping is dominant due to the large valence band offset.

4.4 Comparison to Broad Area Laser Experiments

Broad area (BA) lasers are an excellent tool for extracting the carrier recombination parameters \hat{A} , \hat{B} and \hat{C} . Unlike ridge waveguide lasers, their carrier distribution and current injection are independent of the in-plane position and vary only in growth direction. Their emission wavelength corresponds to the gain maximum wavelength. Finally, their fabrication process is very simple and thermal effects are negligible under pulsed operation.

For the simulation, the threshold gain of an uncoated Fabry-Perot laser is calculated by equation (4.12) [10]:

$$\tilde{g}_{\text{th}} = \tilde{\alpha}_i + \tilde{\alpha}_m = \tilde{\alpha}_i - \frac{2}{l_{\text{LD}}} \ln \left(\frac{n_{\text{eff}} - 1}{n_{\text{eff}} + 1} \right) \quad (4.12)$$

\tilde{g}_{th}	laser threshold gain, = 47/cm for the investigated BA lasers
$\tilde{\alpha}_m$	waveguide mirror losses, = 32/cm for the investigated BA lasers
$\tilde{\alpha}_i$	intrinsic waveguide scattering losses, = 15/cm in this thesis
l_{LD}	laser length, = 400 μm for the investigated BA lasers
n_{eff}	effective waveguide index, ≈ 3.285 in this thesis

Figure 4.6 shows a set of gain spectra above threshold corresponding to the epitaxial structures of Table 4.2. Note that only the active layers vary between the different structures. The surrounding layers are common for all devices and equal to the layer structure in Table 4.1. The gain spectra are generated by the simplified algorithm of the previous section. The fit result for the recombination parameters \hat{A} , \hat{B} and \hat{C} is given in Table 4.3. Although the underlying structures cover a wide range of QW numbers and thicknesses, Table 4.2 shows that the simulated results for BA laser threshold currents and emission wavelengths are in good agreement with the experimental data.

Device	QWs	λ_{PL} [nm]	Threshold J_{th} [kA/cm ²]		Wavelength λ_{BA} [nm]	
			sim	meas	sim	meas
I	10 \times 5 nm	1290	0.83	0.87	1317	1312
II	3 \times 5 nm,	1292	0.95	0.95	1301	1304
	8 \times 7.5 nm	1277				
IV	8 \times 5 nm	1290	0.85	0.83	1313	1307
V	8 \times 7.5 nm	1272	0.65	0.68	1292	1293

Tab. 4.2: Broad area laser simulation and experimental results.

Figure 4.6 indicates that each of the eight QWs of structure IV requires stronger pumping than each of the ten QWs of structure I to make the laser reach its threshold gain. This stronger band filling manifests itself in a blue shift of the gain maximum. The two QW type device II features a wider gain spectrum than the single type ones.

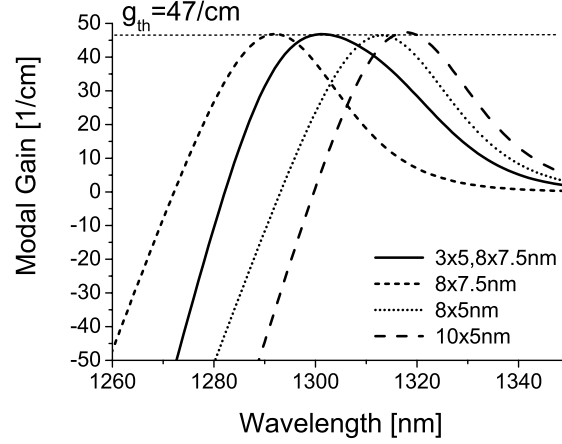


Fig. 4.6: Simulated gain spectra at laser threshold for BA lasers featuring various epitaxial structures.

\hat{A}	$5 \cdot 10^{-7} / \text{s}$
\hat{B}	$2.13 \cdot 10^{-10} \text{ cm}^3 / \text{s}$
\hat{C}	$2.13 \cdot 10^{-28} \text{ cm}^6 / \text{s}$

Tab. 4.3: Fit of the recombination terms \hat{A} , \hat{B} and \hat{C} .

4.5 Ridge Waveguide Gain Spectra

After finding a set of recombination parameters, the simulation was verified by comparing to gain spectra measurements below threshold. The experiment was carried out using the Hakki-Paoli method [29] on lateral single-mode ridge waveguide Fabry-Perot lasers. The devices were $500 \mu\text{m}$ long, yielding a threshold gain of $40/\text{cm}$ according to equation (4.12). Above threshold, the gain spectra are pinned. The device under test was made of the two QW type structure II. The results are presented in Fig. 4.7. Note that the injection currents differ in experiment and simulation for low excitation conditions due to non-radiative recombination in the cladding layers. An empiric ridge factor of 2.3 accounts for the current spreading below the ridge. This current spreading results in inhomogeneous pumping of the active area for ridge waveguide lasers. Although the gain curves are a superposition of the individual contributions of two different QW types, the simulation is in good agreement with the experimental data. Without a simulation tool, it becomes difficult to analyze and finally optimize these complicated gain materials. Too many parameters like QW numbers, thicknesses and PL wavelengths render a purely experimental optimization practically impossible. The model presented here will be used in the following chapters to identify design rules for EMLs with a common active area.

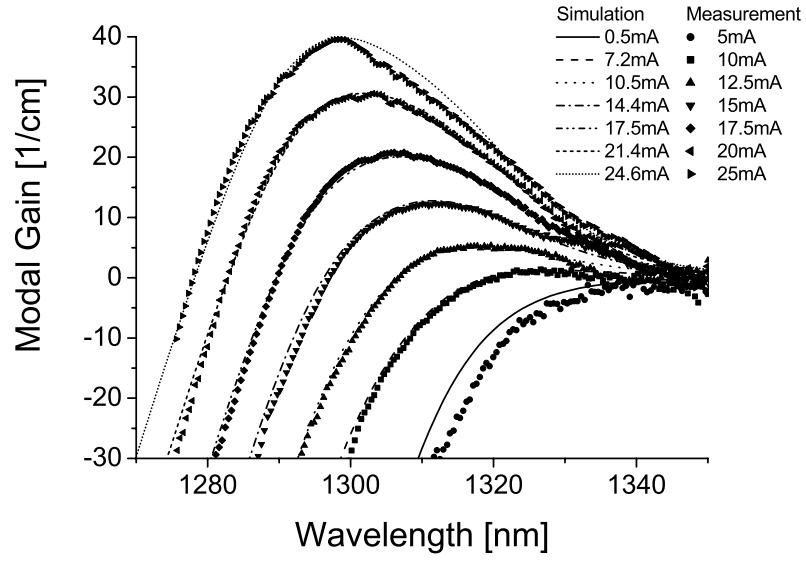


Fig. 4.7: Hakki-Paoli experiment and simulated gain spectra of structure II. Here, the QW PL wavelengths are 1285 nm and 1270 nm, respectively.

Chapter 5

Laser Modulator Ridge Waveguides

Most optical connections and light sources make use of optical waveguides. In contrast to free space transmission, the transverse mode profile stays constant within any ideal waveguide over arbitrary length. Thus, there is no quadratic power density decrease with the link distance as in the case for free space propagation. Furthermore, optical waveguides play a role in the design of resonant cavities for laser applications.

No matter whether optical wave or microwave, a perfect waveguide is characterized by its transversal mode profiles and their appropriate propagation constant or effective index. Both are found by solving Maxwell's equations for a two-dimensional eigenvalue problem in the waveguide's transversal plane. For most applications, single-mode waveguides are desired as the presence of multiple modes, each with its own distinct propagation velocity, will cause pulse broadening or even distortion. This puts a physical limit on the lateral extension of any waveguide.

In contrast to microwave solutions like microstrip or coaxial lines, which are usually fabricated with perfect electric boundaries, optical waveguides are usually made of dielectric materials. The waveguiding is provided by a highly refractive material surrounded by a lower index cladding. It can be explained by total inner reflection of light rays in a simple model.

In a laser, the optical resonator determines the amount of gain that the active material has to deliver to overcome the loss of optical power, the so-called threshold gain. The total loss is a sum of mirrors losses, internal absorption and scattering. Additionally, the spectral properties of the output light are defined by the resonant cavity. Because of their broadband cleaved mirrors and long cavities, Fabry-Perot lasers feature emission spectra as wide as the active material gain with very small sidemode suppression ratios. Wavelength selective cavities allow for only one dominant longitudinal mode, resulting in sharp distributed feedback (DFB) laser spectra. In these lasers, the predominant wavelength is selected by gratings along the waveguide with a period Λ equal to half the waveguide wavelength. At this so-called Bragg wavelength, the reflectivity of the grating is maximal as reflections from adjacent surfaces interfere constructively. Multi-layer reflection coatings are well-known from

other optical applications like Vertical Cavity Surface Emitting Lasers (VCSELs). Periodical gratings can be considered as a layer structure composed of *effective* indices.

In this work, DFB lasers are manufactured by an overgrown etch pattern on top of the active area or metal stripes along the ridge waveguide. Both concepts are shown in Fig. 5.1.

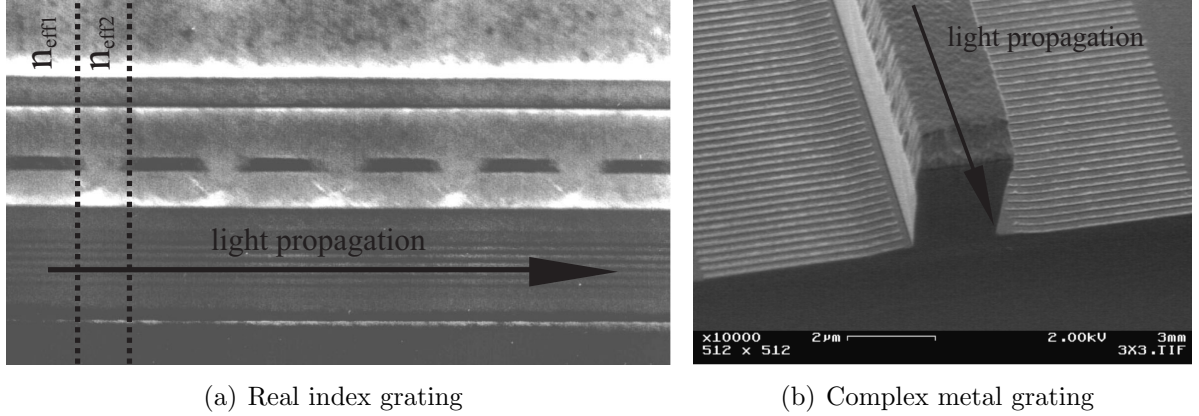


Fig. 5.1: Scanning electron microscope (SEM) pictures of grating variants. (a) DFB laser ridge waveguide cleaved along the propagation axis, showing the active area and the grating layer on top. The grating layer can be identified by the alternating black (high index quaternary material, etched selectively) and gray (low index InP) pattern. (b) Top view of a metal grating laser showing the ridge and exit facet. The metal grating stripes can be on either side of the ridge.

The reflection coefficient r^{Field} between two media 1 and 2 is given by Snellius' law of reflection [13]. Using complex material refractive indices $n = n_r + i\alpha\lambda/4\pi$, an interface with a change in absorption or gain $\Delta\alpha$ causes amplitude reflection just like a dielectric interface Δn_r , but with a phase shift of ninety degrees:

$$r^{\text{Field}} = \frac{n_1 - n_2}{n_1 + n_2} = \frac{\Delta n}{2\bar{n}} = \frac{\Delta n_r + i\frac{\lambda}{4\pi}\Delta\alpha}{2\bar{n}} \quad (5.1)$$

where $\bar{n} = (n_1 + n_2)/2$ is the mean refractive index. This phase shift is the main difference of metal gratings with respect to their index counterparts. While the round trip phase exactly at the Bragg wavelength of a continuous index grating is destructive (-180°), the phase shifts in a metal grating add up to a constructive interference ($-180^\circ + 2 \cdot 90^\circ$). Therefore, index lasers intrinsically exhibit two modes to either side of a stop band centered around the Bragg wavelength, while their metal counterparts feature only one central mode exactly at the Bragg wavelength. Since applications usually demand single-mode laser sources, there is a clear advantage offered by the metal grating technology.

This chapter begins with an overview of waveguide fundamentals in Section 5.1, explaining the models used to design ridge waveguide DFB lasers and modulators. It is followed by a

theoretical treatment of single-mode production yield in Section 5.2, comparing index and metal grating DFB lasers. Finally, a brief discussion on optical feedback and scattering in ridge waveguides is presented in Sections 5.3 and 5.4.

Side note: While some text books make use of absorption or gain coefficients for the electric field ($\alpha^{\text{Field}}, g^{\text{Field}}$), all absorption and gain coefficients in this thesis refer to optical powers ($\alpha, g = 2\alpha^{\text{Field}}, 2g^{\text{Field}}$). Only reflection coefficients may be field (r^{Field}) or intensity ($r = |r^{\text{Field}}|^2$) based. Similarly, all wavelengths are free space wavelengths.

5.1 Fundamentals

In the ray model, light guiding is explained by total internal reflections. In the wave model, every waveguide supports a limited number of discrete modes, each traveling with its own distinct lateral field distribution and propagation constant. For linearly polarized TEM waves, the propagation of a mode in a waveguide along the x -axis is described by [10]:

$$H^+(x, y, z, t) = H(y, z) \cdot e^{i\left(\frac{2\pi n_{\text{eff}}}{\lambda} x - \omega t\right)} \quad (5.2)$$

$H^+(x, y, z, t)$	magnetic field of forward traveling mode (in x -direction)
$H(y, z)$	transversal magnetic field of waveguide mode
ω	light angular frequency, $= 1.44 \cdot 10^{15}$ Hz for 1310 nm wavelength
λ	free space wavelength, not to be confused with waveguide wavelength
n_{eff}	waveguide effective refractive index, may be complex, ≈ 3.28

The magnetic field is used for calculation rather than the electric field as the relative permeability is almost constant in semiconductors. Mode profile $H(y, z)$ and effective index n_{eff} are determined as the eigenfunction and the eigenvalue of a two-dimensional waveguide cross-section problem, see Appendix C. The effective index may be complex, resulting in amplification or damping of the wave [10]:

$$n_{\text{eff}} = n_{\text{eff},r} + i \cdot n_{\text{eff},i} = n_{\text{eff},r} + i \cdot \frac{\tilde{\alpha}\lambda}{4\pi} \quad (5.3)$$

$n_{\text{eff},r}$	real part of effective index
$n_{\text{eff},i}$	imaginary part of effective index, $\approx 10^{-3}$ for 100/cm modal absorption at 1310 nm
$\tilde{\alpha}$	waveguide modal absorption, ≈ 50 to 400/cm

The optical power density is proportional to the modulus squared of the fields:

$$P_{\text{opt}}(y, z) \propto |H(y, z)|^2 \quad (5.4)$$

$$P_{\text{opt}}(x) = P_0 \cdot e^{-\tilde{\alpha}x} \quad (5.5)$$

$P_{\text{opt}}(y, z)$	transversal optical power density distribution
$P_{\text{opt}}(x)$	guided mode optical power
P_0	input mode optical power, ≈ 10 mW

After a certain length l_{EAM} along an absorption modulator with variable absorption $\Delta\tilde{\alpha}$, the extinction ratio ER is defined as:

$$\frac{ER}{\text{dB}} = -10 \log \left[\frac{P_0 e^{-(\tilde{\alpha}_0 + \Delta\tilde{\alpha})l_{\text{EAM}}}}{P_0 e^{-\tilde{\alpha}_0 l_{\text{EAM}}}} \right] = 4.343 \Delta\tilde{\alpha} l_{\text{EAM}} \quad (5.6)$$

5.1.1 Scalar Wave Equation

Eigenmodes in semiconductor ridge waveguide structures can be calculated by the scalar wave equation [10]:

$$\Delta H(y, z) + \frac{4\pi^2}{\lambda^2} (n^2(y, z) - n_{\text{eff}}^2) H(y, z) = 0 \quad (5.7)$$

$n(y, z)$	material index distribution, may be complex, between 1 and 3.5
-----------	--

It is derived from Maxwell's equations for linear, isotropic materials assuming weak guiding, that is small optical intensities (e.g. 1% of the intensity maximum) at dielectric interfaces with a strong change in permittivity (e.g. semiconductor to air or metallic interfaces). Then, the boundary conditions for electric and magnetic fields are equal and TE (electric field in epitaxial layer plane) and TM (magnetic field in epitaxial layer plane) modes degenerate, having the same effective index and field profile. Therefore, (5.7) can be solved for either

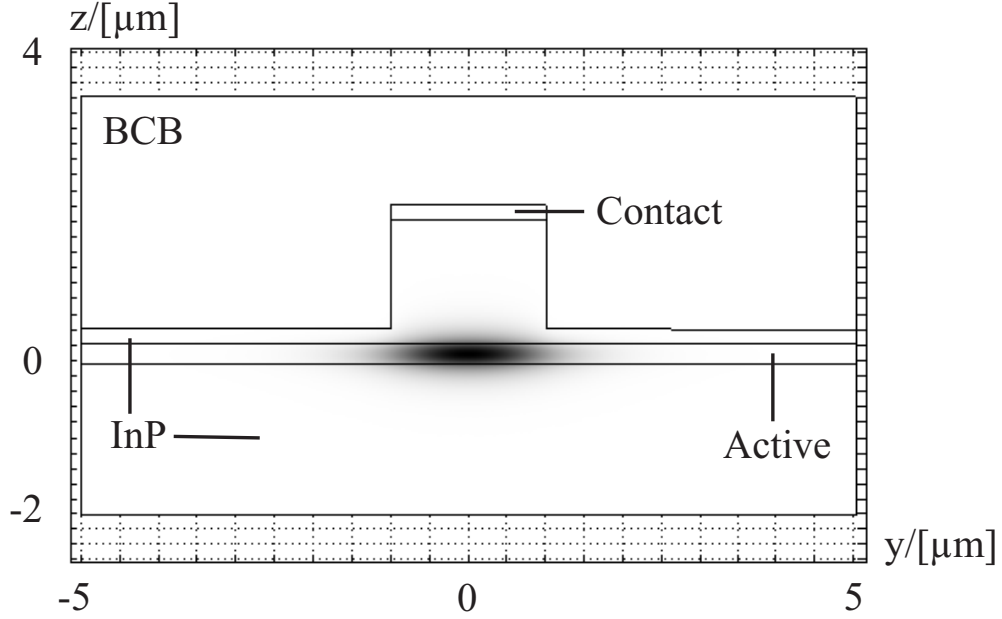


Fig. 5.2: Calculated modal intensity distribution of a ridge waveguide eigenmode, eigenvalue $n_{\text{eff}}=3.264$. The input parameters are $n_{\text{InP}} = 3.182$ (doped InP), $n_{\text{ct}} = 3.68$ (ternary contact layer), $n_{\text{BCB}} = 1.5$ (benzocyclobutene, BCB) and $n_{\text{act}} = 3.431$ (average index of quaternary active material).

the electric or the magnetic field, respectively. Boundary conditions for guided waves are vanishing fields far away from the waveguide core. Similar to the Schrödinger equation of Chapter A.3, equation (5.7) is a functional eigenvalue problem and can be transferred to a matrix eigenvalue problem by the discretization procedure presented in Appendix C. Note that in this analogy, the refractive index profile in the wave equation is similar to the electrostatic potential in the Schrödinger equation. Figure 5.2 shows a calculated two-dimensional intensity profile of the fundamental mode of a single-mode ridge waveguide.

5.1.2 Method of Effective Index

If the mode profiles of two waveguides stay almost constant at an intersection, wave guiding or waveguide reflections can be approximated by the propagation constants n_{eff} of each region. As effective indices rather than material indices are used to describe each region, this method is called the ‘effective index method’. In principle, there are two different ways of using this method. One is the calculation of a waveguide’s effective index eigenvalue (Fig. 5.3b), the other the calculation of reflections at disturbances in the propagation direction (Fig. 5.3c). Both procedures are outlined in Fig. 5.3. Figure 5.3(a) shows two one-dimensional slab waveguides with different layer thicknesses and effective indices $n_{\text{eff},1}$ and $n_{\text{eff},2}$. The corresponding mode intensity profile is indicated by the black curves. For the calculation of

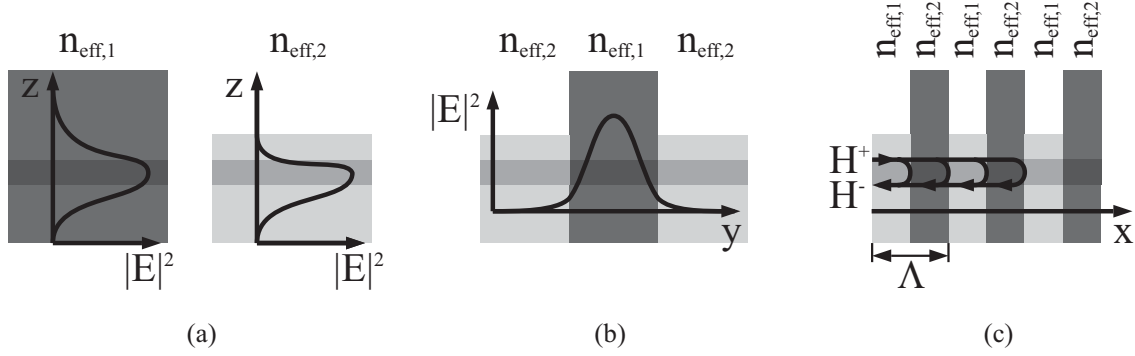


Fig. 5.3: The effective index method. (a) slab waveguide effective index calculation with infinite layers, (b) slabs combined to a ridge waveguide in the transversal plane, (c) slabs combined to a Bragg grating in the propagation direction.

the one-dimensional slab effective indices and mode profiles, all layers are assumed to have infinite widths perpendicular to the z -direction.

To find two-dimensional waveguide eigenvalues, the one-dimensional slab waveguides are assembled to a new structure along the transversal y -direction, resulting in a new slab waveguide geometry of *effective* index layers as shown in Fig. 5.3(b). In a consequent one-dimensional calculation, the resulting ridge waveguide effective index and transversal mode profile are obtained. Note that an effective index step less than 0.02 between ridge $n_{\text{eff},1}$ and side $n_{\text{eff},2}$ effective index is necessary for lateral single-mode operation for $2\ \mu\text{m}$ wide ridges at 1310 nm wavelength.

To determine reflections at waveguide intersections, a new structure composed of alternating layers in propagation x -direction is assembled, producing dielectric interfaces between *effective* index layers as shown in Fig. 5.3(c). The field reflection coefficient r^{Field} at such an interface is given by the well-known relation

$$r^{\text{Field}} = \frac{n_{\text{eff},1} - n_{\text{eff},2}}{n_{\text{eff},1} + n_{\text{eff},2}} \quad (5.8)$$

For the investigated structures, the effective index method is always a reasonable approximation, except for the deeply etched ridges due to their strong confinement. Figure 5.4 shows the field distribution along the growth direction z beneath the ridge by a full two-dimensional and an effective index calculation, respectively. The field distributions and propagation constants for both methods equal each other.

5.1.3 Confinement Factor

If complex material indices are inserted in the wave equation (5.7) *a priori*, the complex result for n_{eff} already contains the effective modal index and modal absorption or gain. To avoid complex calculations, the confinement factor is a convenient way of linking material and modal absorption, absorption change, gain or index change under the assumption that the mode profile is not affected by small changes. It originates from first-order perturbation

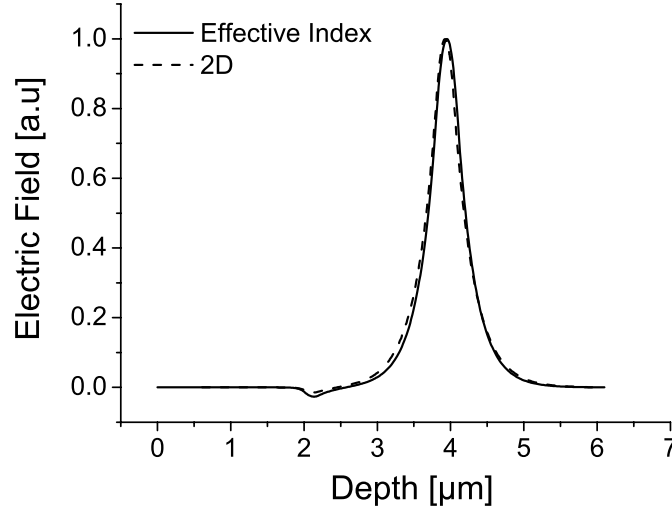


Fig. 5.4: Calculated field distribution along the growth direction z beneath the ridge waveguide, by 2D calculations (compare Fig. 5.2) and the effective index method. The overall effective index is 3.264 for both methods.

theory, describing the overlap between a certain layer and the optical mode and is defined as [10, 2]:

$$\Gamma = \frac{\int \int_{\text{layer}} |H(y, z)|^2 dy dz}{\int \int |H(y, z)|^2 dy dz} \quad (5.9)$$

If material properties like absorption, gain or index of a certain layer are subject to changes, the corresponding modal absorption, gain or effective index change can be determined without repeated eigenvalue calculations:

$$\tilde{\alpha}, \tilde{g}, \Delta n_{\text{eff}} = \Gamma \cdot \alpha, g, \Delta n \quad (5.10)$$

Γ	confinement factor of layers of interest, $\approx 10\%$ to 15% for a QW stack
$\tilde{\alpha}, \tilde{g}, \Delta n_{\text{eff}}$	modal change in absorption, gain or index
$\alpha, g, \Delta n$	material change in absorption, gain or index

5.1.4 Coupled Wave Equation and DFB Spectra

A periodical grating along a waveguide acts as a distributed reflector, see Fig. 5.3(c). The reflectivity per unit length of a waveguide grating is referred to as the coupling coefficient κ .

For phase matching conditions and with the well-known field reflection coefficient between two transparent media (5.1), it is expressed as [2, 30]:

$$\kappa = \frac{1}{\Lambda} \frac{H^-}{H^+} = \frac{1}{\Lambda} 2 \frac{n_{\text{eff},1} - n_{\text{eff},2}}{n_{\text{eff},1} + n_{\text{eff},2}} = \frac{\Delta n_{\text{eff}}}{\Lambda \bar{n}_{\text{eff}}} = \frac{\Gamma_{\text{Grat}} \Delta n_{\text{Grat}}}{\Lambda \bar{n}_{\text{eff}}} \quad (5.11)$$

κ	coupling coefficient, e.g. $\approx 72/\text{cm}$
Λ	grating period, $\approx 200 \text{ nm}$ at 1300 nm operation
Δn_{eff}	grating induced effective index modulation, $\approx 4.7 \cdot 10^{-3}$
\bar{n}_{eff}	waveguide average effective index, ≈ 3.29
Δn_{Grat}	grating matrix and filling material index difference, = 0.076 between InP and lattice matched, 1050 nm PL GaInAsP material = $0.2 + j5.76$ between Ni and BCB
Γ_{Grat}	grating layer confinement, e.g. = 6%

Note that the coupling coefficient may become complex if the index change itself is complex, that is if the reflection is not only due to index but also due to absorption or gain variations. This case is referred to as ‘complex coupling’, while otherwise the coupling is called ‘real’ or ‘index’ coupling.

To calculate the longitudinal field distribution along an arbitrary waveguide with a periodical disturbance and constant optical gain, the coupling coefficient of a waveguide enters the coupled wave equations for the forward and reverse traveling wave envelopes [2, 30]:

$$\frac{d}{dx} \hat{H}^+(x) = (\tilde{g}/2 - j\delta) \hat{H}^+(x) + j\kappa \hat{H}^-(x) \quad (5.12)$$

$$-\frac{d}{dx} \hat{H}^-(x) = (\tilde{g}/2 - j\delta) \hat{H}^-(x) + j\kappa \hat{H}^+(x) \quad (5.13)$$

δ	wave number mismatch to Bragg wave number, $= \frac{2\pi n_{\text{eff}}}{\Lambda} - \frac{\pi}{\Lambda} \approx 10^{-3}/\text{m}$
$\hat{H}^+(x)$	forward traveling wave envelope
$\hat{H}^-(x)$	reverse traveling wave envelope

These equations simply point out that changes in the forward traveling wave envelope $d\hat{H}^+/dx$ result from forward amplification of the incident wave $\tilde{g}\hat{H}^+/2$ and reflections from the reverse traveling wave $j\kappa\hat{H}^-$. Additionally, phase changes over one grating period $j\delta\hat{H}^+$ are caused by a mismatch to the Bragg wavelength. Equations (5.12) and (5.13) can be solved analytically [2, 30].

One application of the solutions of (5.12) and (5.13) is the field reflectivity and transmission of a DFB mirror with an additional facet reflection in the presence of coupling and gain [2, 30], see either part of Fig. 5.5:

$$r^{\text{Field}} = \frac{\hat{H}^-(0)}{\hat{H}^+(0)} = \frac{j \frac{\kappa}{\beta_e} \sin(\beta_e l_{\text{Grat}}) + \frac{r_f^{\text{Field}}}{\cos(\beta_e l_{\text{Grat}}) - \frac{\tilde{g}/2 - j\delta}{\beta_e} \sin(\beta_e l_{\text{Grat}}) - j r_f^{\text{Field}} \frac{\kappa}{\beta_e} \sin(\beta_e l_{\text{Grat}})}}{\cos(\beta_e l_{\text{Grat}}) - \frac{\tilde{g}/2 - j\delta}{\beta_e} \sin(\beta_e l_{\text{Grat}})} \quad (5.14)$$

$$t^{\text{Field}} = \frac{\hat{H}^+(l_{\text{Grat}})}{\hat{H}^+(0)} = \frac{1 + r_f^{\text{Field}}}{\cos(\beta_e l_{\text{Grat}}) - \frac{\tilde{g}/2 - j\delta}{\beta_e} \sin(\beta_e l_{\text{Grat}}) - j r_f^{\text{Field}} \frac{\kappa}{\beta_e} \sin(\beta_e l_{\text{Grat}})} \quad (5.15)$$

$$\beta_e = \sqrt{(\delta + j\tilde{g}/2)^2 - \kappa^2} \quad (5.16)$$

r^{Field}	complex field reflection coefficient, absolute value may exceed unity!
t^{Field}	complex field transmission coefficient, absolute value may exceed unity!
r_f^{Field}	complex facet field reflection, e.g. $ r_f^{\text{Field}} = 0.53$ for uncoated facets
l_{Grat}	length of grating, e.g. $150 \mu\text{m}$

The phase of the facet reflectivity depends on the exact cleaving position within the grating period and varies from device to device. Zero phase is defined exactly at the center of the low refractive index layers.

Now, the reflectivity of two single DFB mirrors can be used to calculate the output spectrum of a DFB laser diode. Figure 5.5 illustrates this procedure. First, the DFB laser of length l_{LD} is divided into two parts. The point of separation is arbitrary, but for mathematical stability it is chosen at the center of the cavity. The method is extended to an arbitrary number of sections by including a transfer matrix approach.

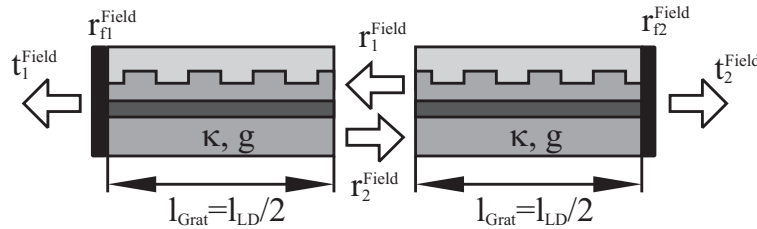


Fig. 5.5: Outline of the ‘bouncing equation’.

The reflection and transmission coefficients of both distributed mirrors are given by equations (5.14) to (5.16). Now, the output spectrum can be determined in a fashion similar to Fabry-Perot lasers. Beginning with spontaneous excitation P_{in} in the center of the cavity, light can leave the cavity by direct transmission t_1^{Field} , after one round trip $r_1^{\text{Field}} r_2^{\text{Field}} t_1^{\text{Field}}$ or after a higher number n of round trips $(r_1^{\text{Field}} r_2^{\text{Field}})^n t_1^{\text{Field}}$. If initial emission is in the opposite

direction, light is emitted after being reflected once $r_2^{\text{Field}} t_1^{\text{Field}}$ or after one or more round trips $(r_2^{\text{Field}} r_1^{\text{Field}})^n r_2^{\text{Field}} t_1^{\text{Field}}$. Combining the resulting geometric series, the final result for the DFB emission spectrum is obtained as:

$$P_{\text{out}}(\lambda) = \frac{|t_1^{\text{Field}}|^2}{|1 - r_1^{\text{Field}} r_2^{\text{Field}}|^2} (1 + |r_2^{\text{Field}}|^2) P_{\text{in}}(\lambda) \quad (5.17)$$

P_{out}	spectral power density of optical output in [W/nm]
P_{in}	spectral power density of optical input in [W/nm]

Note that all reflection and transmission coefficients are wavelength dependent. Equation (5.17) can be used in two ways. First, to simulate a continuous DFB laser spectrum by sweeping the wave number mismatch δ and keeping the cavity gain at an arbitrary but fixed level below the laser threshold. Second, to determine emission wavelength and threshold gain of the discrete DFB laser modes by finding the complex zeroes of the denominator varying wavelength and cavity gain. In contrast to a Fabry-Perot laser simulation, both wavelength and gain affect absolute value and phase of the complex term. For more exact spectral calculations, the cavity has to be divided into multiple sections, each with a gain value of its own due to non-uniform pumping and amplification ('spatial hole burning'). Comparison to measured spectra shows that for the low excitation in integrated laser modulators, (5.17) is an adequate simplification.

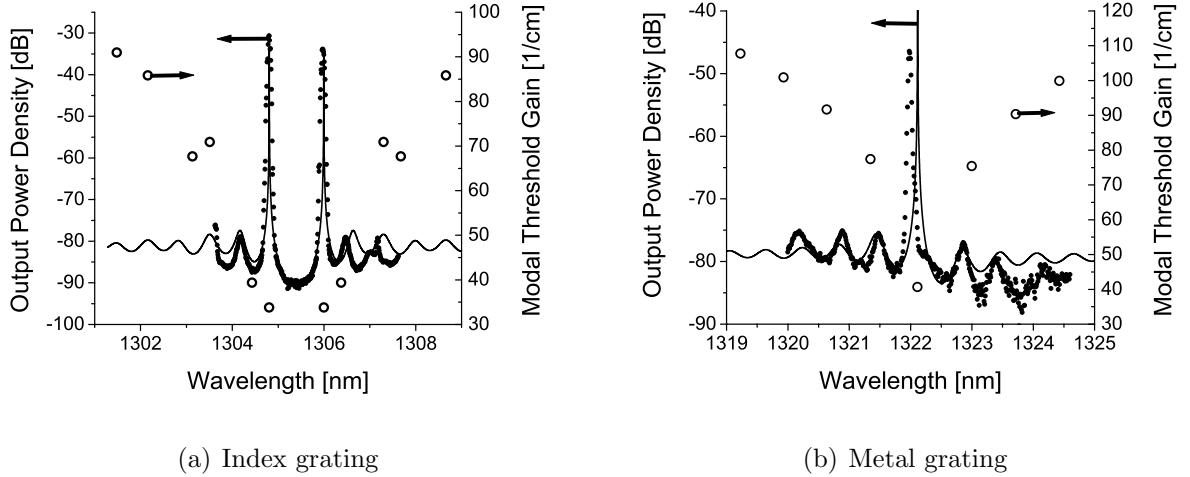


Fig. 5.6: Measured (dots) and simulated (line) DFB spectra of index and metal coupled DFB lasers. Facets are high-reflection (HR, $r_{\text{fl}}^{\text{Field}} = 0.8e^{\pm j\pi/2}$) and anti-reflection (AR, $r_{\text{f2}}^{\text{Field}} = 0$) coated, respectively, and the lasers are $380 \mu\text{m}$ long. The coupling coefficients are $34/\text{cm}$ and $j 15/\text{cm}$, the grating periods are 198.6 nm and 201 nm . The waveguide's effective indices are 3.287 and 3.289 . The circles correspond to the modal threshold gains.

Figure 5.6 shows two typical DFB spectra with corresponding threshold gains for index and metal grating, respectively. Index gratings without an additional phase shifting section

show the typical double-mode behavior, as the round trip phase is destructive exactly at the Bragg wavelength. The peaks will vary in amplitude if the phase of the high-reflecting facet is changed. This feature severely limits the yield of index coupled laser diodes, as a sidemode suppression ratio of 30 dB is usually demanded for system applications

Side Note: In this model, the threshold gain of complex coupled devices may become negative. This is due to the fact that only the *modulation* of absorption or gain $\Delta\alpha = -\Delta g$ enters the complex coupling coefficient. Its *mean* value is not considered, which is equal to a modulation around zero absorption. Thus, it is not possible to distinguish between gain and absorption modulation if only the coupling coefficient is known. As the standing resonator wave will position itself in such a way that its maxima coincide with the gain maxima, it will always undergo a net amplification. Thus, negative threshold currents can result for high coupling strengths. The mean absorption of a metal grating imposes additional losses that have to be added to the gain budget manually. For reasonable grating duty cycles, it is approximately equal to half the coupling coefficient [30].

5.2 Single-Mode Yield Analysis

As discussed by round trip phase arguments in the preceding sections, index grating DFB lasers will intrinsically feature two resonator modes with equal threshold, whereas metal grating DFB lasers tend to have only one central mode. Now, a mathematical evaluation is presented that takes into account the additional influence of the resonator facets. In a laser

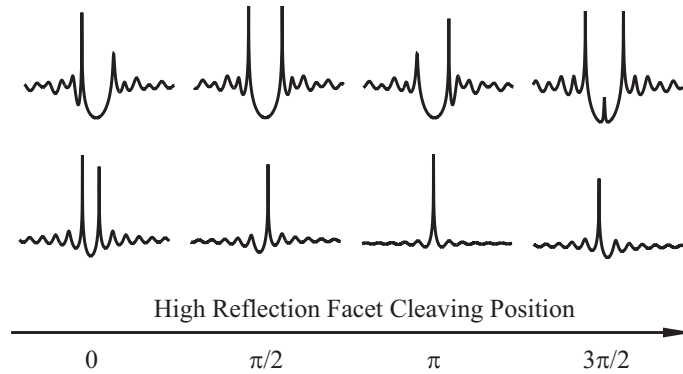


Fig. 5.7: Simulated DFB spectra in arbitrary units as a function of the high-reflecting ($r_{\text{fl}}^{\text{Field}} = 0.8e^{\pm j\theta}$) facet cleaving position for index (top) and metal (bottom) coupled gratings. The second facet is anti-reflection ($r_{\text{f2}}^{\text{Field}} = 0$) coated and the lasers are $380\mu\text{m}$ long. The coupling coefficients are 80/cm and j 15/cm, respectively. Cleaving at the center of a layer with low refractive index refers to zero phase.

diode, the facets cleaving positions play a major role in the modal behavior as they break the cavity's symmetry. Usually, the facets are high-reflection (HR) and anti-reflection (AR)

coated, respectively. In this case, the position of the HR facet has the dominating influence on the laser spectrum. Figure 5.7 shows the emission spectra of comparable index and metal coupled DFB lasers for variations of the HR facet's cleaving position. For practical purposes, single-mode operation is often defined by a sidemode suppression ratio (SMSR) of 30 dB. Obviously, the metal coupled grating has a much larger single-mode range. Figure 5.8 converts

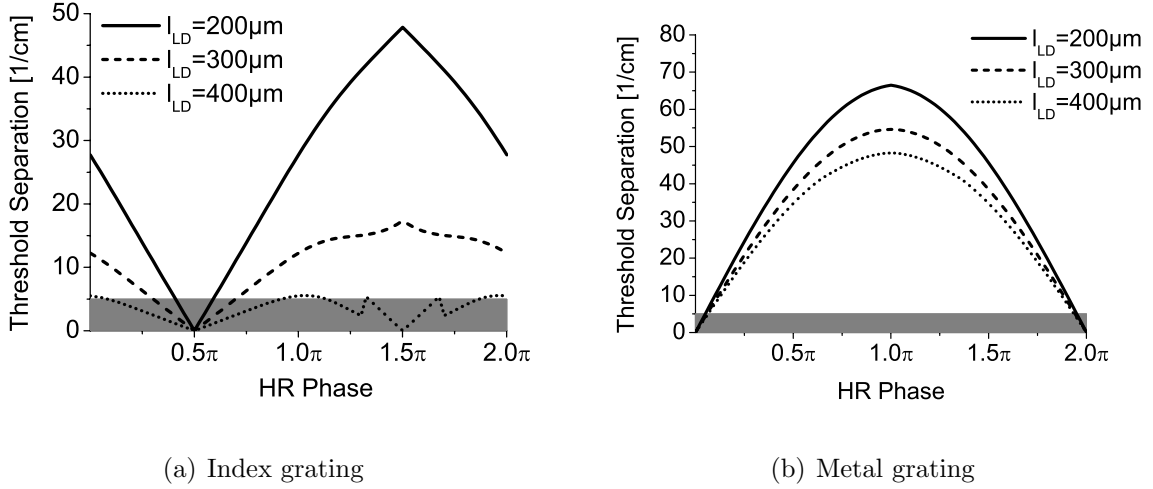


Fig. 5.8: Simulated threshold gain difference of the two dominant resonator modes for a variable HR facet cleaving position. Input data are similar to Fig. 5.7

this qualitative statement into quantitative numbers. It shows the threshold gain difference of the two dominant resonator modes for different laser lengths, again for variations of the HR facet's cleaving position. For a good agreement with experimental results, a threshold gain difference of 5/cm was chosen as the single-mode limit.

Today, the exact positioning of a facet within a grating period is beyond the technological limit. Therefore, the single-mode range in terms of facet positions with a threshold separation exceeding 5/cm divided by 2π is equal to the single-mode yield percentage in laser production. Figure 5.8 clearly reveals that the possibility of finding a single-mode metal grating laser is over 95%, while there is a strong tendency to multi-mode behavior in long index lasers with $\kappa l_{LD} > 3$. Finally, Fig. 5.9 shows the experimental yield of standard index DFB lasers and integrated EMLs in comparison to the theoretical limit. The strong tendency to higher yield with shorter laser length is obvious for both. In contrast, all observed metal coupled EMLs showed longitudinal single-mode behavior.

Side Note: It has to be mentioned that the spectral quality of metal coupled DFB lasers has its price. Featuring two equal modes, the index laser always prefers the mode with constructive facet interference. In contrast, the metal grating laser is limited to its fundamental mode, even if it suffers from destructive facet interference. While the threshold gain is almost independent of the facet position for index grating lasers, there is a strong increase in laser

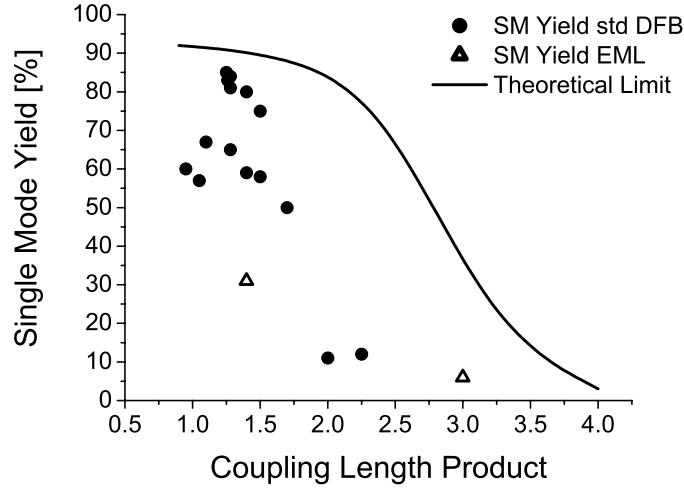


Fig. 5.9: Experimental and simulated yield of standard DFB lasers (over 1000 production devices, [31]) and index coupled EMLs (roughly 30 devices, [24]).

threshold for metal grating lasers for a wide range of cleaving positions. For example, the threshold gain of the lasers of Fig. 5.7 varies between 23 and 28/cm for index and 35 and 55/cm for metal gratings, respectively.

5.3 Optical Feedback

If light is reflected back into a laser diode, laser properties like threshold current or emission spectrum will change since light feedback is equal to a variation in effective facet reflectivity. This has to be avoided in integrated laser modulators as modulated optical feedback will cause laser resonances or even chaotic behavior. Therefore, the modulator facet requires a very good anti-reflection (AR) coating, and internal reflections between the individual device sections must be weak. Multi-mode devices with small sidemode suppression are especially susceptible to chaotic mode switching with EAM bias variations.

5.3.1 Facet Reflection and Coating

Figure 5.10 sketches two effects of optical feedback in integrated laser modulators. Light is generated in the laser, travels through the modulator, is reflected at the end facet and reaches the laser again after passing the modulator a second time. By changing the modulator voltage, amplitude and phase of the reflection are controlled. For static operation like in Fig. 5.10(a), the laser threshold current strongly depends on the modulator voltage. Instead of a simple amplification or damping of the laser signal, the modulator influences the laser via optical feedback. The dynamic small signal measurement in Fig. 5.10(b) exhibits strong resonances close to the laser resonance frequency for the modulator in short-circuit operation.

After increasing the absorption, the effect disappears.

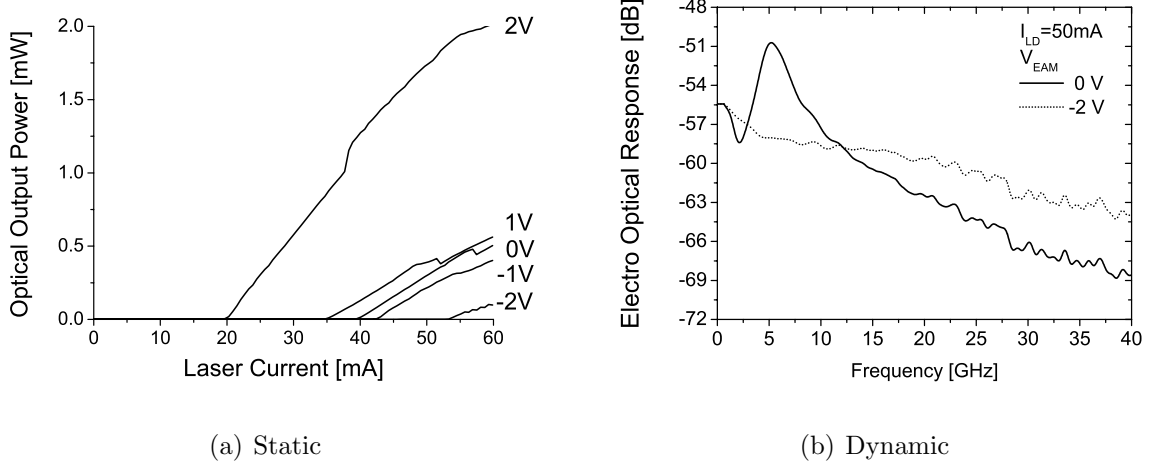


Fig. 5.10: Static (uncoated device) and dynamic (1% anti-reflection coating) influence of optical feedback on device D.

With this information, it is possible to estimate the critical amount of optical feedback. The modulator showed a residual absorption of ≈ 6 dB. The facet features a single layer anti-reflection coating, giving it a reflection damping of ≈ 15 dB. The extinction ratio to -2 V was 14 dB. This indicates that an optical feedback of -27 dB is still critical, while an isolation of 55 dB is sufficient. This result conforms to the estimations in [10]. For proper function, the anti-reflection coating must exhibit a reflection coefficient well below 0.1%. Possibly, other reflection reducing methods like tilted waveguides or window structures have to be introduced as well, especially for low residual absorption devices or additional amplifier integrations.

5.3.2 Internal Waveguide Reflections

The following sections will focus on internal waveguide disturbances and their corresponding reflectivity. Reflections along the waveguide are only critical if their reflectivity is subject to changes under modulation or if they occur after the modulator output, for example in an additional amplifier section.

Segment Separation In this work, electrical isolation between two segments is realized by a $6 \mu\text{m}$ long etched trench in the ridge [32]. In contrast to a local diffusion of acceptor atoms [33], this provides very high and defined electrical isolation but acts as a source of optical reflection, too. Figure 5.11 summarizes both competing features (note that the etch depth given in Fig. 5.11 includes the 200 nm thick contact layer). The p-region has a specific resistance of $0.13 \Omega\text{cm}$. The reflection is estimated by the effective index method that is valid for small disturbances. In this worst case scenario, the separation is etched vertically and both reflections on either side of the trench add up constructively. Reflectivities as low as

-50 dB are obtained for high isolation resistances of 20 k Ω . This is the preferred design figure. For higher electrical isolations with equal reflectivity, the etch trench must be increased in length.

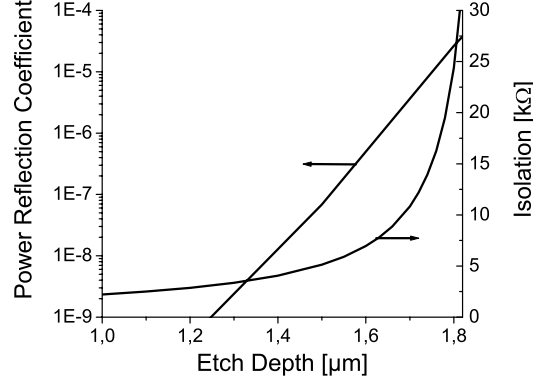


Fig. 5.11: Calculated worst case reflectivity and electrical isolation of the segment separation.

Interface: Forward to Reverse Driven Waveguide The refractive index may change from the laser to the modulator section without any geometrical variation due to the material refractive index change of forward and reverse driven active regions. According to equation (3.17), a maximum effective index variation of 10^{-3} is expected switching from forward bias to zero bias and from zero bias to reverse bias, respectively. This results in reflectivity modulations at the laser modulator intersection of

$$|\Delta r| = \left| \frac{dr}{dn_{\text{eff}}^{\text{EAM}}} \Delta n_{\text{eff}}^{\text{EAM}} \right| \approx \frac{\sqrt{r}}{n_{\text{eff}}^{\text{LD}}} |\Delta n_{\text{eff}}^{\text{EAM}}| < -80 \text{ dB} \quad (5.18)$$

This reflectivity modulation cannot be the origin of optical feedback.

Interface: Standard to Deeply Etched Ridge Waveguide This intersection probably introduces the highest reflectivity due to the strong change in device geometry. Both waveguides are shown in Fig. 6.11 on page 75. Unfortunately, including taper and strong guiding, it may only be evaluated by a sophisticated field analysis. The effective index method produces a reflectivity of $r = -60 \text{ dB}$ for a refractive index change of 0.007 from standard to deeply etched ridge waveguides ($n_{\text{eff}}^{\text{Side}} = 1.5$). This result is only a first approximation and should be reconsidered for the introduction of additional sections after the modulator output.

5.4 Surface Roughness Scattering

Apart from absorption, guided mode power may be lost due to scattering processes in radiation modes. Scattering takes place due to the roughness of waveguide layers or sidewalls.

As a detailed focus on scattering mechanisms is not possible within this work, only an expression derived in [34] was evaluated. Figure 5.12 shows a scanning electron microscope

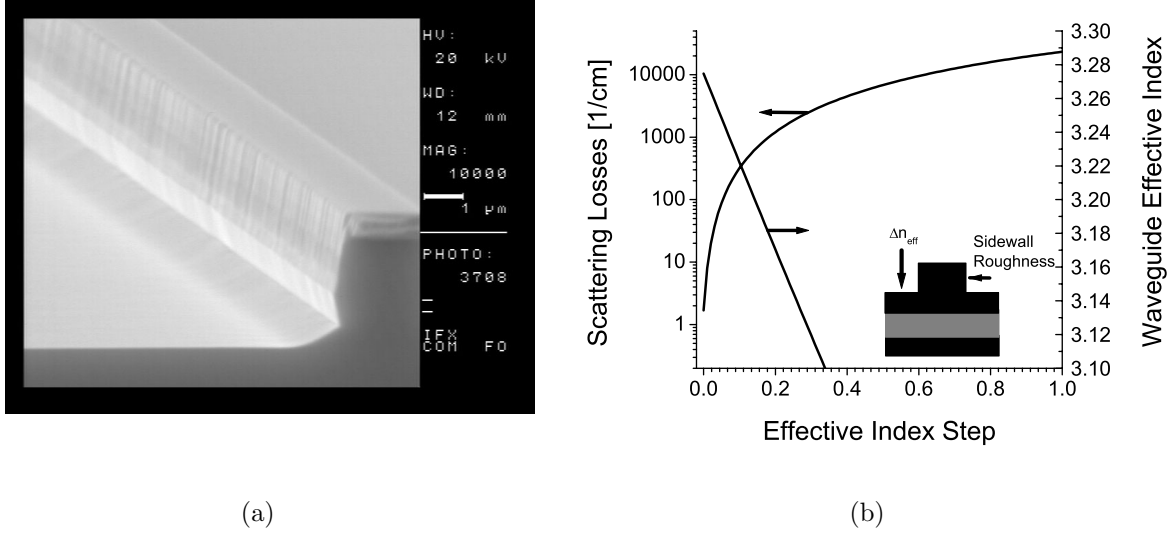


Fig. 5.12: (a) SEM picture of sidewall roughness. (b) Calculated ridge waveguide scattering at 1310 nm.

(SEM) picture of a ridge waveguide sidewall and the calculated scattering coefficient. The mean sidewall roughness is estimated to be 20 nm, the correlation length 1 μm. For standard ridge waveguides with an index profile of around 0.015 and a 2 μm wide ridge, the scattering loss coefficient is $\alpha_i = 15/\text{cm}$. This is consistent with the long wavelength tail of Hakki-Paoli gain measurements.

The figure also indicates that the scattering losses rise dramatically for higher index contrasts as in deeply etched modulators ($\Delta n_{\text{eff}} = 1.8$). This is due to a strong overlap of the guided mode with the rough area and the presence of multiple lateral modes. Although strong guiding waveguides are out of the validity range of Fig. 5.12, scattering will be a severe problem if fabrication roughness cannot be avoided.

Chapter 6

Design and Fabrication of EMLs with Shared Active Area

Modern optical communication systems comply with the standards set by the International Telecommunication Union (ITU). They vary depending upon link distance and the bit rate employed. In 2001, the ITU proposed a draft standard for 40 Gbps systems [35]. The physical background of these specifications is discussed in Section 6.1. To qualify as a product, an optical transmitter has to fit all the requirements specified by this standard, and therefore they are chosen as design guidelines throughout this chapter. The design and manufacturing process can be divided into three parts: epitaxy, chip technology and packaging.

Epitaxial growth is the deposition of lattice matched or strained semiconductor layers on a substrate. The layers define *intrinsic* material properties such as absorption, gain and intrinsic modulation behavior as well as waveguiding in vertical direction. The design of the layer stack compositions and thicknesses are described in Section 6.2. As most semiconductor optical parameters are wavelength dependent, choice of operating wavelength is the most critical design parameter in an electroabsorption modulated laser (EML). This is especially true for shared active area EMLs, and hence a detailed treatment is to be found in Section 6.2.2. Simulation tools based upon the results of Chapters 3 and 4 were applied to find a proper trade-off between laser and modulator performance of the active region. Finally, two epitaxial material structures I and II are proposed in Sections 6.2.3 and 6.2.4, respectively. The operating wavelength is defined by a periodic grating along the propagation direction, which can be either an etched-and-overgrown semiconductor grating below the ridge waveguide or a post-growth-defined metal grating placed adjacent to the ridge. The impact of grating technology is presented in Section 6.3.1. For the first time, EMLs with complex metal coupling were designed within this thesis.

After epitaxial material growth and grating technology, chip technology determines the device geometry by lithographically defined etching and deposition techniques. Besides lateral waveguiding, the geometry is responsible for *extrinsic* parameters such as interaction length, pad capacitance, current spreading or feed line impedance. They limit device performance in the majority of cases. The EML device layout is presented in Section 6.3. To distinguish

between epitaxial structures and device geometry layouts, Roman numbers (I to V) and Roman letters (A to D) are introduced, respectively.

6.1 Optical Standard

Table 6.1 lists an extract from the ITU draft standard for optical 40 Gbps transmitters [35]. These figures are used as design guidelines throughout this chapter.

	Unit	Value
Target distance	km	2
Encoding		NRZ 40 Gbit/s
Source		Single longitudinal mode (SLM)
Minimum SMSR	dB	35
Operating wavelength range	nm	1290-1330
Maximum mean output power	dBm	5
Minimum mean output power	dBm	2
Minimum extinction ratio	dB	10

Tab. 6.1: Extracts from the ITU-T G.959.1 draft optical transmitter standard

Before reaching the receiver, the optical signal is transmitted along a standard single-mode fiber (SSMF). Dispersion widens the pulse and attenuation adds to the power budget, see Table 6.2.

Wavelength	Attenuation $\frac{\text{dB}}{\text{km}}$	Dispersion $Disp \frac{\text{ps}}{\text{nm km}}$
1310 nm	0.5	-1 to +1
1550 nm	0.3 (EDFAs available)	+17

Tab. 6.2: Typical standard single-mode fiber (SSMF) data [36]. At 1550 nm, erbium doped fiber amplifiers (EDFAs) are available.

The minimum detectable power in an optical link is given by the detector sensitivity. Due to the large bandwidth and room temperature operation, thermal noise shows itself to be the predominant noise contribution. Being proportional to bandwidth ($N = k_B T \Delta f$, [1]), a 40 Gbps transmission needs 16 times more average power than a 2.5 Gbps transmission. Tables 6.1 and 6.2 point out that for high-speed applications, a minimum of approximately 1 mW average power is available at the receiver end (mean input power of 2 dBm and 1 dB fiber attenuation). The maximum input power is restricted by nonlinear optic effects in the fiber.

The broadening of optical pulses in the time domain Δt on a SSMF is proportional to the dispersion coefficient $Disp$ and the initial spectral width $\Delta \lambda$ and the link distance L [1]:

$$\Delta t = Disp \cdot \Delta\lambda \cdot L \quad (6.1)$$

Multi-mode transmitters feature a wide optical emission spectrum, making them unsuitable for high-speed transmission even for short reach applications. For example, a 40 Gbps pulse (corresponding to a full width at half maximum of 25 ps) is widened by $\Delta t = 34$ ps over $L = 1$ km of standard single-mode fiber at 1550 nm wavelength ($Disp = 17$ ps/(nm km)) for the typical DFB mode spacing of $\Delta\lambda = 2$ nm as shown in Fig. 5.6(a). This results in complete eye closure at the receiver. Therefore, lateral and longitudinal single-mode behavior (SLM) of the source is essential. A sidemode suppression ratio (SMSR) of at least 35 dB is demanded.

Single-mode devices themselves will be susceptible to dispersion broadening if amplitude modulation is accompanied by a positive frequency modulation, that is a rise in optical power causes a spectral blue shift of the emission wavelength. This behavior is called (positive) optical chirp [10]. Even for a low chirp parameter of +0.5 that typically shifts the laser wavelength by 0.25 nm at 40 Gbps operation [24], the maximum link distance of a 40 Gbps transmission at 1550 nm is approximately 2 km with pulse broadening of around one third of the initial pulse width. For negative chirp, the pulse is initially compressed and starts to broaden again after a certain link distance. Therefore, negative chirp is extremely useful for high-speed transmission over SSMFs at 1550 nm.

Dispersion is small at 1300 nm, but optical power limits the link distance as attenuation is higher and no erbium doped fiber amplifiers (EDFAs) are available. They are used to amplify the signal but cause a noise penalty for high power levels in the off-state. Therefore, extinction ratios must be as high as possible. Usually 10 dB extinction is sufficient.

This implies that for system applications, apart from cut-off frequencies of around 35 GHz, average output power of at least 1.6 mW (2 dBm), extinction ratio of 10 dB, sidemode suppression greater than 35 dB and zero or negative chirp values are desired. These are the design guidelines. Other semiconductor laser and modulator parameters like laser threshold current, laser slope efficiency or modulator residual absorption are of secondary interest. For example, a lower laser threshold current results in higher output power at a given pump current, but lower residual absorption may have the same effect.

6.2 Epitaxial Layer Design

To meet the requirements of Section 6.1, first the underlying epitaxial layer structure must be defined. Usually, a whole stack of layers is deposited on the InP substrate, each with a distinct functionality supporting laser or modulator operation. For example, QW layers deliver optical gain or absorption, confinement layers guide the optical wave and contact layers minimize the electrical series resistance. The performance of each layer usually depends on quantum mechanical effects like two-dimensional electron confinement in the QWs, tunneling through the barriers or Fermi level pinning at the contact interfaces. Thus, their dimensions and composition form the essential target of the design and optimization process.

This section will focus on this layer design procedure. Hereby, the challenge of shared active area EMLs lies in the fact that laser and modulator layer structure cannot be optimized individually. In contrast, most layer parameters will have an influence on the performance of both, laser and modulator. These dependencies are illustrated in Fig. 6.1. For example, if the number of QWs is increased (with all other parameters remaining constant) the modal gain for a given pump current in the laser section will be diminished (at least for practical laser modulator QW numbers of eight and above). Thus, the threshold current is increased and the optical output power is reduced. At the same time, residual absorption in the modulator rises for a given modulator length and bias point, further reducing the output power and having a negative impact on carrier pile-up related modulation constraints. On the other hand, the extinction ratio is increased. As a result, it would be possible to shorten the modulator section to maintain a desired extinction ratio, with a positive consequence for both, output power and modulation bandwidth.

Obviously, it is not possible to focus on single epitaxial parameters like QW number or wavelength detuning. Also, the choice of epitaxial parameters depends on the choice of device geometry data like laser and modulator lengths l_{LD} and l_{EAM} , and the choice of proper bias points for laser current I_{LD} and modulator voltage V_{EAM} . Thus, the whole set of unknowns must be treated simultaneously to optimize the final device performance.

The following procedure was identified as the most practical layer design sequence, beginning with the most intrinsic parameters:

1. QW layer thickness d_{QW} : As a rule of thumb, the wavefunction half-maximum width of the electron fundamental state should be minimal, guaranteeing sufficient electron confinement. This is equivalent to an optimal designed single-mode waveguide. A QW width of 5-7.5 nm is found to be the ideal figure for the electron mass of $m_e \approx 0.05 m_0$ of AlGaInAs on InP. For both thicker or thinner wells, the electron wavefunction spreads out again.

Note that there is no change in modal absorption $\Gamma\alpha$ or gain Γg for different QW thicknesses. Although a thicker QW features an increased optical confinement factor Γ proportional to d_{QW} according to equation (5.9), its material absorption amplitude α_0 is inversely proportional to d_{QW} in equation (3.4).

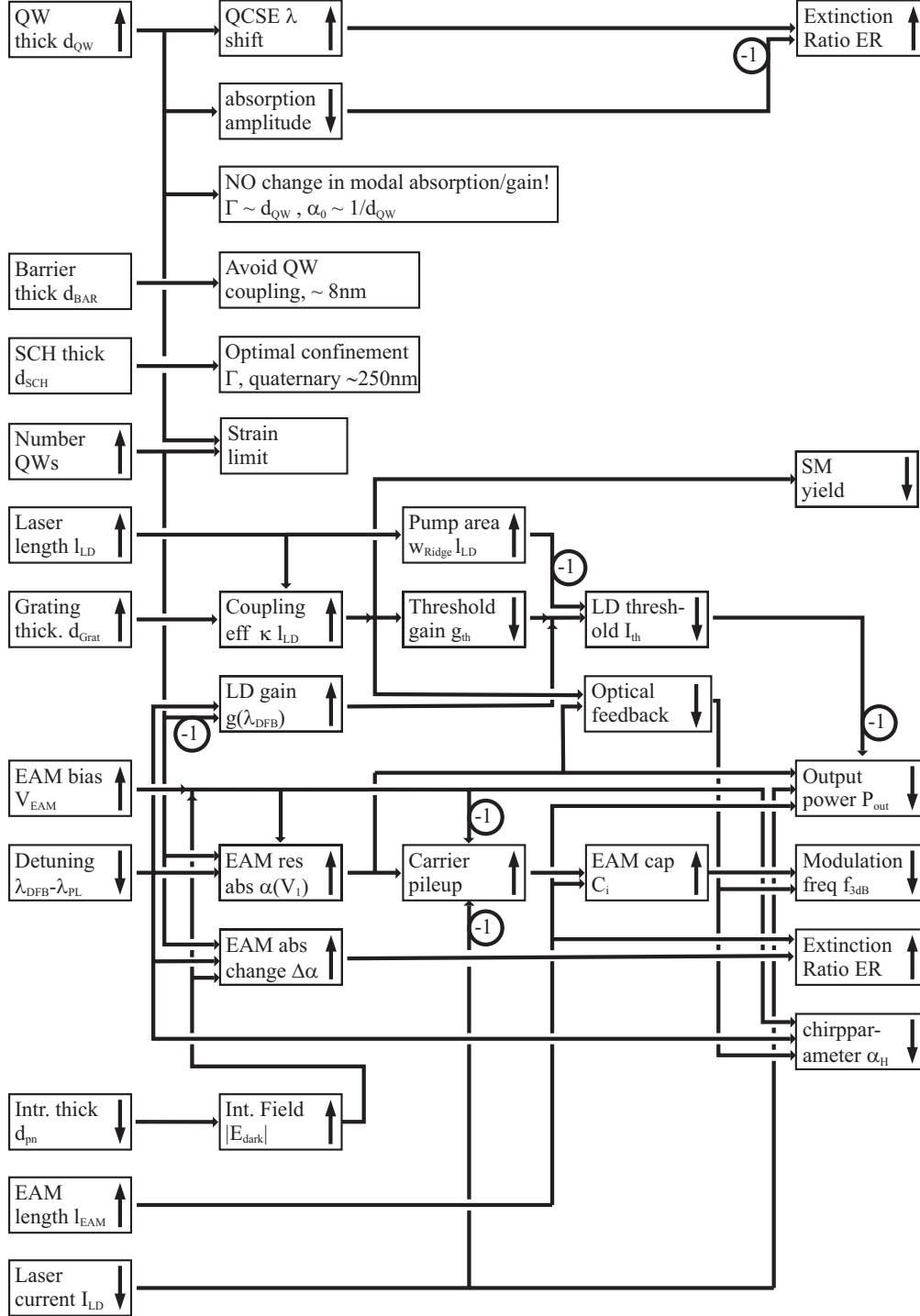


Fig. 6.1: Design restrictions. '-1' indicates a degradation.

In the EAM section, the wavelength shift induced by the QCSE is stronger for thicker QWs, but so is the reduction in wavefunction overlap. This is illustrated in Fig. 3.2 on page 14. Comparing graphs 1 and 3 of Fig. 3.7 shows that the absorption shift toward longer wavelengths is increased for thicker wells, but at the same time the absorption amplitude decreases faster with applied electric field. Thus, the resulting modal absorption modulation at a given wavelength is comparable for both, 5 and 7.5 nm thick QWs.

2. QW $\text{Al}_x\text{Ga}_y\text{In}_{1-x-y}\text{As}$ composition x, y : The composition defines photoluminescence (PL) wavelength and layer strain. High compressive strain is desired to separate heavy and light holes sufficiently. A composition of $x = 0.17$ and $y = 0.16$ of a 5 nm thick QW on InP substrate (with barrier compositions as described shortly) will result in a PL wavelength of 1290 nm and -0.95% compressive strain. According to Fig. 3.2 on page 14, this strain magnitude is sufficient to separate light and heavy hole transitions by more than 75 nm. Thus, the light hole influence on absorption and gain characteristics is negligible.
3. Barrier $\text{Al}_x\text{Ga}_y\text{In}_{1-x-y}\text{As}$ composition x, y : The energy barrier must be high enough for sufficient carrier confinement in the well, but as low as possible to enhance escape processes in the modulator section. A simple design rule is that the second electron level should be barely present in the well. Tensile strain in the barrier delivers strain compensation maximizing the number of QWs. In this work, $\lambda_{\text{PL}} = 1100$ nm and $+0.5\%$ tensile strain are chosen, which correspond to a composition of $x = 0.27$ and $y = 0.28$.
4. Barrier layer thickness d_{BAR} : The barriers are kept as thin as possible to enable maximum number of QWs with high optical confinement, but must be thick enough to avoid tunneling of the confined particles. A thickness of 8 nm is sufficient as the electron wavefunction is reduced to 1% at the adjacent well according to Fig. 3.3 on page 15. Thus, the wells can be considered decoupled and tunneling between them is negligible [12].
5. QW number: The thickness of the quaternary optical waveguide is around 300 nm for optimal confinement of the wave in vertical direction. The number of QWs is not restricted by this constraint, as it allows for more than 18 wells and 19 barriers. The practical limit is defined by the layer strain. In this work, a maximum number of QWs is used in order to minimize the modulator length and related capacitance. Since preliminary test devices at 1300 nm (high Al content) with a total thickness of the QW layers of 95 nm ($3 \times 5, 8 \times 10$ nm QWs) were destroyed due to strain, this thickness does not exceed 75 nm for the investigated devices.
6. Waveguide thickness d_{SCH} : Lattice matched, high index AlGaInAs separate confinement heterostructure (SCH) layers are added symmetrically to the stack of QWs and barriers in order to achieve optimal vertical waveguiding and thus maximum optical

confinement in the wells. Their thickness is varied until the total thickness of quaternary SCH, QW and barrier layers is 250 nm to 300 nm. This ensures optimal waveguiding at 1310 nm operating wavelength for an average material index contrast of $\Delta n = 0.25$ of AlGaInAs to InP [12]. Again, both thicker and thinner waveguides feature a larger mode diameter in vertical direction.

7. Thickness of intrinsic layers between p- and n-regions d_{pn} : The thickness of the intrinsic layers is varied by doping the SCH layers or adding undoped InP layers for optimal modulator performance in terms of extinction ratio and intrinsic capacitance. Since both of them are proportional to the internal electric field and thus inversely proportional to d_{pn} , there is a trade-off between the two competing optimization goals. The thickness of the intrinsic layers has no effect on continuous wave laser operation. For low capacitance and 10 dB/2 V extinction ratio, 270 and 300 nm are chosen.
8. Electron stop layer: An AlInAs layer with high conduction band (CB) discontinuity is added at the p-side of the intrinsic region. It blocks the electron leakage that originates from the absence of a CB offset of the aluminum containing SCH regions to the InP cladding material. Use of an electron stop layer is important for high-temperature performance of laser diodes. As the EML is mainly designed for temperature controlled operation and as the electron stop layer significantly increases lateral conductivity in the modulator section, its use should be reconsidered for future designs.
9. Holography grating layer thickness d_{Gat} : This parameter determines the coupling factor κ in the laser section. For low laser threshold currents and good single-mode yield, a κL -product of 1.5 is intended. Note that it causes lateral conductivity in the modulator section.
10. Contact, spacer and etch stop layers: Contact layers are highly doped, low bandgap materials for low contact resistance. Due to their low bandgap and high refractive index, they cause anti-guiding as well as additional losses. Spacer layers must be added to reduce optical overlap of the contact layer with the lasing mode. Spacer layers should be as thin as possible because of an increase in series resistance and epitaxial growth time. In this work, $1.6 \mu\text{m}$ and $1 \mu\text{m}$ were identified as sufficient spacing on the p- and n-sides of the active area, respectively, reducing the optical confinement of the contact layers below 0.1%. Etch stop layers are introduced for wet chemical ridge definition. Their position ensures lateral single-mode behavior ($\Delta n_{\text{eff}} < 0.02$ for $2 \mu\text{m}$ wide ridges at 1300 nm operating wavelength). In this design, the remaining grating layer itself acts as a ridge etch stop in order to reduce the lateral conductance. Another spacer is needed between Al and P quaternary materials since they are grown at different temperatures.

A typical layer structure of an overgrown EML is listed in Table 6.3. Except for the intrinsic region (layers 4 to 26), the layer structure is valid for all samples of this work. A schematic

view of the processed device is provided in Fig. 6.2.

#	Function	Material	Thickness [nm]	Bulk λ_{PL} [μm]	Strain ε_{xx} [%]	x	y	Doping N_D $10^{18}/\text{cm}^3$
32	p-contact	Ga_xInAs	200	1.65	+0.6(t)	0.557		-2.0 (p)
31	Cladding	InP	1600					-0.5 (p)
30	Grating 1	InP	45					-0.5 (p)
29	Grating 2	$\text{Ga}_x\text{InAs}_y\text{P}$	130	1.05	0	0.137	0.301	-0.5 (p)
28	Spacer	InP	10					-0.5 (p)
27	El.stop	Al_xInAs	18	0.87	0	0.47		-0.5 (p)
26	SCH	$\text{Al}_x\text{Ga}_y\text{InAs}$	80	1.05	0	0.315	0.157	
	11 \times Bar	$\text{Al}_x\text{Ga}_y\text{InAs}$	8	1.10	+0.5(t)	0.265	0.278	
	10 \times QW	$\text{Al}_x\text{Ga}_y\text{InAs}$	5	1.29 ¹	-0.95(c)	0.170	0.159	
4	SCH	$\text{Al}_x\text{Ga}_y\text{InAs}$	80	1.05	0	0.315	0.157	
3	Spacer	InP	1000					+1.0 (n)
2	n-contact	$\text{Ga}_x\text{InAs}_y\text{P}$	200	1.2	0	0.25	0.55	+10 (n)
1	Buffer	InP	1000					+2.0 (n)
	Substrate	InP	360 μm					n or s.i.

Tab. 6.3: Typical layer structure. Nominal intrinsic layers have n-type background doping of $\approx 5 \cdot 10^{16}/\text{cm}^3$. The PL wavelength varies by approximately 40 nm across a 2 inch wafer. The material compounds are written as $\text{Ga}_x\text{In}_{1-x}\text{As}$, $\text{Ga}_x\text{In}_{1-x}\text{As}_y\text{P}_{1-y}$, $\text{Al}_x\text{In}_{1-x}\text{As}$ and $\text{Al}_x\text{Ga}_y\text{In}_{1-x-y}\text{As}$ for the sake of completeness. ¹ QW PL includes confinement energy, QCSE due to the built-in field and exciton energy.

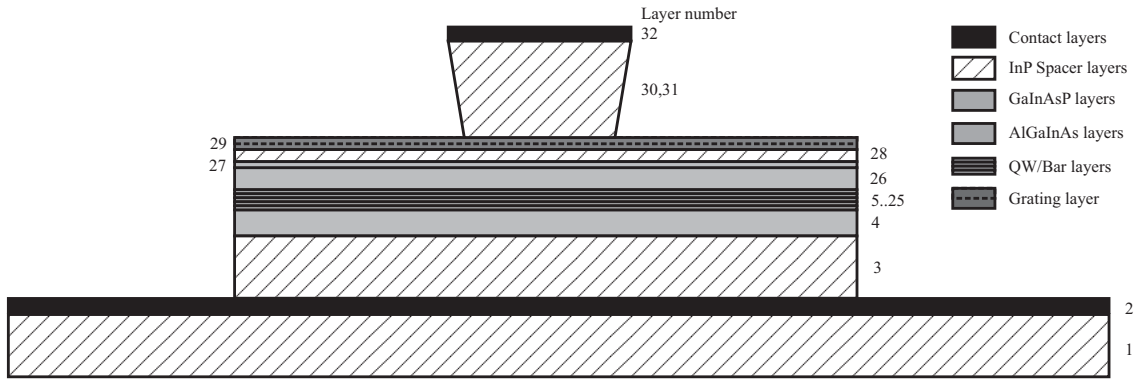


Fig. 6.2: Schematic of the layer structure after wafer processing. Layer numbers correspond to Table 6.3.

6.2.1 EAM Static Figure of Merit

Since both, logarithmic residual absorption in the ON-state and extinction ratio, are proportional to the modulator length, absorption change divided by residual absorption is a

reasonable figure of merit (*FoM*) definition to describe static modulator performance.

$$\begin{aligned}
 FoM(V_{\text{EAM}}, V_{\text{pp}}) &= \frac{\alpha(V_{\text{EAM}} - V_{\text{pp}}/2) - \alpha(V_{\text{EAM}} + V_{\text{pp}}/2)}{\alpha(V_{\text{EAM}} + V_{\text{pp}}/2)} = \frac{\Delta\alpha}{\alpha(V_1)} \\
 &= \frac{\text{extinction ratio [dB]}}{\text{insertion loss [dB]}}
 \end{aligned} \tag{6.2}$$

FoM	static figure of merit, typically -1 to 4
α	modal OR material absorption coefficient
$\Delta\alpha$	modal OR material absorption change
V_{EAM}	EAM bias voltage, typically -1 to -2 V in this thesis
V_{pp}	peak-to-peak driver voltage swing, typically 2 V in this thesis
V_1	driver voltage at ON-state, $= V_{\text{EAM}} + V_{\text{pp}}/2$

Residual absorption and extinction ratio (ER) are defined in Section 5.1. For design purposes, the operating wavelength is chosen at the maximum *FoM*. Then, the modulator length is varied to meet the desired extinction ratio. A maximum *FoM* corresponds to a maximum in output power for a given extinction ratio.

Another advantage of this definition is that the *FoM* can be measured with low error by the absorption measurement procedure given in Section 3.4. Constant calibration factors will cancel out due to the ratio of two absorptions. Therefore, the *FoM* is directly proportional to the corresponding photocurrents. In the same way, neither the number of QWs in the device nor optical reflections influence the *FoM*. Additionally, even modal absorptions measured on a waveguide structure can be used as input data.

6.2.2 Choice of Detuning

In conjunction with the waveguide effective index, the grating period determines the lasing wavelength. Its detuning to the QW PL wavelength is the most critical design parameter and will be carefully evaluated in this section. Modal gain, residual absorption, extinction ratio, figure of merit, modulator bias range, switchable optical power and chirp parameter all depend on the detuning value as illustrated in Fig. 6.1.

Figures 6.3 and 6.4 show the values of various design parameters for different modulator bias voltages as a function of detuning for the layer structure of Table 6.3 and a typical device geometry. All graphs are calculated after gain and absorption calibrations described in Chapters 3 and 4. The driver voltage swing is $V_{\text{pp}} = 2$ V. Thus, -2 V bias voltage graphs correspond to modulation between -1 V (ON-state) and -3 V (OFF-state). For example, a detuning of 30 nm and a modulator bias voltage of $V_{\text{EAM}} = -2$ V result in 7 dB residual loss, 14 dB extinction ratio, 18 mA laser threshold current and a zero chirp parameter. Note that absorption modulators with negative chirp are only feasible for either small detuning or

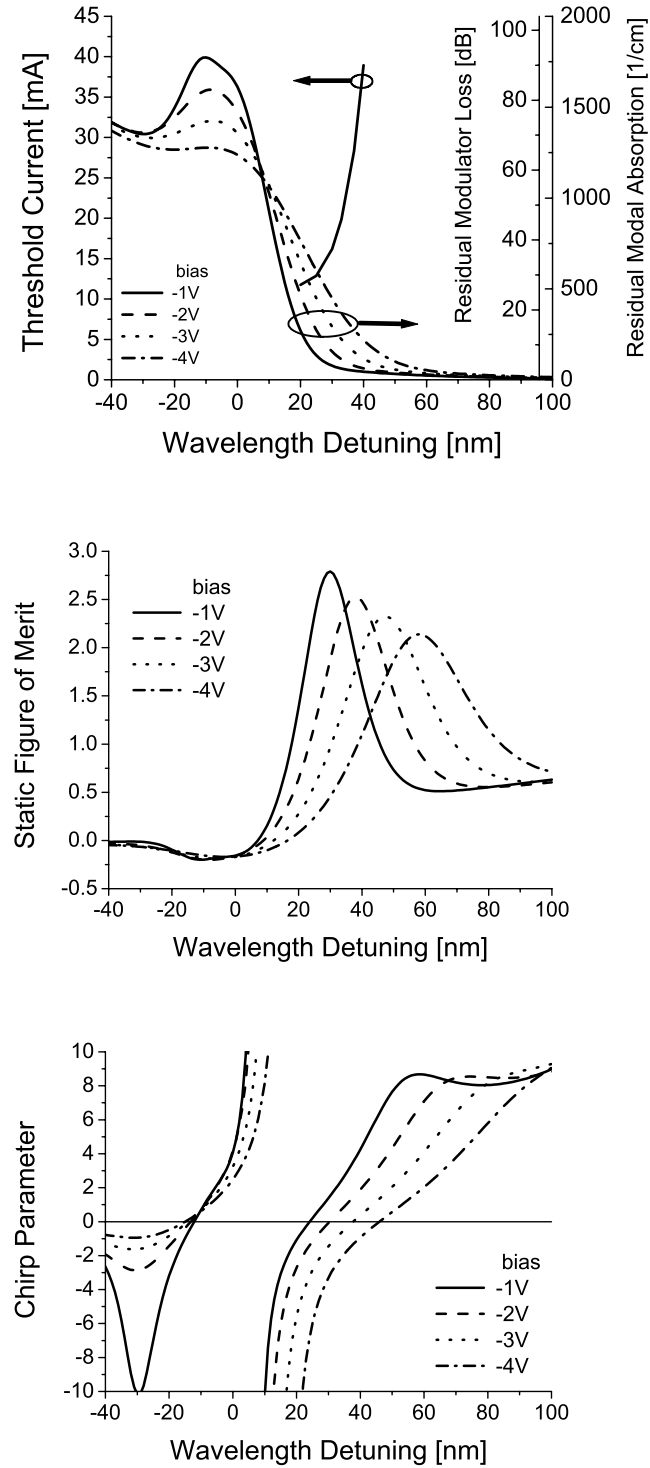


Fig. 6.3: Simulated laser and modulator parameters as a function of the modulator bias voltage V_{EAM} for $V_{\text{pp}} = 2\text{ V}$ peak-to-peak driver voltage swing. Calculations are performed according to Chapters 3 and 4 for the layer structure given in Table 6.3. The laser diode is $380\text{ }\mu\text{m}$ long and $2\text{ }\mu\text{m}$ wide. The modulator is $120\text{ }\mu\text{m}$ long. Note that the residual absorption for -1 V bias is the static 0 V absorption graph.

high bias voltage and thus limited output power. Since the absolute PL wavelength varies by approximately 40 nm across a two inch wafer, most wavelength dependent measurements will be presented as a function of detuning wavelength rather than using an absolute wavelength scale. This avoids confusion with numerous PL wavelengths encountered for a single design. Obviously, a similar FoM is achieved for different detunings by varying the bias voltage. For modulators with a free choice of PL wavelength, a high detuning of 50-70 nm is usually chosen to permit higher bias voltages. This lowers the carrier pile-up effect and enables a higher amount of switched power as well as faster switching speed with otherwise similar performance. The maximum optical input power into the EAM with negligible switching speed limitations is shown in Fig. 6.4. EMLs with identical active layer are restricted to a

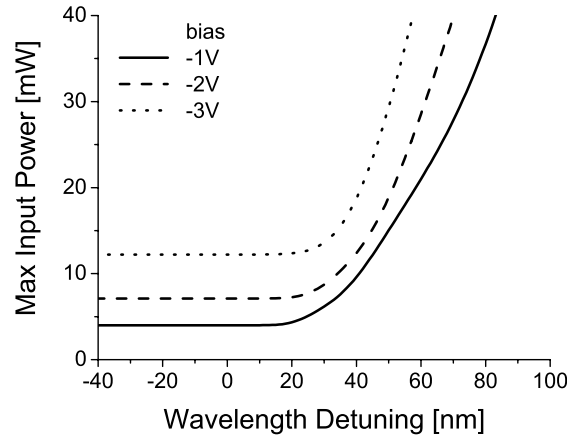


Fig. 6.4: Simulated maximum power coupled into the EAM for various bias voltages V_{EAM} and a $V_{pp} = 2$ V driver voltage swing. Maximum power is reached when the average absorbed power increases the intrinsic capacitance by 10% according to Fig. 9.5.

smaller detuning window of 30 nm to 50 nm to obtain reasonable threshold currents. Beyond 50 nm detuning, the available gain decreases rapidly and the threshold current approaches infinity. This has also been reported by [37]. This design issue imposes major drawbacks on residual absorption and switching speed, since large amounts of carriers are generated and the sweep out bias voltage is limited at the same time. On the other hand, high extinction ratios and low or even negative chirp can be achieved easily. This feature can be exploited for 10 Gbps negative chirp light sources at 1550 nm wavelength.

6.2.3 Epitaxial Layout I: Single QW Type Structure

Table 6.4 shows epitaxial layout I. The $d_{pn} = 300$ nm thick intrinsic layer stack has a low intrinsic capacitance and is at the upper limit for effective waveguiding at 1310 nm wavelength. 10×5 nm thick QWs are well below the total critical thickness and have a reasonable optical confinement factor of $\Gamma = 0.12$.

Epitaxial Layout I							
Function	Material	Thickness [nm]	Bulk λ_{PL} [μm]	Strain ε_{xx} [%]	x	y	Doping $10^{18}/\text{cm}^3$
SCH	$\text{Al}_x\text{Ga}_y\text{In}_{1-x-y}\text{As}$	80	1.05	0	0.315	0.157	
$11 \times \text{Bar}$	$\text{Al}_x\text{Ga}_y\text{In}_{1-x-y}\text{As}$	8	1.10	+0.5(t)	0.265	0.278	
$10 \times \text{QW}$	$\text{Al}_x\text{Ga}_y\text{In}_{1-x-y}\text{As}$	5	1.29 ¹	-0.95(c)	0.170	0.159	
SCH	$\text{Al}_x\text{Ga}_y\text{In}_{1-x-y}\text{As}$	80	1.05	0	0.315	0.157	

Tab. 6.4: Active layers of epitaxial layout I. These replace layers 4 to 26 in Table 6.3. ¹ QW PL includes confinement energy, QCSE of the built-in field and exciton energy.

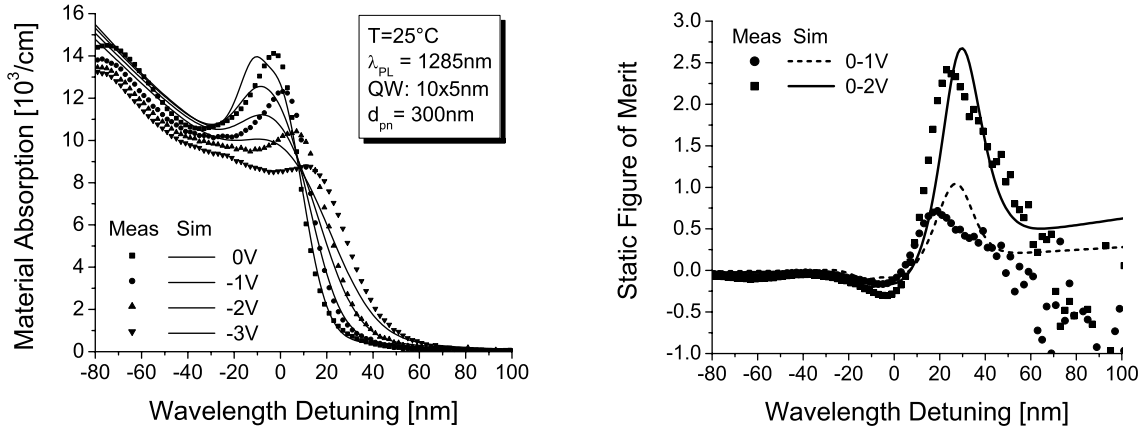


Fig. 6.5: Absorption spectra of layout I, predicted and measured according to Chapter 3 and Section 3.4 for various modulator bias voltages V_{EAM} . The PL wavelength was measured from the absorption device.

Fig. 6.5 shows predicted and experimental absorption spectra along with the corresponding figure of merit. The maximum FoM for -1 V bias and 2 V voltage swing is obtained at a detuning of 30 nm , just slightly above the broad area laser gain maximum. Thus, this epitaxial structure is suitable for both, laser and modulator operation. It features low residual absorption and optimal absorption swing as well as high optical gain at a single operating wavelength. The experimental and simulated BA laser results are given in Table 6.5.

Device	QWs	λ_{PL} [nm]	Threshold J_{th} [kA/cm^2]		Wavelength λ_{BA} [nm]	
			sim	meas	sim	meas
I	$10 \times 5\text{ nm}$	1290	0.83	0.87	1317	1312

Tab. 6.5: Predicted and measured broad area laser characteristics of layout I according to Chapter 4.

6.2.4 Epitaxial Layout II: Double QW Type Structure

The structure listed in Table 6.6 represents another proposal for an active material common for both sections in an integrated EML. The idea behind the incorporation of two different types of QWs is asymmetric behavior between reverse and forward operation expected from the phosphorus system. In this material system, mainly the first few QWs on the p-side of the active material are electrically pumped due to the high valence band contrast and heavy hole masses as indicated by Fig. 2.8. Therefore, two or three QWs with larger PL wavelength dominating laser operation (laser(LD)-QWs) are grown on top of eight to ten modulator wells (EAM-QWs) dominating modulator performance.

Epitaxial Layout II							
Function	Material	Thickness [nm]	Bulk λ_{PL} [μm]	Strain ε_{xx} [%]	x	y	Doping $10^{18}/\text{cm}^3$
SCH	$\text{Al}_x\text{Ga}_y\text{In}_{1-x-y}\text{As}$	30	1.05	0	0.315	0.157	
$4 \times \text{Bar}$	$\text{Al}_x\text{Ga}_y\text{In}_{1-x-y}\text{As}$	8	1.10	+0.5(t)	0.265	0.278	
$3 \times \text{LD-QW}$	$\text{Al}_x\text{Ga}_y\text{In}_{1-x-y}\text{As}$	5	1.29 ¹	−0.95(c)	0.170	0.159	
SCH	$\text{Al}_x\text{Ga}_y\text{In}_{1-x-y}\text{As}$	30	1.05	0	0.315	0.157	
$9 \times \text{Bar}$	$\text{Al}_x\text{Ga}_y\text{In}_{1-x-y}\text{As}$	8	1.10	+0.5(t)	0.265	0.278	
$8 \times \text{EAM-QW}$	$\text{Al}_x\text{Ga}_y\text{In}_{1-x-y}\text{As}$	7.5	1.27 ¹	−0.95(c)	0.215	0.116	
SCH	$\text{Al}_x\text{Ga}_y\text{In}_{1-x-y}\text{As}$	30	1.05	0	0.315	0.157	

Tab. 6.6: Active layers of epitaxial layout II. These replace layers 4 to 26 in Table 6.3. ¹ QW PL includes confinement energy, QCSE of the built-in field and exciton energy.

Unfortunately, the concept loses its benefits in the aluminum system. Its low valence band contrast results in very homogeneous pumping as illustrated in Fig. 4.2. Absorption, gain and PL spectra are simply averaged between the two QW types weighted by their confinement factor. The performance is comparable to a single QW type device with additional complications in the epitaxial process.

According to Fig. 6.6, detuning for the optimum FoM is still at 40 nm in relation to the laser QW PL wavelength. This is an indisputable sign for the dominance of the laser wells with lower bandgap even for reverse operation. Fig. 6.5 shows the absorption characteristic of a single QW type and clearly indicates that the EAM-QWs make no reasonable absorption contribution 60 nm above their own PL wavelength.

For forward bias operation, Table 6.7 indicates that a detuning of 40 nm to the laser QW PL wavelength equals a 30 nm redshift to the BA wavelength of the device and is thus far beyond acceptable wavelength detuning. According to the gain spectra of Fig. 4.7, the modal gain does not exceed 10/cm for this large wavelength detuning even for strong pumping currents of up to 25 mA. This modal gain will not be sufficient to reach a DFB laser threshold gain of 25/cm simulated in Chapter 5. The EAM-QWs simply act as recombination paths, leading to a high amount of gain well below the operating wavelength and strongly increasing the

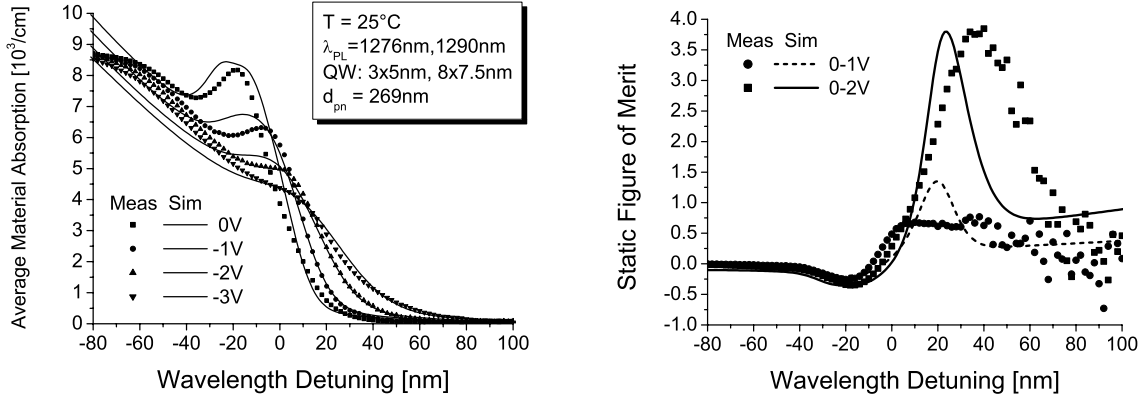


Fig. 6.6: Absorption spectra of layout II, predicted and measured according to Chapter 3 and Section 3.4 for various modulator bias voltages V_{EAM} . The PL wavelength was measured from the absorption device. Wavelength detuning refers to the laser QW PL wavelength.

Device	QWs	λ_{PL} [nm]	Threshold J_{th} [kA/cm ²]		Wavelength λ_{BA} [nm]	
			sim	meas	sim	meas
II	3 × 5 nm, 8 × 7.5 nm	1292	0.95	0.95	1301	1304
		1277				

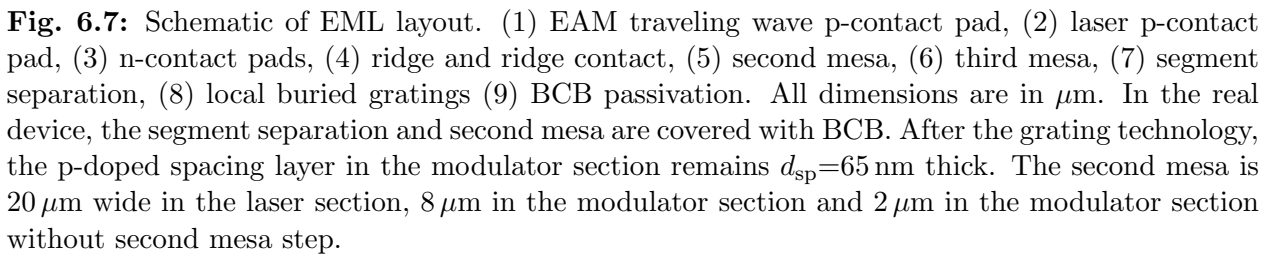
Tab. 6.7: Structure II predicted and measured broad area laser characteristics according to Chapter 4. The BA wavelength is an average between the gain maximum of the three laser (≈ 1315 nm) and the eight modulator (≈ 1300 nm) QWs due to the homogeneous pumping in the aluminum system.

threshold current. Although the maximum FoM is larger for the double QW type structure, there are no benefits of using two QW types within the reasonable range of wavelength detuning of up to 20 nm from the laser QW PL wavelength (or 10 nm to the BA laser wavelength). Note that the absorption edges are much steeper in the single QW type structure I.

6.3 Device Geometry Design

Epitaxial layer structures themselves fulfill no function as they are purely one-dimensional geometries. A waveguide must be defined for lateral optical confinement and metal contacts have to be introduced for driving the EML with electric circuits. In addition, gratings must be defined for lasing action. This is usually done by optical lithography defined wet and dry chemical etching and various material deposition processes. The whole procedure is referred to as device or chip technology and treated in this section.

A typical laser modulator layout is shown in Fig. 6.7. It represents a design with buried gratings and a second mesa step in the modulator. For metal gratings, the chip technology starts immediately after the single epitaxial run. For index gratings, it follows after an initial



The laser section is $380\,\mu\text{m}$ long with a coupling factor of roughly 80/cm for index and 15/cm for metal gratings, respectively. Exact values are given in Table 7.2. The continuous waveguide into the modulator section is equivalent to a zero reflectivity anti-reflection coating of the second laser ‘facet’. According to Chapter 5.1.4, the DFB laser threshold gain

is affected by the HR facet cleaving position and shows a span of $g_{\text{th}} = 23/\text{cm}$ to $28/\text{cm}$ for index and $36/\text{cm}$ to $55/\text{cm}$ for metal gratings, respectively. Note that these values include intrinsic waveguide scattering losses of $\alpha_i = 15/\text{cm}$ and additional metal grating losses of $\alpha_{\text{metal}} = 8/\text{cm}$. The modulator section is $120\ \mu\text{m}$ long.

The following design variations are discussed in the subsequent sections:

- Grating technology: position of index grating layer and lateral gratings
- Substrate material: conducting or semi-insulating (s.i.)
- Modulator waveguide definition: with or without second mesa step

6.3.1 Grating Technology

The fundamental impact of different grating types and coupling strengths on laser threshold current and emission spectrum are discussed in Chapter 5. In contrast, this section deals with the additional technological challenges and trade-offs associated with gratings for integrated laser modulators in the aluminum material system. Here, the gratings have to be applied locally to the laser section only.

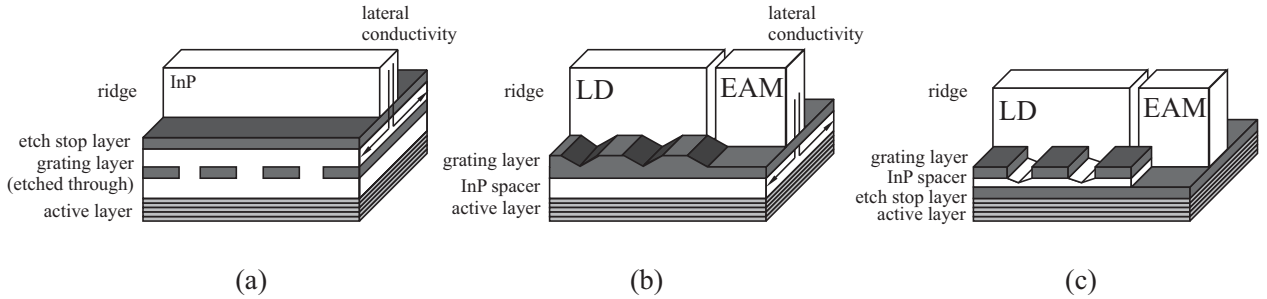


Fig. 6.8: Schematic of various grating designs. (a) standard layout for stand-alone DFB lasers. (b) EML type. (c) improved EML type.

Figure 6.8 illustrates various grating types. In a stand-alone DFB laser as in Fig. 6.8(a), the quaternary grating layers are etched through during the grating definition. The coupling strength is defined by the well controlled epitaxial layer thickness, and the grating shape is almost rectangular. A SEM picture of this grating approach is shown in Fig. 5.1 on page 40. An additional layer on top of the grating acts as an etch stop for the ridge definition. Another approach was chosen in order to reduce the lateral conductivity of the layers between the ridge and the active stack in the modulator since it degrades modulation performance. The approach is illustrated in Fig. 6.8(b). The quaternary index grating layer is thicker than the grating defining etch depth and remains at least $d_{\text{sp}} = 65\ \text{nm}$ thick after the grating definition. The remaining part can be used as an etch stop layer for the ridge process in both sections, rendering an additional stop layer unnecessary. Figure 6.9 provides

an SEM picture of the cross section of the grating.

This trade-off between laser and modulator performance has three main drawbacks. First,

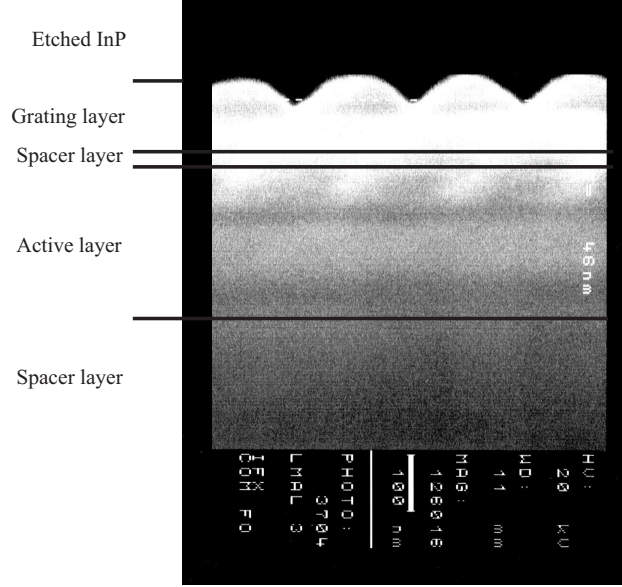


Fig. 6.9: SEM picture of a cleaved grating surface. The overgrown InP layer is etched selectively.

the grating profile is triangular, resulting in a lower coupling coefficient. Second, the grating depth is defined by the etch process, causing fluctuations in coupling strength between different technology runs. Third, although reduced, there is still lateral conductivity in the modulator section.

As threshold current is only of secondary interest for integrated EMLs, metal gratings are an attractive alternative to their index counterparts, rendering the overgrowth process unnecessary and producing a very high single-mode yield [32]. Within this thesis, no special layer structure was designed for lateral metal gratings. The p-doped layers were reduced to a thickness of $d_{sp} = 65$ nm in the laser and modulator sections by an additional dry etch process after the ridge definition. This reduces lateral conductivity and increases the grating coupling coefficient, but imposes a strong tendency towards lateral multi-mode behavior. Metal grating stripes are defined on the quaternary etch stop layer on either side of the ridge by a lift-off process after an electron beam lithography step [38].

Side Note: The alternative layer design proposed in Fig. 6.8(c) includes an etch stop layer *below* the grating layer and an InP spacer. During the local grating process, the grating stripes are etched down to the InP layer in the laser section. Thus, the grating layer is totally removed in the EAM. The overgrowth process is similar to that of a stand-alone DFB laser. During the wet chemical ridge definition, the etch process will stop at the grating layer in the laser section. Despite the gaps in the quaternary material, this happens as soon as the crystal planes are developed in the binary InP. A single-mode laser waveguide is formed.

In the modulator section, the etching will not stop until the second quaternary layer. This proposal features defined gratings as well as low lateral conductivity. Unfortunately, the results of this promising approach are not included in this thesis and will be presented in future work [38, 24].

In the active phosphorus system, the intrinsic SCH layers themselves can act as an etch stop, reducing lateral conductivity to zero.

6.3.2 Substrate Influence

Integrated EMLs can be grown on n-doped or semi-insulating (s.i.) InP substrates. For most applications, conducting n-doped substrate is the first choice due to its superior material quality and the possibility of having a large area n-contact on the back of the wafer. However, large conducting areas are a source of parasitic capacitance. Thus, high-speed applications often use s.i. substrates.

The EAM in Fig. 6.7 features two main capacitors: the intrinsic capacitor of the active region and the parasitic capacitor formed by the contact pads. The intrinsic capacitance is not affected by the substrate type since epitaxially grown n- and p-doped InP forms the electrodes of the capacitor. However, Fig. 6.10 shows that the parasitic capacitance of feed lines and their wave impedance strongly depend on the choice of the substrate. Up to 40 GHz, the microwave wavelength is much longer than the whole device. Thus, it can be regarded as a lumped element. Another approach is the description in terms of wave impedance mismatch that might be more familiar to microwave engineers. Obviously, both models yield similar results.

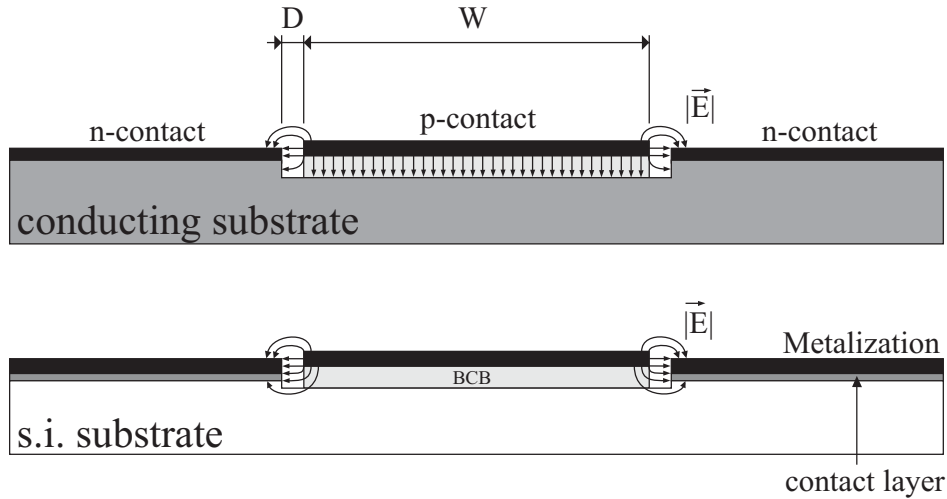


Fig. 6.10: Comparison between feedlines on conducting and s.i. substrates.

Lumped Element Model: In the lumped element model, the pads form an additional capacitor that increases the overall RC time constant. For a conducting substrate, a simple

plate capacitor model is used:

$$C_{\text{pad}} = \varepsilon_0 \varepsilon_{\text{r,BCB}} \frac{A_{\text{pad}}}{d_{\text{BCB}}} = 0.21 \text{ pF} \quad (6.3)$$

C_{pad}	p-pad capacitance
$\varepsilon_{\text{r,BCB}}$	BCB dielectric constant, = 3 [39]
A_{pad}	p-pad area, = $2 \cdot 250 \mu\text{m} \times \frac{70+20}{2} \mu\text{m} + 120 \mu\text{m} \times 10 \mu\text{m}$
d_{BCB}	BCB thickness below p-pad, $\approx 3 \mu\text{m}$

In this equation, the BCB thickness is the main source of uncertainty due to the inhomogeneous planarization process.

For a s.i. substrates, the capacitance can be approximated using a conformal mapping technique [40]:

$$\varepsilon_{\text{eff}} = \frac{\varepsilon_{\text{r,BCB}} + 1}{2} = 2 \quad (6.4)$$

$$C_{\text{pad}} = 4 \varepsilon_0 \varepsilon_{\text{eff}} \frac{\pi l_{\text{pad}}}{\ln \left(2 \frac{1 + \sqrt[4]{1 - (W/(W+2D))^2}}{1 - \sqrt[4]{1 - (W/(W+2D))^2}} \right)} + 11 \text{ fF} = 0.05 \text{ pF} \quad (6.5)$$

ε_{eff}	microwave effective permittivity
l_{pad}	pad length, = $2 \cdot 250 \mu\text{m}$
W	central stripe width, = $70 \mu\text{m}$ in this thesis
D	coplanar stripe spacing, = $35 \mu\text{m}$ in this thesis

The 11 fF in equation (6.5) refer to the ridge contact stripe capacitance. Note that the actual capacitance is higher due to the finite extension of the contact metalizations and the presence of a high-permittivity semiconductor. The incorporation of a semi-insulating substrate reduces the parasitic capacitance by a factor of four.

Microwave Model: Although shorter than the material microwave wavelength, the contacts can also be regarded as waveguides. In this model, an impedance mismatch with the 50Ω driver resistance results in reflections and performance degradation at high frequencies. For (quasi-)TEM lines, the characteristic impedance is calculated by the capacitance and inductance per length unit, C' and L' , respectively. Both parameters enter the phase velocity term $v_{\text{ph}} = (L'C')^{-0.5} = c_0/\sqrt{\varepsilon_{\text{eff}}}$. Therefore, knowledge of one of the parameters, usually C' will be sufficient if the waveguide effective permittivity is known. For a certain frequency

range, C' is determined by static calculations according to equations (6.3) or (6.5).

For a conducting substrate, the feed line is a microstrip line. For high frequencies, its effective permittivity is mainly determined by the highest dielectric permittivity between the conductors ($\varepsilon_{\text{eff}} = \varepsilon_{\text{r,BCB}}$). This is equivalent to the attraction of an optical wave by the highly refractive fiber core material.

$$C' = 4 \frac{\text{pF}}{\text{cm}} \quad (6.6)$$

$$Z = \sqrt{\frac{L'}{C'}} = \frac{\sqrt{\varepsilon_{\text{r,BCB}}}}{c_0 C'} = 15 \Omega \quad (6.7)$$

C'	microwave capacitance per unit length
L'	microwave inductance per unit length, here = 0.9 nH/cm
Z	microwave characteristic wave impedance

More detailed calculations result in 20 to 30 Ω over a wide frequency range [41].

On a s.i. substrate, the feed line is almost a coplanar waveguide. For the approximation of thin metalizations, its effective permittivity is given by equation (6.4) and remains constant for all frequencies:

$$C' = 1 \frac{\text{pF}}{\text{cm}} \quad (6.8)$$

$$Z = \sqrt{\frac{L'}{C'}} = \frac{\sqrt{\varepsilon_{\text{eff}}}}{c_0 C'} = 47 \Omega \quad (6.9)$$

Obviously, the semi-insulating substrate shows much better impedance matching. Thus, less microwave power is reflected back to the source.

In Section 9, both types of substrate are included in an equivalent circuit model, pointing out that a s.i. substrate is beneficial beyond 10 GHz modulation frequency for the investigated contact layout.

6.3.3 Modulator Section with and without Second Mesa Step

As mentioned before, lateral conductivity in the modulator second mesa p-region causes a constraint of modulation behavior. Fig. 6.11 points out that for high lateral conductivity the

effective intrinsic capacitance is increased by a factor of up to three due to the larger active area, leading to a decrease in bandwidth by the same factor. The effect will be weakened if lateral conductivity in the p-region is reduced, by reducing either its dopant concentration or its layer thickness. If lateral conductivity cannot be avoided, devices etched through the active area without a second mesa step can overcome the problem.

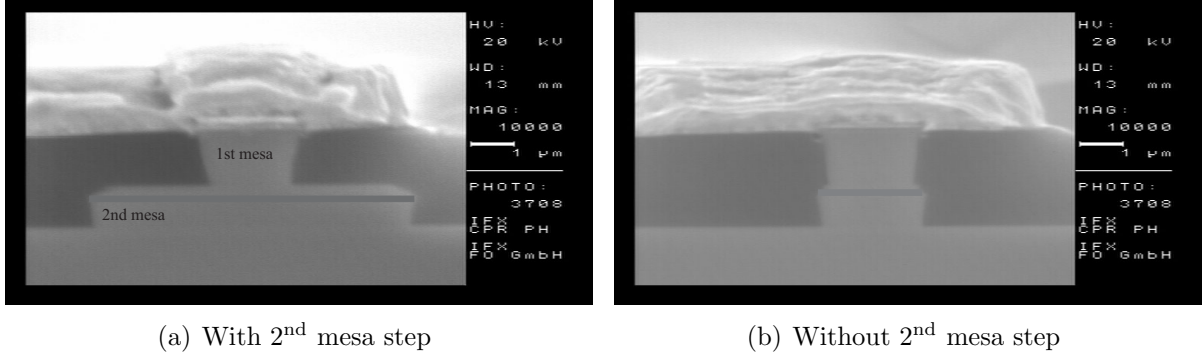


Fig. 6.11: SEM pictures of modulator facets. The intrinsic active area is highlighted. If the upper p-region is highly conductive, the capacitance of design (a) will be three times larger than that of design (b).

On the other hand, the etched trough modulator is no longer a single-mode waveguide because of the strong lateral confinement of semiconductor to BCB. Furthermore, the optical field has a significant overlap with the sidewalls, increasing scattering effects. For this particular design, the dry etching process must be well controlled for a homogeneous vertical profile through the different layers (InP, ternary, Al-quaternary) with smooth surfaces and low surface leakage currents.

6.3.4 Device Geometry Layouts A, B, C and D

Table 6.8 summarizes the four different geometry layouts that are proposed within this thesis, featuring various combinations of the above design variations.

	Device A	Device B	Device C	Device D
Grating type	index	metal	index	index
Substrate	s.i.	n	s.i.	n
EAM 2nd mesa step	no	no	no	yes

Tab. 6.8: Device geometry layouts.

The results for static, dynamic and thermal performance of the four EML devices will be discussed in the following three chapters.

Chapter 7

Static Device Performance

	Device A	Device B	Device C	Device D
Epitaxial structure	Layout I	Layout I	Layout II	Layout II
QWs	10×5 nm	10×5 nm	3×5, 8×7.5 nm	3×5, 8×7.5 nm
Operating wavelength	1309 nm	1314 nm ⁽¹⁾	1305 nm	1305 nm
Detuning	30 nm	25 nm	25 nm ⁽²⁾	15 nm ⁽²⁾
Modulator length	120 μm	120 μm	120 μm	120 μm
Grating type	index	metal	index	index
Substrate	s.i.	n	s.i.	n
EAM 2nd mesa	2 μm	2 μm	2 μm	8 μm
Simulation:				
Residual absorption	4.5 dB	7.6 dB	4.2 dB	10.3 dB
Extinction ratio $V_{pp} = 2$ V	15.0 dB	17.8 dB	12.3 dB	17.9 dB
Bandwidth, $V_{EAM} = -2$ V	38 GHz	27 GHz	38 GHz	19 GHz
Experiment:				
Residual absorption ⁽⁴⁾	3.1 dB	8.5 dB	2.8 dB	7.9 dB
Extinction ratio $V_{pp}=2$ V	12.4 dB	13.9 dB	9.3 dB	19.8 dB
Bandwidth, $V_{EAM} = -2$ V ⁽³⁾	35 GHz	20 GHz	39 GHz	20 GHz
Fiber coupled power	425 μW	494 μW	409 μW	568 μW
Threshold current	30 mA	32 mA	31 mA	21 mA
SMSR	45 dB	30 dB ⁽¹⁾	10 dB	12 dB
CPR nomenclature	M7-23-12-04	M8b-15-16	M6II-18-20-01	M4-16-08-03

Tab. 7.1: Devices under test. All experimental data are for $I_{LD}=60$ mA laser current and 15°C heat sink temperature. Fiber coupled power is measured at $V_{EAM} = 0$ V modulator bias with a fiber coupling efficiency of 40%. ⁽¹⁾ Device B features two lateral modes. ⁽²⁾ Detuning to laser well PL wavelength. ⁽³⁾ Measured by [24] and [38]. ⁽⁴⁾ Extracted from modulator currents, $\approx \Delta I_{EAM}(0 - 2 \text{ V})/\max(I_{EAM})$.

This chapter compares the static performance of four chosen components realized according to the design rules of the previous chapter. Experimental data of fiber coupled optical power and modulator current with variable laser current as well as optical spectra are chosen to represent the static behavior. Table 7.1 summarizes the main technological characteristics

of all four devices under test along with selected measurement results.

The simulation results are in good agreement with experimental data. For three out of four devices, measured residual absorption is 1.5 dB to 2 dB lower than predicted by theory. In the same way, the extinction ratio of three out of four devices is 2.5 dB to 4 dB lower in the experiment than in the simulation. This error of approximately -25% is attributed to the uncertainty of the normalization factor used in the Fit Algorithm to calibrate the absorption simulation.

Concerning the 3 dB modulation bandwidth, simulated and experimental data are in very good agreement. Except for device B the error is less than 8%. For this device, the predicted bandwidth exceeds the experimental result by more than 35%. Obviously, the parasitic capacitance of the conducting substrate is higher than predicted in Section 6.3.2 which is most likely due to a thinner BCB passivation layer.

As pointed out in Section 6.2.4, theoretically there is no benefit from including double QW types in shared active area EMLs employing AlGaInAs as active material. This is proved by focusing on devices A and C, comparing epitaxial layouts I and II with single and double QW types, respectively. Both have similar detuning that is large enough to allow for excellent modulation bandwidths. The predicted figures for residual absorption (4.5 dB and 4.2 dB), extinction ratio (15.0 dB and 12.3 dB) and bandwidth (38 GHz for both) are almost equal. The experimental performance of the structures in terms of fiber coupled power (425 μ W and 409 μ W), extinction ratio (12.4 dB and 9.3 dB), bandwidth (35 GHz and 39 GHz), threshold current (30 mA and 31 mA) and residual absorption (3.1 dB and 2.8 dB) is comparable. This confirms the prediction that, due to homogeneous pumping in the aluminum system, there is no principle advantage of double QW types. Their individual contributions are simply averaged in absorption, gain and chirp.

According to Section 6.2, wavelength detuning is one of the most essential parameters for integrated shared active area EMLs. To ascertain this proposal, the static design of devices C and D is equal except for increased detuning of device D. Their comparison proves that this increased detuning results in lower residual absorption (2.8 dB opposed to 7.9 dB), lower extinction ratio (9.3 dB and 19.8 dB) between zero and minus two volts and higher threshold current (31 mA and 21 mA) as predicted by theory, photocurrent absorption and Fabry-Perot gain experiments. This is consistent with the design rules illustrated in Fig. 6.3, pointing out that for a larger wavelength detuning the EAM bias voltage has to be increased in order to achieve an equal figure of merit, and the laser threshold current rises.

Concerning the two types of gratings, device B incorporating metal gratings is similar to its index counterpart A. The only drawback is lower bandwidth due to the conducting substrate. Unfortunately, the structure showed two lateral modes. Section 7.3 will provide a detailed discussion of this behavior.

Finally, high cut-off frequencies of 35 GHz and 39 GHz are only achieved by devices A and C grown on a semi-insulating substrates and featuring etched through EAM sections. Devices

B and D show worse dynamic performance with bandwidths of only 20 GHz due to the combination of $8\mu\text{m}$ second mesa and a conducting substrate.

Unfortunately, optical output powers are rather low. For the low bandwidth designs B and D, this obviously arises from high residual absorption. Equation (7.1) is a brief estimation of the expected fiber coupled optical power of an EML.

$$P_{\text{out}} = \eta_f \eta_d (I_{\text{LD}} - I_{\text{th}}) 10^{-\alpha_{\text{res}}/10} \quad (7.1)$$

Assuming a laser slope efficiency of $\eta_d = 0.3\text{ W/A}$ and a fiber coupling efficiency of $\eta_f = 35\%$ [24], $P_{\text{out,B}} = 400\mu\text{W}$ and $P_{\text{out,D}} = 630\mu\text{W}$ fiber coupled power are expected under $\alpha_{\text{res,B}} = 8.5\text{ dB}$ and $\alpha_{\text{res,D}} = 7.9\text{ dB}$ optical attenuation in the EAM, pumping $I_{\text{LD}} - I_{\text{th}} = 28\text{ mA}$ and 39 mA above the laser threshold current for devices B and D, respectively. This is close to the experimental figures of $P_{\text{out,B}} = 494\mu\text{W}$ and $P_{\text{out,D}} = 568\mu\text{W}$ fiber coupled power, respectively.

For the etched through modulator ridges, the power loss cannot be explained by residual absorption as the modulator currents are rather low. It is attributed to optical scattering and excitation of higher order modes.

7.1 Effective Index of Laser Modulator Waveguides

To determine the grating period and to obtain the desired DFB output wavelength, the effective index of the ridge waveguide laser structure must be known. As it is only accessible to measurement after DFB device fabrication, it is very convenient to have a simulation tool that is able to predict a good initial guess for the effective index prior to the technological run. This section compares the initial effective index prediction that was used to calculate the DFB grating period and the final experimental result.

Simulation makes use of the effective index method explained in Section 5.1.2. The material input data are provided in Table G.6 on page 139. They include the refractive indices for the layers interpolated by the Adachi method given by equation (A.7) on page 106. They are higher than material indices obtained from other interpolation methods but yield excellent results in predicting waveguides properties. Note that charge densities resulting from doping or pumping are not included and actually lower the refractive index, see Chapter A.1. QW indices cannot be calculated by the bulk semiconductor Adachi method as the operating wavelength lies below the bandgap wavelength. Instead, the Kramers-Kronig relationship presented in Chapter 3.5 has to be used on the QW gain spectrum.

Effective indices are measured by the emission wavelength λ_{DFB} and grating period Λ of a DFB laser according to equation 7.2 [10].

$$\lambda_{\text{DFB}} = 2 \Lambda n_{\text{eff}} \quad (7.2)$$

Coupling coefficients are extracted from the wavelength separation between the two dominating modes on either side of the Bragg wavelength of devices with low SMSR. For these devices, the separation becomes maximal and is equivalent to the stop band width $\Delta\lambda_{\text{Stop}}$ [30]:

$$\Delta\lambda_{\text{Stop}} = \frac{\lambda_{\text{DFB}}^2}{2n_{\text{eff}}} \left(\frac{1}{l_{\text{LD}}} + \frac{\kappa}{2} \right) \quad (7.3)$$

Peak separations smaller than the stop band width may occur for devices with high SMSR due to cleaving related statistics. Such spectra cannot be used to extract the coupling coefficient.

Device	Device A	Device B	Device C	Device D	std DFB	std DFB
Wavelength	1309 nm	1314 nm 1323 nm	1305 nm	1305 nm	1310 nm	1490 nm
Epitaxial structure	I	I	II	II		
Grating	index	metal	index	index	index	index
Simulation:						
n_{eff}	3.290	3.291 3.270	3.282	3.285	3.242	3.225
Γ	12%	12%	17%	17%		
Γ_{Grat}	6.2%	$1.5 \cdot 10^{-4}$	6.9%	3.1%		
κ	72/cm	113/cm	80/cm	36/cm	70/cm	50/cm
Measurement:						
Grating period	199.1 nm	201.0 nm	199.6 nm	198.6 nm	201.2 nm	231.0 nm
n_{eff}	3.289	3.291 3.271	3.269	3.285	3.240	3.225
κ				35/cm	60/cm	

Tab. 7.2: Waveguide properties of different investigated devices. Note that device B features two lateral modes as predicted by calculations and verified by emission spectra and far field pattern measurements. Average values for standard DFB lasers are obtained from 1000 devices. For device D, the grating etch depth is only 45 nm. Calculated and measured spectra for devices B and D are shown in Fig. 5.6.

Simulation and experimental data are summarized in Table 7.2. The agreement is excellent: except for device C, the error of the effective index is below 0.1%. Even the two lateral modes of device B were predicted with an error below 0.1%. Detailed explanation on this

topic is given in section 7.3. Additionally, the table includes the experimental and simulated data of standard stand-alone DFB lasers validating the excellent performance of the simulation approach for a diversity of devices. The effective index method in conjunction with the Adachi indices is a very reliable simulation approach that is well-suited for the ridge waveguide device design without any experimental fitting.

In the subsequent subsections, the experimental graphs are provided from which the static key figures are summarized in Tables 7.1 and 7.2. The dynamic modulation bandwidths will be provided in Chapter 9.

7.2 Device A

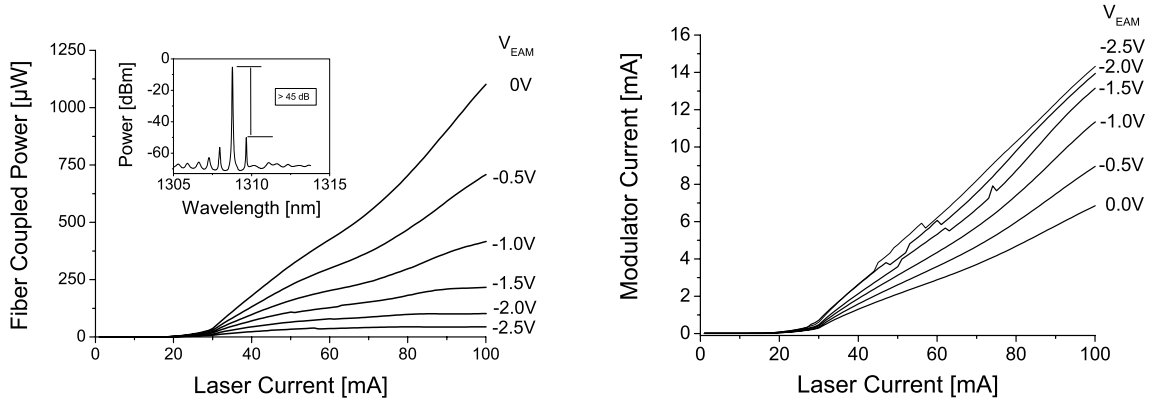


Fig. 7.1: Static experimental results of device A.

For this design, Fig. 7.1 shows a rather high maximum output power and a good extinction ratio between $V_{\text{EAM}} = -0.5\text{ V}$ and -2.5 V modulator bias. The large difference between the modulator currents corresponding to $V_{\text{EAM}} = 0\text{ V}$ and -2 V implies low residual absorption of only 3 dB.

7.3 Device B

The nonlinearity of the PI characteristics of device B in Fig. 7.2 and the double threshold current behavior indicates a modal defect. The spectrum shows that, like all metal grating lasers, device B features one longitudinal mode and switches between two competing *lateral* modes. The modulator current characteristic is typical for a high residual absorption device, with only a slight increase of roughly 15% in modulator current between minimal and maximal absorption. Around 85% of the optical power is lost for the case of ON-state bias $V_{\text{EAM}} = 0\text{ V}$.

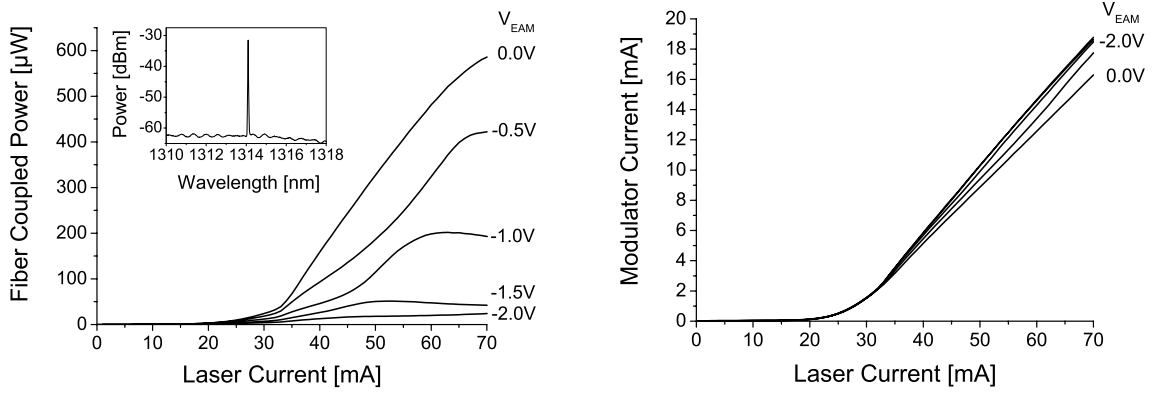


Fig. 7.2: Static experimental results of device B.

A main drawback of metal gratings is a strong tendency toward lateral multi-mode behavior. This is due to the fact that the first order mode has a much higher overlap with the grating placed adjacent to the ridge ($\Gamma_{\text{Grat,1st}} > \Gamma_{\text{Grat,fund}}$) and is therefore subject to much stronger coupling than the fundamental mode according to equation (5.11).

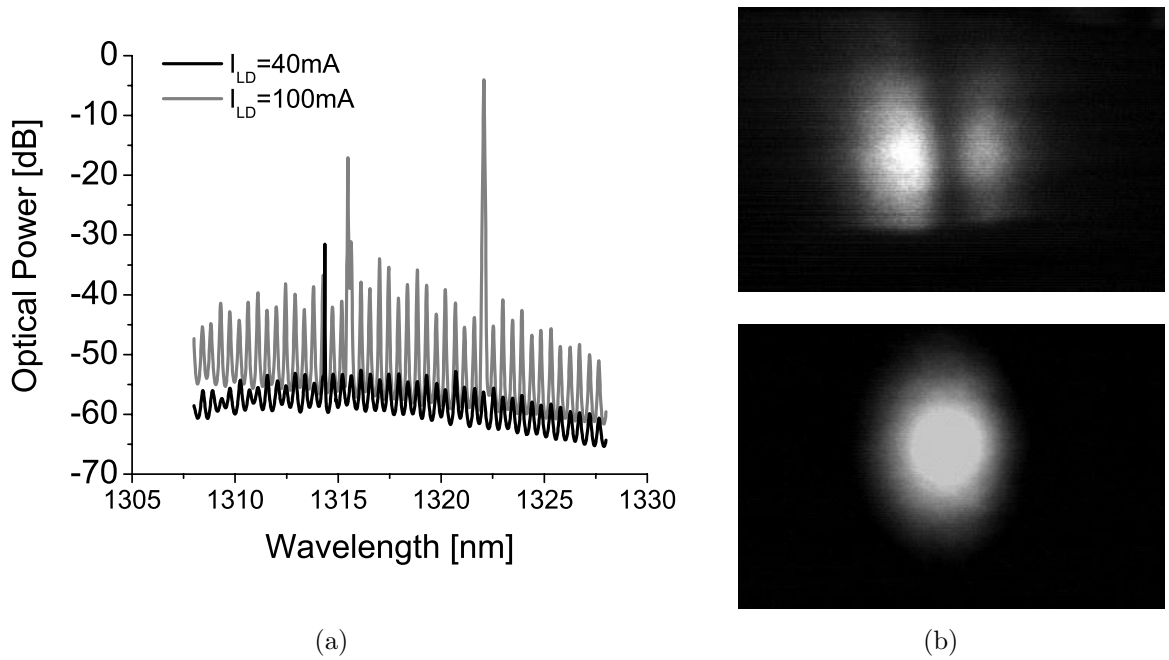


Fig. 7.3: Experimental lateral multi-mode behavior of metal coupled DFB lasers. (a) Optical spectra for low and high excitation, (b) far fields of DFB laser for low excitation (top) and Fabry-Perot laser with identical waveguide (bottom) [38].

Figure 7.3 indicates that the device starts lasing in its first order mode with lower emission wavelength, lower effective index and two far field lobes. Due to spatial hole burning occurring at high pumping currents, the carrier density diminishes adjacent to the ridge and the

fundamental mode becomes dominant. Compared to index coupled DFB lasers, the design margins of metal grating lasers for lateral single-mode operation are much tighter. It can be guaranteed by employing high index contrast or narrow ridge widths. A Fabry-Perot laser with identical waveguide showed a Gaussian far field pattern for all pumping currents. In this case, the fundamental lateral mode is preferred due to its strong overlap with the spatial carrier injection profile.

7.4 Device C

Device C shows a defined threshold current and the typical enhanced thermal roll-over induced by modulator self-heating as illustrated in Fig. 7.4. Due to the large detuning, the

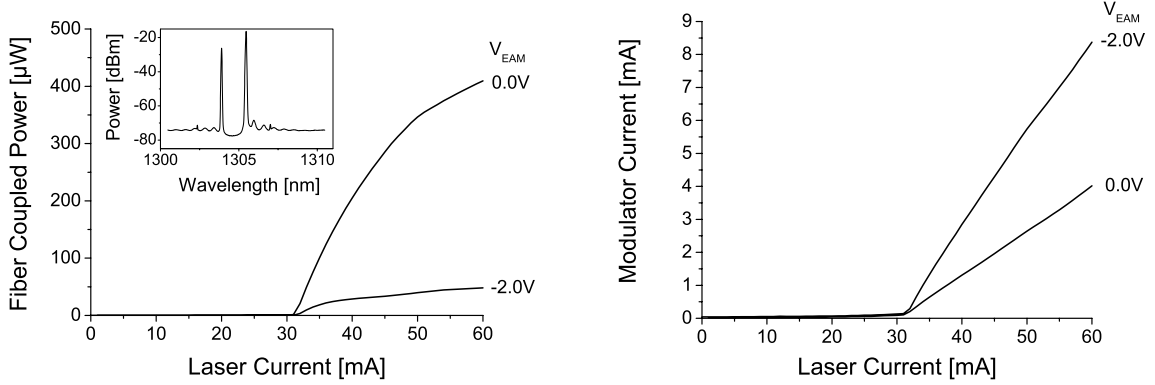


Fig. 7.4: Static experimental results of device C.

extinction ratio is limited and the threshold current is rather high. Similar to device A, the modulator currents indicate very low residual absorption. Unfortunately, the output power of the component is in the same order of magnitude as for the other designs. This is attributed to roughness scattering at the etched sidewalls of the ridge. Due to its low absorption and optimized microwave design, the device showed the fastest modulation speed of all investigated laser modulators.

7.5 Device D

Device D was part of the initial steps of design process. Its static performance is shown in Fig. 7.5. Incorporating a standard ridge waveguide including a second mesa step in both laser and modulator sections, it shows undisturbed static characteristics but severe limitations in modulation bandwidth. The small detuning causes high residual absorption, high extinction ratio and low threshold current.

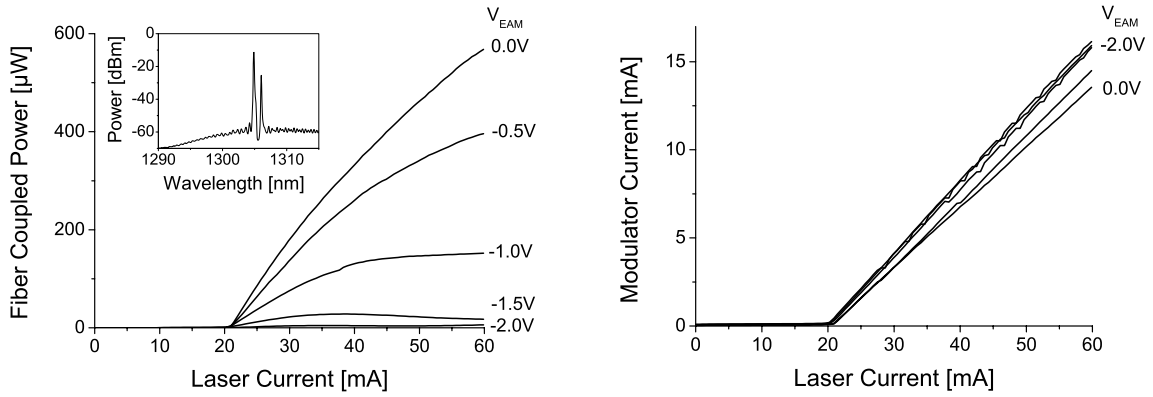


Fig. 7.5: Static experimental results of device D.

7.6 On-Wafer Testing

On-wafer testing is a promising possibility to test integrated laser modulators. It enables preliminary screening of devices prior to cleaving, coating and mounting and can easily be done automatically. Without major effort, all devices on a wafer can be screened. Up to now, only VCSELs have allowed for this sort of measurement.

As the active area can also be used as a waveguide detector, an alignment of the devices on the wafer with two modulator sections facing each other or an integrated amplifier enables on-wafer testing. The setup is outlined in Fig.7.6. The laser section is driven in forward

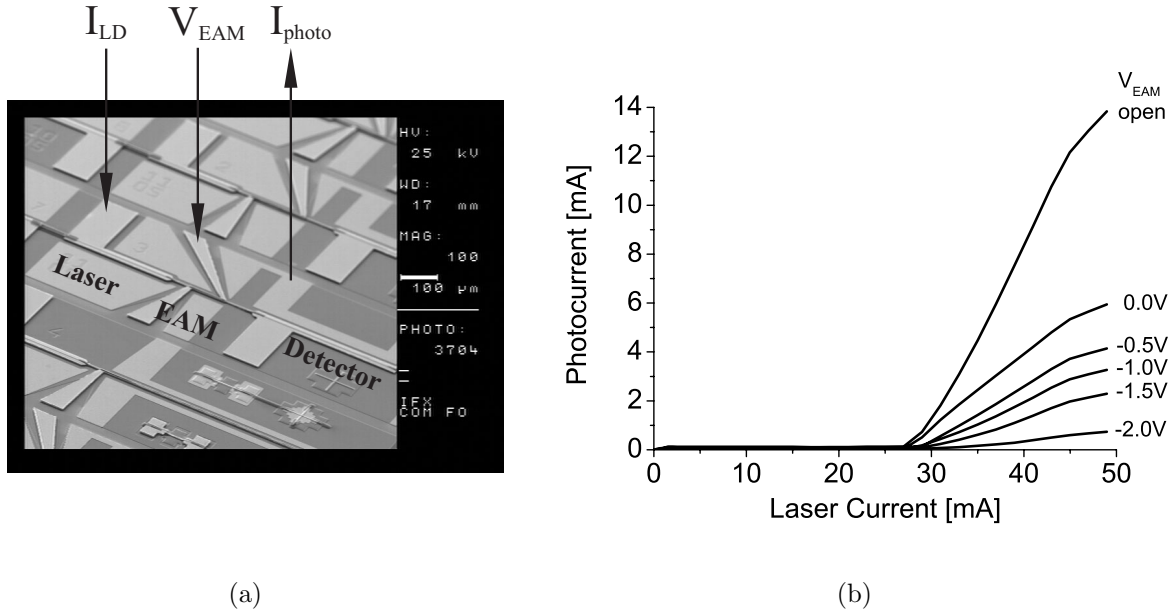


Fig. 7.6: On-Wafer testing. (a) Test setup with an integrated amplifier as a detector. (b) Experimental photocurrent results of device D.

direction. It starts lasing due to its DFB grating resonator. The EAM section is used to modulate the light intensity. Finally, either the modulator of the adjacent device or an integrated amplifier acts as a photodetector under strong reverse bias. All other sections along the ridge are used as absorbers to avoid multiple reflections. Thus, the light never leaves the ridge waveguide. With two microwave optimized EAMs facing each other, it is even possible to measure the small and large signal dynamic performance on wafer level. Although this procedure enables an early check of device characteristics, it has some serious drawbacks:

- Very high extinction ratios cannot be measured precisely. For example, the photocurrents in the detector for a total modulator absorption of 30 dB are in the range of a few microampere. This is well below the electrical crosstalk of 0.1 mA originating from $V_{\text{EAM}} = -2 \text{ V}$ modulator bias voltage over a $20 \text{ k}\Omega$ separation resistance.
- The laser is examined under non-ideal conditions due to two perfectly anti-reflecting facets. It will change its emission spectrum, threshold current and slope efficiency randomly once the high-reflection facet is cleaved. By experience, the threshold current will be reduced roughly by a factor of 1.5.
- As no light leaves the structure, the spectral behavior and emission wavelength remain unknown. On-wafer, lasers with two perfect anti-reflection coatings will feature their intrinsic modal behavior with two and one longitudinal modes for index or metal coupled gratings, respectively.
- To avoid any saturable absorbers, there is no segment separation between two lasers aligned back to back on one ridge. The effective laser length for on-wafer testing is up to twice as long as for isolated devices.
- It is not possible to distinguish between a malfunction of the light emitter and the detector.

Thus, on-wafer testing can only be a rough estimation of the quality of a wafer or a means of monitoring technological stability during the EML production process. It cannot replace characterization of the final mounted device.

Chapter 8

Thermal Properties

In contrast to hybrid laser modulator solutions, the different sections of an integrated device cannot be considered independently of each other in general. Due to the strong optical coupling between laser and EAM, reflections from the EAM can cause optical feedback. The electrical separation of the sections is usually produced by ion implantation [9], etched trenches [32] or local zinc diffusion [33], but insufficient longitudinal resistances may lead to electrical crosstalk. Finally, the spatial proximity of the sections can result in thermal crosstalk [42], meaning a temperature change in one section caused by the heat generation in an adjacent section. All these effects may drastically reduce the static and dynamic performance compared to decoupled devices, leading to threshold changes, increased roll-over, mode jumping or wavelength shifts. While electrical and optical crosstalk are eliminated by high separation resistances and improved anti-reflection measures, respectively, the thermal influence is inevitable in integrated laser modulators.

This chapter starts with the fundamental equations of self-heating of lasers and modulators in Section 8.1. An often underestimated fact is that photo carriers can create heat energy which can be a multiple of the absorbed photon energy. Once the thermal properties of the individual sections are known, the heat generation terms are introduced into a three-dimensional model. Using this simulation, the thermal crosstalk between the device stages is discussed in Section 8.2. Thermal scattering parameters are defined to simplify the further procedure. They enter an ordinary laser model to explain experimental phenomena like modulator bias induced wavelength shift (8.3.2) or increased thermal roll-over (8.3.3).

8.1 Heat Generation in Modulator and Laser

Figure 8.1 illustrates the physical heating mechanism in an EAM. An electron hole pair is created by the absorption of a photon of energy $\hbar\omega$ equal to the bandgap energy. During the escape process, electron and hole travel along the band edges and lose an amount of energy to scattering processes that is equivalent to the sum of initial photon energy and the energy corresponding to the applied bias voltage.

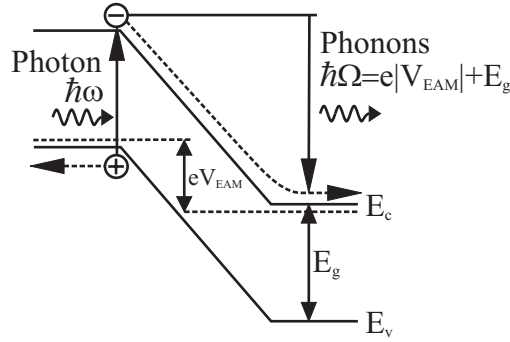


Fig. 8.1: Schematic of the heating process in an EAM.

For a typical bias point of $V_{\text{EAM}} = -2 \text{ V}$, three times more heat is generated than optical power is absorbed. The excess energy is supplied by the generator maintaining the reverse voltage. The heat generation term in the modulator's intrinsic region is written as

$$q_{\text{EAM}}(x) = \frac{1}{d_{\text{pn}}} \left(|V_{\text{EAM}}| + \frac{\hbar\omega}{e} \right) J_{\text{EAM}}(x) \quad (8.1)$$

q_{EAM}	heat source, $\approx 10^9 \text{ W/cm}^3$ at EAM input
V_{EAM}	EAM bias voltage, typically -2 V
d_{pn}	intrinsic region thickness, $\approx 300 \text{ nm}$ in this thesis
J_{EAM}	EAM current density, $\approx 10 \text{ kA/cm}^2$ at EAM input

Typical values are valid for laser operation at a bias point of 40 mA above the threshold current and high residual absorption. The exponential decay of guided mode power indicates that the predominant part of temperature rise takes place in the initial $20 \mu\text{m}$ section of the modulator. In this region, the temperature rise can be up to ten times higher than in the laser section itself. There, the heat generation is described by

$$q_{\text{LD}} = \frac{1}{d_{\text{pn}}} \left(V_{\text{LD}} J_{\text{LD}} - \frac{P_{\text{LD}}}{w l_{\text{LD}}} \right) \quad (8.2)$$

q_{LD}	heat source in the laser active region, $\approx 10^8 \text{ W/cm}^3$
V_{LD}	laser bias voltage, typically 1.5 V
J_{LD}	laser current density, $\approx 4 \text{ kA/cm}^2$
P_{LD}	laser output power, typically 12 mW
l_{LD}	laser length, $= 380 \mu\text{m}$ in this thesis
w	effective width of the active region, $\approx 4 \mu\text{m}$ in this thesis

Equation 8.2 is a simple expression of energy conservation between injected and radiated power.

8.2 Thermal Crosstalk

The thermal crosstalk phenomenon was simulated by a 3D finite element method (FEM) using the commercial software FEMLAB. The modeled cross-section of the InP substrate was $130\text{ }\mu\text{m}$ thick and $100\text{ }\mu\text{m}$ wide. The underlying differential equation is the standard heat transport equation [43]:

$$-\nabla(k\nabla T) = q_i \quad (8.3)$$

k	thermal conductivity of InP, $= 68\text{ W/(Km)}$ [44]
T	temperature

with $i \in [\text{LD}, \text{EAM}]$ for the laser and modulator sections, respectively. The dissipated power densities q are given by equations (8.1) and (8.2). The current density in the laser is assumed to be constant while the current density in the EAM section reduces exponentially with optical power:

$$J_{\text{EAM}}(x) = \frac{e}{\hbar\omega} \frac{1}{w} \tilde{\alpha} P_{\text{LD}} e^{-\tilde{\alpha}x} \quad (8.4)$$

$\tilde{\alpha}$	modal power absorption coefficient in modulator, $\approx 300/\text{cm}$ for -2 V for device D
------------------	---

For the sake of simplicity, all light generated in the laser is assumed to couple into the EAM. In order to separate self-heating and thermal crosstalk effects, two different simulations with only one heat source q_i active at one time are shown in Fig. 8.2.

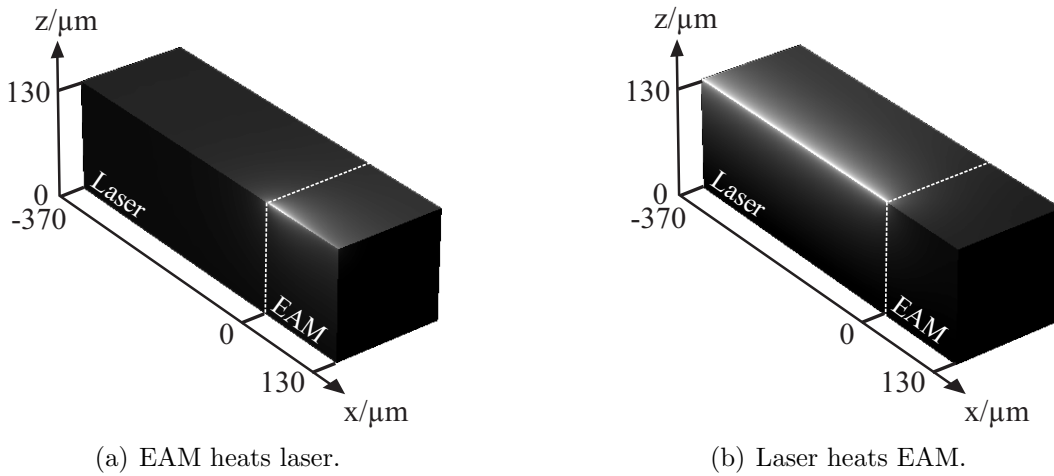


Fig. 8.2: Simulated temperature rise along a vertical cross-section along the symmetry axis of the ridge and on the substrate surface. Only one heat source q_{EAM} (a) or q_{LD} (b) is active at one time.

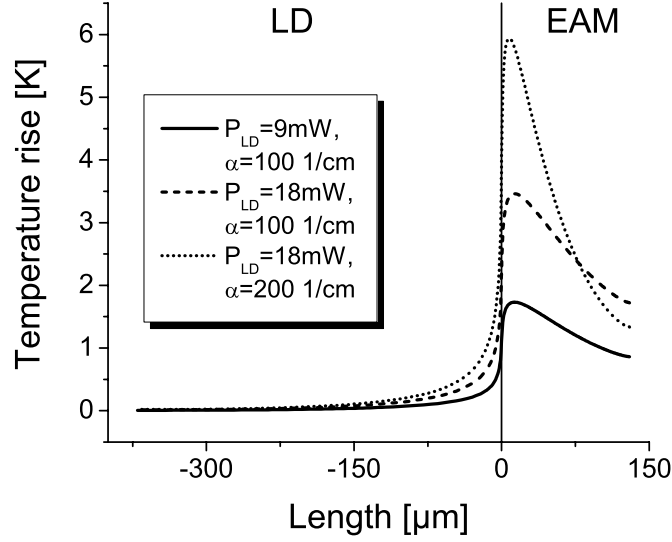


Fig. 8.3: Temperature rise along the DFB-EAM axis by EAM heating.

Fig. 8.3 shows the temperature along the active area with the modulator as the heat source. Higher optical input and higher absorption increase the temperature profile. For both cases illustrated in Fig. 8.2, the average temperature rise in the heating section as well as the average temperature rise in the passive section due to heat transfer were monitored. Thermal ‘scattering parameters’ were defined to link the self-heating and thermal crosstalk to the heat source expressions of the laser and modulator sections:

$$\begin{pmatrix} \Delta \bar{T}_{LD} \\ \Delta \bar{T}_{EAM} \end{pmatrix} = \begin{pmatrix} s_{11}^{th} & s_{12}^{th}(\tilde{\alpha}) \\ s_{21}^{th} & s_{22}^{th}(\tilde{\alpha}) \end{pmatrix} \begin{pmatrix} I_{LD} V_{LD} - P_{LD} \\ \left(\frac{eV_{EAM}}{\hbar\omega} + 1 \right) \tilde{\alpha} P_{LD} \end{pmatrix} \quad (8.5)$$

$$s_{11}^{th} = 84 \text{ K/W} \quad (8.6)$$

$$s_{21}^{th} = 13 \text{ K/W} \quad (8.7)$$

$$s_{22}^{th} = \left(0.325 + 2.01 \cdot e^{-\tilde{\alpha} \cdot \text{cm}/139} \right) \frac{\text{K cm}}{\text{W}} \quad (8.8)$$

$$s_{12}^{th} = \frac{s_{22}^{th}}{7.75 + 14.75 \cdot e^{-\tilde{\alpha} \cdot \text{cm}/288}} \quad (8.9)$$

$\Delta \bar{T}_i$	average temperature rise in a section
s_{11}^{th}, s_{22}^{th}	self-heating coefficient of laser diode and modulator
s_{21}^{th}, s_{12}^{th}	thermal crosstalk between laser and modulator; modulator and laser

After deriving the thermal scattering matrix from 3D simulations, the result was used in conjunction with an ordinary laser model [2, 1]

$$P_{LD} = \eta_d (I_{LD} - I_{th}) \quad (8.10)$$

$$V_{LD} = R_{LD} I_{LD} + V_0 \quad (8.11)$$

to simulate variations in DFB wavelength and output power. Both quantities are easily accessed by experiments. Parameters for the characteristic equations are the threshold current $I_{th} = 18 \text{ mA}$, the differential quantum efficiency at the intersection between laser and modulator $\eta_d = 0.4 \text{ W/A}$, the diode turn-on voltage $V_0 = 0.95 \text{ V}$ and the laser series resistance $R_{LD} = 8 \Omega$ taken from measurement data of the integrated device. The voltage dependent absorption coefficient is derived in Chapter 3. The thermal wavelength shift is $\Delta\lambda_{DFB}/\Delta T = 0.1 \text{ nm/K}$ [44].

8.3 Measurement Results

8.3.1 Temperature Dependent Absorption Characteristics

Before looking at the complex interactions within the final elements, the temperature dependent absorption characteristics must be defined. By empiric investigations, a bandgap shrinkage equivalent to $+0.5 \text{ nm/K}$ band edge shift at 1310 nm emission wavelength and room temperature was found by Varshni, see equation (A.5) on page 105. This shift of the band edge can further be accompanied by an excitonic broadening as enhanced thermal escape processes lower the exciton lifetime. Figure 8.4 shows experimental and simulated temperature dependent absorption spectra.

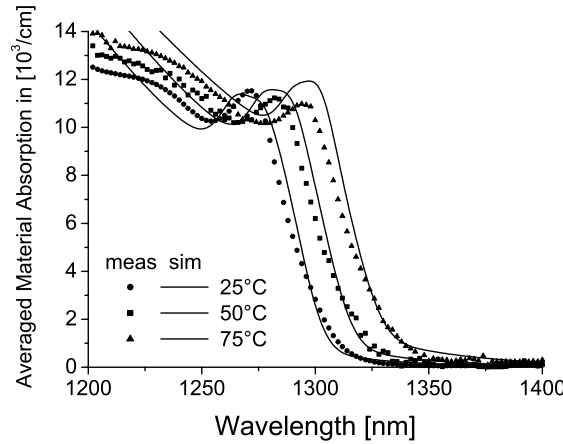


Fig. 8.4: Simulated and experimental absorption spectra of epitaxial layout II for $V_{EAM}=0 \text{ V}$ bias and various heat sink temperatures.

Obviously, the slope of the band edge stays almost constant within a 50°C temperature range. Explanation is provided by the high conduction band contrast of the AlGaInAs system that

is well-known for its thermal stability in stand-alone laser applications. For all thermal simulations, the absorption spectra were simply red-shifted with increasing temperature. Note that a temperature rise effectively decreases positive detuning by 0.4 nm/K as the DFB wavelength also shifts by $+0.1 \text{ nm/K}$.

8.3.2 Thermally Induced Wavelength Shift

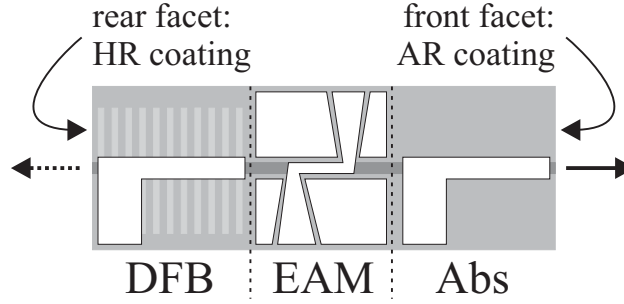


Fig. 8.5: Schematic of the contact layout of the device under test. Section separations are indicated by dashed lines.

The thermal model was confirmed by measurements on device D featuring an additional absorber section. The contact layout of the device is illustrated in Fig. 8.5. Under standard operating conditions, the absorbing region is either omitted or forward biased to act as an additional semiconductor optical amplifier (SOA), and intensity modulated light exits the front facet. The peak wavelength is measured at the rear facet where the intensity level is independent of the EAM bias and always well above the noise level. Furthermore, the long absorbing section avoids reflections from the front facet.

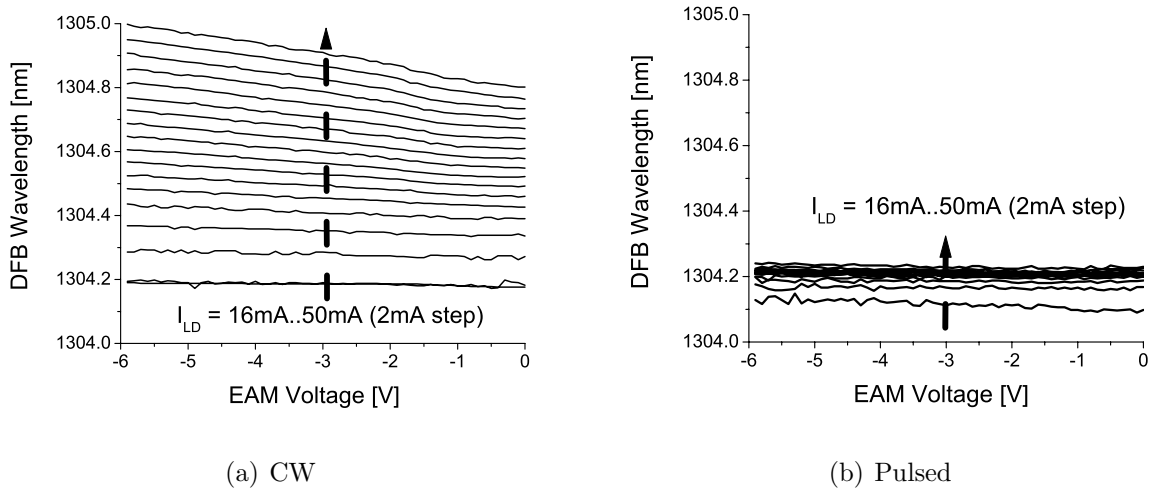


Fig. 8.6: Experimental DFB peak wavelength of device D for different laser currents and variable modulator voltage under continuous wave (CW) and pulsed (1:100 duty cycle) operating conditions at room temperature [38].

A linear DFB wavelength shift with reverse modulator bias is observed in Fig. 8.6(a). The slope depends on the input optical power that is proportional to the laser current above threshold. To explain this result, the measurement was repeated driving the laser in pulsed mode rather than in continuous wave (CW) mode. The pulse length was $1\text{ }\mu\text{s}$ with a duty cycle of 1:100. The results are shown in Fig. 8.6(b). The voltage dependency of the wavelength shift has vanished, identifying the thermal nature of the effect. Note that the pulse length is rather long, leading to a slight shift of the laser wavelength with increasing laser current. This laser self-heating takes place on a much faster time scale than the thermal crosstalk due to the limited thermal spreading velocity. From the absorption change in the EAM and the maximum wavelength shift in the DFB, an adiabatic chirp parameter $\alpha_{H,0-6V} = \Delta n_{\text{eff},r,\text{LD}} / \Delta n_{\text{eff},i,\text{EAM}} = 0.13$ is obtained for the device, with $n_{\text{eff},r,\text{LD}}$ and $n_{\text{eff},i,\text{EAM}}$ being the real and imaginary parts of the complex refractive index in DFB and EAM, respectively.

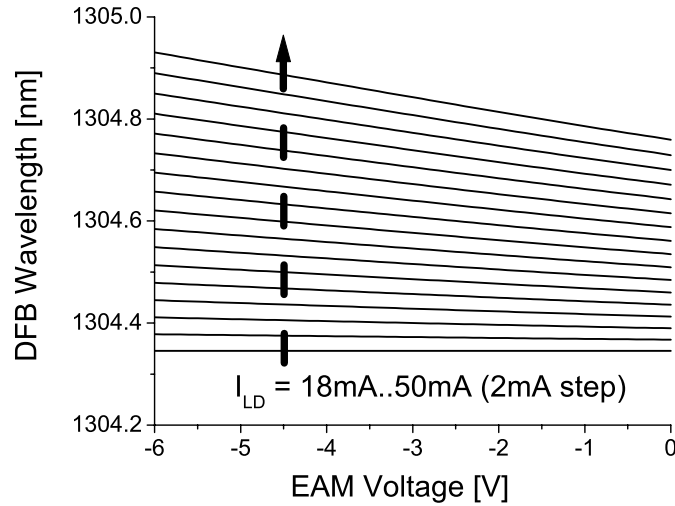


Fig. 8.7: Simulated wavelength shift of device D due to modulator induced heating and laser self-heating in comparison to measurement data of Fig. 8.6(a).

Figure 8.7 shows the calculated wavelength shift with modulator bias. Equation (8.1) includes the explanation for the set of curves. Considering that $q_{\text{EAM}} \propto J_{\text{EAM}} V_{\text{EAM}}$, the amount of heat generated in the modulator and the induced average temperature rise in the laser due to crosstalk is directly proportional to the modulator voltage. The slope is given by the modulator current, which is proportional to the optical input power and thus to the laser current.

The measured data fit the simulation well. However, the calculated wavelength shift is smaller than in the experiment. This discrepancy is attributed to non-ideal thermal coupling of the chip to the heat sink and the non-self-consistent nature of the simulation. In the experiment,

higher EAM temperatures lead to higher absorption, further amplifying the thermal heating. This positive feedback can even lead to the destruction of integrated devices in the EAM section.

8.3.3 Enhanced Thermal PI Roll-Over

All PI characteristics show either an exceptionally strong thermal roll-over in comparison to stand-alone DFB lasers or other non-linearities like kinks or bends. Both are thermal effects that vanish under pulsed operation. Figure 8.8 compares the experimental and simulated PI roll-over of device D.

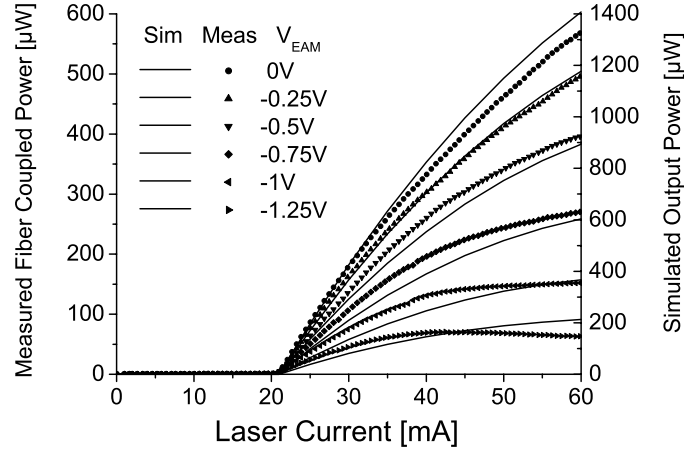


Fig. 8.8: Simulated and experimental results on the increased thermal roll-over of device D. The fiber coupling efficiency is 0.43.

The reason for the loss in output power with laser current is a temperature rise in the modulator. The higher the input power, the more heat is generated leading to enhanced absorption, see equation (8.1) and Fig. 8.4. Due to the thermal roll-over, the static extinction ratio increases with the laser current. The dynamic extinction ratio is always smaller than in the static case.

Mode jumping with modulator bias is caused by thermal crosstalk. Again, the modulator temperature increases with its bias. The partial feedback on the laser changes the boundary conditions for the guided modes. If multiple modes are present, chaotic mode switching can result.

Thermal crosstalk can only be avoided by the incorporation of passive waveguide sections between the laser and modulator. This is not possible for the investigated EMLs as the unbiased shared active area always features a non-zero absorption coefficient. Fortunately, thermal crosstalk effects vanish under high-speed operation since their time constants lie in the range of microseconds.

Chapter 9

Modulation Behavior

This chapter is dedicated to the high-speed performance of integrated absorption modulators which is limited by intrinsic and parasitic capacitances. Parasitics like pad or ridge capacitance can be minimized by way of improving device geometry design with certain trade-offs. In contrast, the intrinsic capacitance is necessary for absorption control.

Unlike Mach-Zehnder components, photo carriers are created and pile up in the active area of an electroabsorption modulator until they escape into the conducting claddings. The actual carrier dynamics are of secondary interest as the final carrier distribution is reached within a few picoseconds for an abrupt field change [45]. However, once the stationary carrier density is established, the amount of carriers trapped in the active region strongly depends on their escape time and the input optical power. As electrons and holes leave the intrinsic area to the opposite terminals, a charge separation is caused that builds up a screening electric field. This is equivalent to the polarization of a dielectric in a classic capacitor similar to the case shown in Fig. 9.1. Electrons and holes increase the intrinsic capacitance and thereby lower the modulation bandwidth.

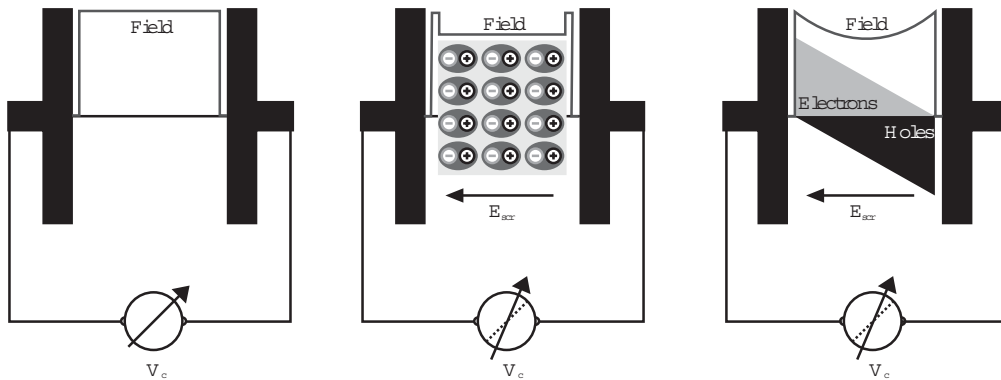


Fig. 9.1: Comparison of a dielectric and a carrier generation process within a capacitor. The first capacitor is empty. The second and third contain a neutral but polarized charge density due to the presence of a dielectric and a carrier generation process, respectively. In both cases, the voltage $V_c = \int |\vec{E}| ds$ across the capacitor decreases and its capacitance $C = Q/V_c$ increases due to a generated screening field.

The concept of a single grown active area imposes two major challenges on the EAM design. First, the operating wavelength has to be close to the bandgap in order to achieve sufficient gain in the DFB section for low laser threshold currents. Therefore, the residual absorption in the EAM is high and the bias voltage is limited to low values for sufficient output power. Both can result in serious carrier pile-up effects, which in turn increase the pin capacitance. Second, the DFB grating layer acts as an etch stop layer during the ridge fabrication process in both sections. The spacing between the grating layer and the waveguide is chosen to optimize the coupling coefficient in the laser section. The consequence of the remaining layer is unwanted lateral conductance in the EAM section. At low modulation frequencies, the effective capacitance becomes larger and degrades RF performance, see Fig. 9.2.

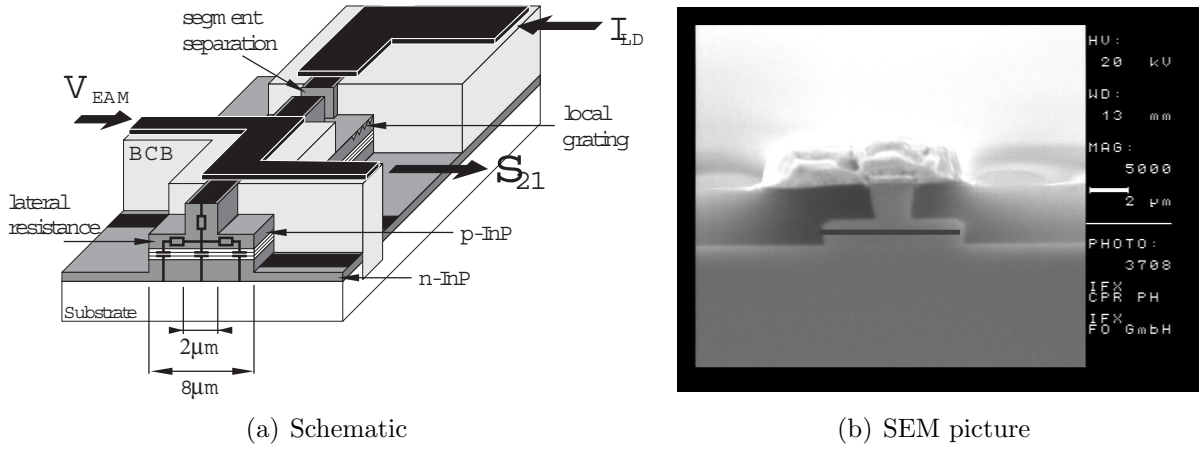


Fig. 9.2: Device schematic and SEM image of the EAM facet.

The chapter is organized as follows. Without going further into detail, Section 9.1 shows the results of dynamic carrier simulations for an abrupt bias change. It validates the proposal that these picosecond time scale effects will not influence modulation behavior up to 40 Gbps and a quasi-static carrier distribution model is sufficient. This is presented in Chapter 9.2. It is similar to the forward injection model for the gain discussion and provides an expression for the intrinsic capacitance under carrier generation and reverse bias $C(P_{\text{abs}}, V_{\text{EAM}})$. This capacitance enters an equivalent circuit model that accounts for the source and measurement setup, parasitics and lateral ridge conductance. In Chapter 9.4, small signal measurements are reproduced with high accuracy for various bias points. The simulation enables the forecast of design changes that finally lead to devices with 40 GHz bandwidth and 40 Gbps eye diagrams introduced in Section 9.5.

9.1 Dynamics of the Active Region

A self-consistent model was used to identify the time resolved carrier transport. In this model, the intrinsic region is divided into slices with and without QWs. The carrier movement is described using field dependent time constants for drift, diffusion, escape and recapture

[46, 45]. Additionally, the electric field is calculated for every time step. Figure 9.3(a) plots the stationary solution for the distribution of free and bound electrons (bottom) and holes (top) in conjunction with the resulting electric field across the intrinsic area. It is reached 4 picoseconds after ideal instantaneous switching of the internal modulator voltage across the intrinsic region.

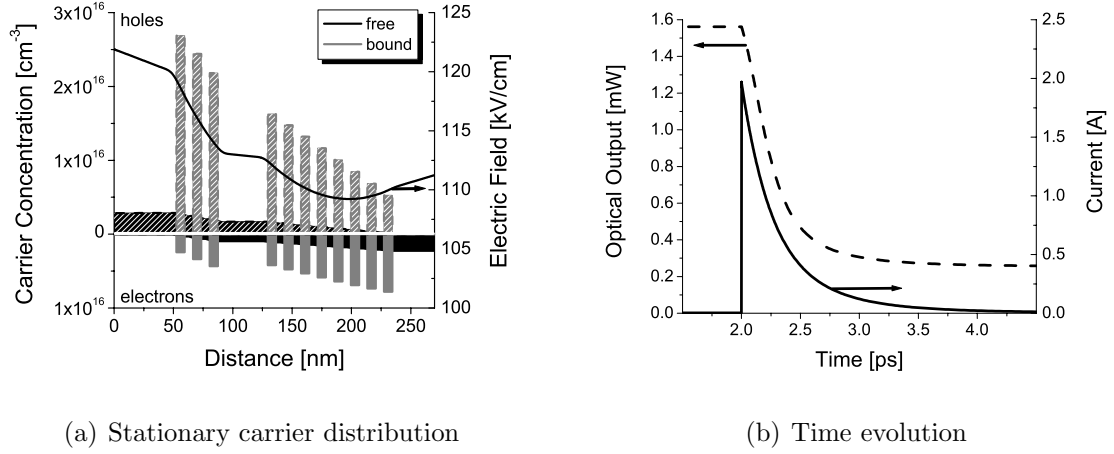


Fig. 9.3: Carrier dynamics for the QW structure II. (a) Stationary solution for the distribution of free and bound electrons (bottom) and holes (top) in conjunction with the resulting electric field across the intrinsic area. (b) Time evolution of optical output and modulator current. The optical input power is $P_{\text{in}} = 5 \text{ mW}$ and the modulator bias is instantaneously switched from $V_{\text{EAM}} = 0 \text{ V}$ to -2 V at $t = 2 \text{ ps}$. The total electric field in (a) shows the characteristic bending in the presence of a screening field.

Time dependent current and output power in Fig. 9.3(b) indicate that the stationary solution is reached after two to three picoseconds. This is in the same order of magnitude as the escape and drift time constants of a few hundred femtoseconds. The strong current spike in the ampere range is caused by the fact that the modulator capacitance acts as a short circuit at the instant of switching. The stationary current is 1.4 mA above its initial value.

9.2 Stationary PIN Capacitance

Section 9.1 showed that in a well designed EAM steady-state carrier distribution is reached after a few picoseconds. For modulation bandwidths up to 50 GHz, the active area can be modeled as a variable capacitor $C(V_{\text{EAM}}, P_{\text{abs}})$ depending on the absorbed optical power and the reverse bias voltage. The stationary band diagrams for reverse bias of Fig. 9.4 were calculated by the 1D drift/diffusion semiconductor simulation of Appendix D, additionally featuring a carrier generation term and carrier mobilities including saturation velocity [26]:

$$P_{\text{abs}}^{\text{QWi}} = P_{\text{in}} (1 - e^{-\tilde{\alpha} l_{\text{EAM}}}) \frac{\Gamma_{\text{QWi}} \alpha_{\text{QWi}}}{\tilde{\alpha}} \quad (9.1)$$

$$G_{QWi} = \frac{P_{\text{abs}}^{QWi}}{\hbar\omega} \frac{1}{d_{QWi} l_{\text{EAM}} w} \quad (9.2)$$

$$\mu_N(|\vec{E}|) = \frac{\mu_N}{1 + \frac{\mu_N |\vec{E}|}{v_s}} \quad (9.3)$$

$$\mu_P(|\vec{E}|) = \frac{\mu_P}{1 + \frac{\mu_P |\vec{E}|}{v_s}} \quad (9.4)$$

P_{abs}^{QWi}	absorbed power in i th QW, ≈ 1 mW
P_{in}	EAM input power, ≈ 12 mW at 40 mA above threshold current
$\tilde{\alpha}$	modal absorption, $= \sum \Gamma_{QWi} \alpha_{QWi} \approx 60 - 480/\text{cm}$
l_{EAM}	EAM length, $= 120 \mu\text{m}$
Γ_{QWi}	i th QW confinement factor, $\approx 1.1\%$ (5 nm QW), $\approx 1.7\%$ (7.5 nm QW)
α_{QWi}	i th QW material absorption, $\approx 50 - 400/\text{cm}$
G_{QWi}	i th QW generation term, $\approx 2.75 \cdot 10^{26}/(\text{cm}^3 \text{s})$
$d_{QWi} l_{\text{EAM}} w$	i th QW active area, $= 2.4 \cdot 10^{-12} \text{cm}^3$
$\mu_N(\vec{E}), \mu_P(\vec{E})$	field dependent carrier mobility
μ_N, μ_P	equilibrium carrier mobility, $= 4700 \text{cm}^2/(\text{Vs})$, $50 \text{cm}^2/(\text{Vs})$ [25]
$ \vec{E} $	electric field, $\approx 35 - 100 \text{kV/cm}$
v_s	saturation velocity, $= 10^7 \text{cm/s}$ [26]

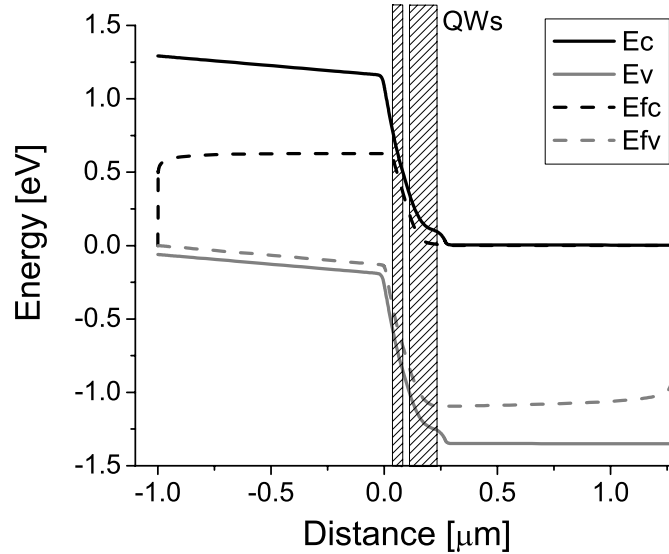


Fig. 9.4: Simulated band diagram of device D for zero bias and carrier generation due to light absorption. The active area is between 0 and 270 nm. The absorbed optical power is $P_{\text{abs}} = 10$ mW.

Even in the absence of an external bias voltage, carrier generation causes splitting of the quasi-Fermi levels. In contrast to forward pumping, the boundary conditions do not allow

for flat band conditions. After the carrier distribution is derived from the band diagrams, the capacitance at a certain bias point is calculated by the total charge change within the structure for a small bias voltage change. Due to charge neutrality, the integral over electron and hole densities is equal.

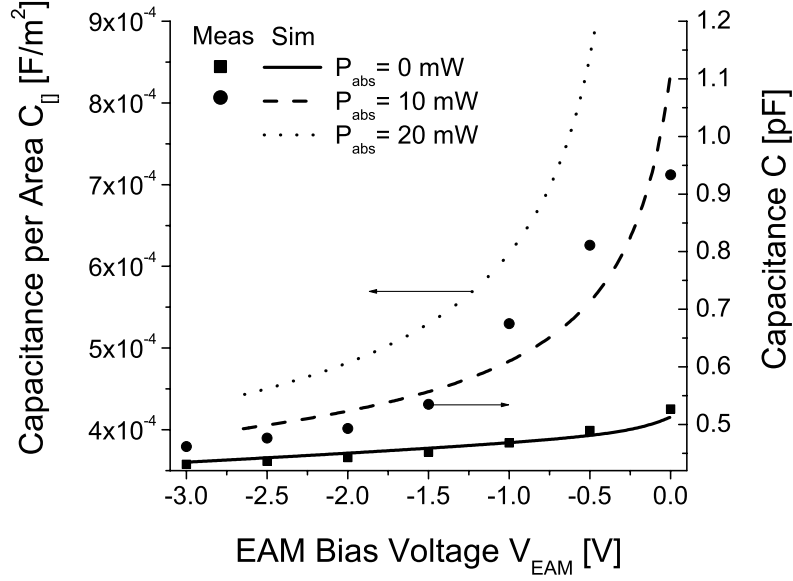


Fig. 9.5: Simulated and experimental capacitance per unit area of device D ($w_{2nd} = 8 \mu\text{m}$ second mesa, $120 \mu\text{m}$ long). The measurement results are extracted from the electrical reflection coefficient for small frequencies. They include a pad capacitance of 0.21 pF .

Figure 9.5 shows the simulated capacitance per area of the active region together with measurement results. Without input light, the capacitance decreases with reverse bias as the space charge region (SCR) increases. With optical input, photo carriers are generated and separated by the electric field. Similarly to a dielectric in a capacitor, they create a screening field that weakens the initial field and increases the capacitance. For low reverse bias voltages and high optical power, the effect escalates as soon as the screening field reaches the order of magnitude of the external field. Under such circumstances, the carriers no longer reach saturation velocity.

9.3 Small Signal Equivalent Circuit Model

In the next step, the calculated intrinsic capacitance is introduced into the equivalent circuit model of Fig. 9.6 that accounts for the parasitics and the 50Ω electrical measurement environment.

The two lateral capacitances $C_{11,2}$ vary for different bias voltages only, while the capacitance

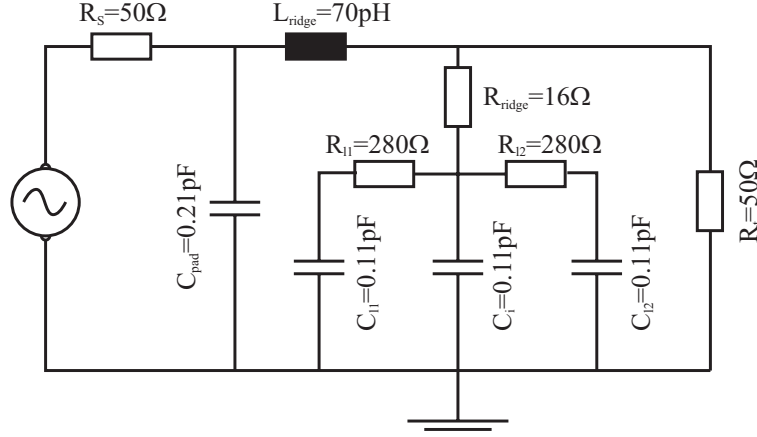


Fig. 9.6: Equivalent circuit model of device D for zero bias and no optical input power.

under the ridge C_i is also influenced by the optical input power. The differential ridge series resistance R_{ridge} is taken from forward modulator VI graphs above the turn-on voltage. The ridge inductance L_{ridge} is estimated by the well-known single-wire inductance relationship [13]. The pad capacitance C_{pad} for a conducting substrate was derived in Section 6.3.2. Etched down to the same layer, the lateral resistances $R_{11,2}$ are calculated similar to the separation resistance in Section 5.3.2. The resistor is $2.5\ \mu\text{m}$ long and has a cross-section of $120\ \mu\text{m} \times 100\ \text{nm}$. For a device without second mesa step, the lateral parasitic elements vanish.

9.4 Initial Small Signal Measurements

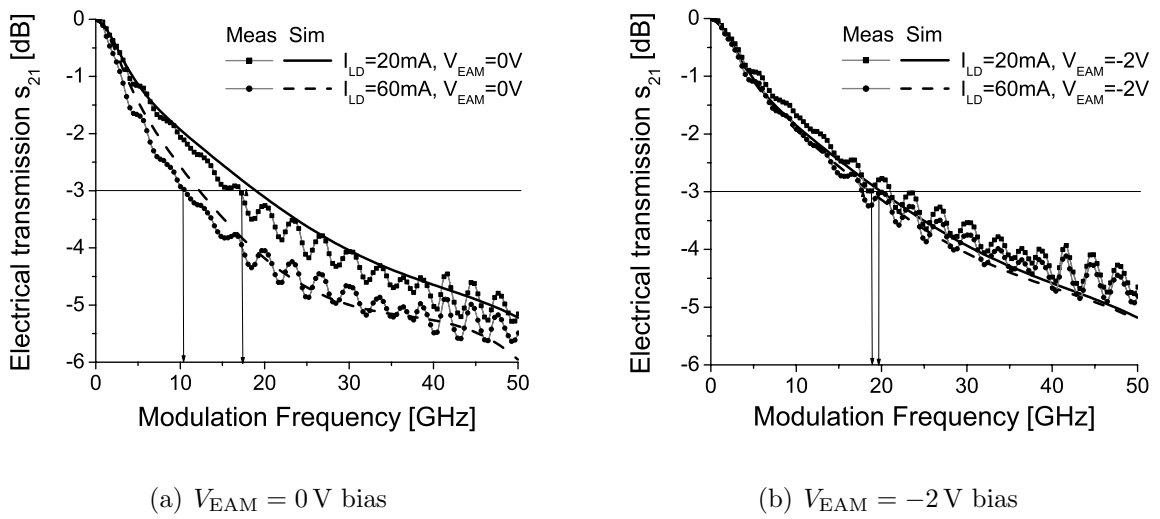


Fig. 9.7: Simulated and experimental electrical transmission of device D. The ripples originate from an imperfect impedance matching.

To examine the capacitance change, the electrical transmission through the modulator trav-

eling wave contact is measured for different modulator and laser bias points. With this procedure, other bandwidth limiting effects like optical feedback or detector speed are eliminated. Figure 9.7 shows simulated and experimental small signal graphs of the EAM traveling wave contact with excellent agreement. While the 3 dB bandwidth is almost independent of the optical power at -2 V EAM bias, it is cut in half at 0 V bias and 60 mA laser current due to carrier pile-up. All graphs show a major decrease in response below 10 GHz. At low frequencies, the lateral resistance below the ridge connects the outer intrinsic areas. This causes the steep descent in small signal behavior due to the capacitance that is now three times larger. The higher the lateral resistance, the smaller is the degradation in bandwidth. With the first layout, the bandwidth is limited to approximately 18 GHz.

For the redesign, three major changes were introduced. First, the structure was grown on a semi-insulating substrate to reduce the pad capacitance. Second, the $2\text{ }\mu\text{m}$ EAM ridge was etched through the active region with a nitrogen based dry-etching process. Third, the detuning of the DFB wavelength to the QW photoluminescence was increased, sacrificing laser threshold current for less residual absorption. The corresponding predictions of small signal behavior are shown in Fig. 9.8. Modulation bandwidths of 40 GHz are accessible with reasonable output power and laser threshold.

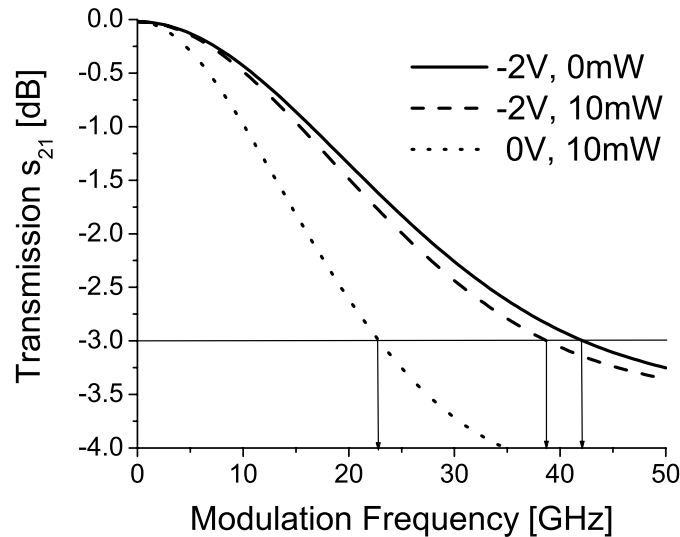
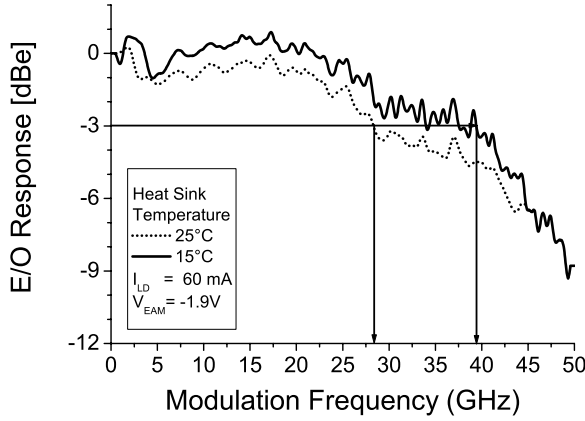
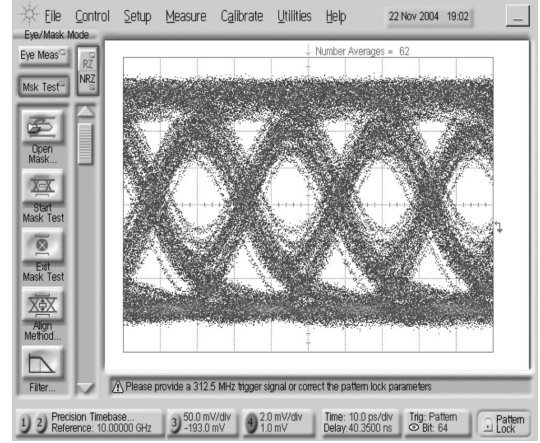


Fig. 9.8: Simulated electrical transmission of a modulator without a second mesa step, on s.i. substrate and with 30 nm detuning for different bias voltages V_{EAM} and absorbed optical powers P_{abs} .



(a) Small signal



(b) 40 Gbps eye diagram

Fig. 9.9: Experimental electro-optic small signal measurement of device C [24] and large signal eye diagram of device A [38]. The averaged eye diagram is measured at $I_{LD} = 50$ mA laser current, $V_{EAM} = -1$ V modulator bias voltage, $V_{pp} = 2$ V driver swing and a bit pattern length of $2^7 - 1$.

9.5 High-Speed Results after Redesign

Figure 9.9 shows the dynamic electro-optical results of the optimized designs. The small signal modulation bandwidth is about 30 GHz at room temperature, enabling 40 Gbps large signal modulation. The bandwidth approaches 40 GHz for lower temperatures. The additional detuning of 4 nm for a 10°C temperature change is sufficient to lower the residual absorption, avoiding carrier pile-up and the related increase of the modulator capacitance. Note that the static characteristics of these devices were also measured at low temperatures. To avoid cooling, larger detuning must be chosen to obtain the same performance at room temperature.

The eye diagram shows clear eye opening at 40 Gbps modulation. The dynamic extinction ratio is approximately 8 dB. Unfortunately, the low output power requires averaging to overcome the noise level.

The chapter showed that EMLs with the integration concept of a shared active area throughout all sections are in principle capable of 40 Gbps operation. Future works [24, 38] will have to concentrate on optimization of the modulator microwave contacts and on increasing average optical output power. Electrical and optical crosstalk between the laser and modulator sections have to be investigated carefully.

Chapter 10

Conclusion

This thesis presents an investigation of integrated absorption modulated lasers (EMLs) with an identical active area in laser and modulator sections. Motivated by better performance of edge emitting lasers, the main objective of the study was the transfer of design criteria from the well-known GaInAsP on InP material system to the novel AlGaInAs on InP active material. The results obtained can be grouped into three major categories: the transfer to the aluminum system itself, the high-speed optimization process after an initial iteration, and the incorporation of metal grating distributed feedback (DFB) lasers.

The transfer to the novel material system was initialized by a number of numerical tools. Simulation approaches concerning fundamental material properties like absorption, gain and waveguiding were presented in Chapters 3 to 5. As theory that ends in itself is fruitless, all results were carefully compared to experiments carried out on corresponding test structures. Thus, the models were tailored to the particular design demands and achieved an impressive level of accuracy in subsequent experimental results. For example, EML waveguide effective indices are determined with an error below 0.1% for both grating types, and absorption and gain spectra are within the uncertainty of the measurement method. This knowledge base enabled the deduction of device design rules in Chapter 6, and the assertion of initially unexplainable effects like thermal crosstalk and the lateral double-mode behavior of metal grating DFB lasers in Chapter 8 and Section 7.3, respectively.

A main design feature originating from the phosphorus material system was the growth of additional quantum wells (QWs) with smaller bandgap on the p-side of the active area. Acting as a primary recombination paths due to hole trapping, they are supposed to deliver gain at longer wavelengths permitting additional detuning. However, drift/diffusion simulations suggested that this benefit is lost in the aluminum system, indicating a homogeneous carrier distribution among the wells. Thus, absorption, gain, photoluminescence (PL) and chirp spectra simply average between the individual QW contributions. In the experiment, devices with one and two QW types showed similar performance. Since the double stack QW approach increases fabrication complexity and prevents reliable room temperature PL measurements, it is omitted in more advanced designs.

In this context, the concept of an identical active layer EML was successfully transferred to the aluminum system with a single QW type. A low residual absorption of 3 dB in a $120\text{ }\mu\text{m}$ long modulator section was measured along with a laser threshold current of 30 mA for positive detuning of 30 nm between DFB and PL wavelengths. This is enabled by the very abrupt band edge and steep exciton slope of the aluminum system proved by absorption simulations and specific test devices presented in Chapter 3.

In the second iteration, the very limited bandwidth of the first generation layouts was boosted from roughly 10 to 32 GHz at room temperature. For the first time worldwide, a 40 Gbps eye diagram was recorded for shared active area EMLs in the aluminum material system. This major step was achieved by careful optimization of the intrinsic and parasitic capacitances with corresponding simulation tools presented in Chapter 9. The key design features are increased detuning, omission of the second mesa step in the EAM section, and growth on semi-insulating substrates. Besides large bandwidths, the component was characterized by 8 dB dynamic extinction ratio for a 2 V peak-to-peak driver signal. A sidemode suppression ratio of 45 dB was accomplished. With a small footprint of $500\text{ }\mu\text{m} \times 500\text{ }\mu\text{m}$ and exploiting epitaxial growth similar to stand-alone DFB lasers with an inherent 100% laser-modulator coupling efficiency, the concept of a low-cost 40 Gbps transmitter with low driver voltage swing was successfully demonstrated. From simulations, a slightly positive chirp parameter of $\alpha_H = +1$ was predicted. Future work will have to concentrate on detailed treatment of time resolved chirp behavior [24].

However, high-speed transmission does not only impose challenges on the modulation bandwidth but also on the average optical output power. This is explained by an increase in thermal noise proportional to the measurement bandwidth. Unfortunately, the only ITU requirement that could not be fulfilled by the investigated EMLs was the mean output power. Very low power is attributed to high residual absorption and roughness scattering in modulators with and without a second mesa step, respectively. In forthcoming designs, modulators with a second mesa step etched down to the active area or to an additional intrinsic InP spacer can avoid lateral conductivity and preserve lossless waveguiding at the same time. A similar performance can be achieved by an optimized second mesa etch process with negligible sidewall roughness.

Additionally, high optical input power remains a critical issue for the EML integration concept addressed in this thesis. Chapter 9 proves that a bias voltage of -2 V at the EAM is necessary to maintain modulation behavior for reasonable input power. However, shared active area EMLs are restricted to a much smaller modulator bias to circumvent high residual absorptions. For 0 V bias, the modulation bandwidth is approximately cut in half compared to its maximum value of 32 GHz due to carrier pile-up. Future work has to address this topic, sacrificing laser threshold for higher detuning values or including additional semiconductor optical amplifiers.

In another effort, EMLs including metal grating distributed feedback (DFB) lasers were de-

signed and manufactured for the first time worldwide. The tested components feature a bandwidth exceeding 20 GHz. Output powers and extinction ratios show performance similar to their index grating counterparts. Waveguide simulation indicated a single-mode yield close to 100% for metal grating EMLs. This was confirmed by numerous experimental EML spectra. These devices are promising for a major reduction in fabrication cost, increasing single-mode yield and enabling single-step epitaxial growth. Further treatment on this promising topic will be given in [38].

As of today, the 40 Gbps market is still small. However, the valuable findings of this thesis are simply transferred to 10 Gbps applications at 1550 nm operating wavelength. Here, EMLs are on their way to replace direct modulated lasers due to their superior chirp behavior [5], increasing the maximum link distance by a factor of eight or more. The limited bias does not restrict device performance for 10 Gbps systems due to relaxed power and bandwidth requirements. Even hybrid integration schemes end up with an operating wavelength close to the EAM band edge to guarantee a negative chirp parameter [5]. Being less expensive and more reliable than those concepts, EMLs with identical active area have the potential to dominate the market.

Summarizing, this thesis lays a solid foundation for future research into and development of EMLs with an identical active layer integration scheme. It provides the reader with numerous simulation approaches and design rules to optimize EMLs in the AlGaInAs on InP material system. Efficient metal grating EMLs were designed and investigated. They show high yield single-mode operation and their modulation bandwidth exceeds 20 GHz. 40 Gbps large signal modulation was successfully demonstrated using optimally designed index coupled devices. These results demonstrate that EMLs are extremely attractive light sources for highest speed fiber-optic communication systems.

Appendix A

Material Fundamentals

Semiconductor solid-state lasers and optoelectronic devices are usually fabricated from binary, ternary or quaternary III-V compound materials such as GaAs, InP, AlGaAs or AlGaInAs. To name only a few, knowledge of material band structure, carrier mass, lattice constant or refractive index is fundamental for calculating and understanding device specific parameters like absorption, gain, waveguiding, temperature distribution or modulation characteristics.

While binary material parameters are well-known from measurements on bulk structures, higher order compounds can often be characterized by simulations only. Usually, a linear parameter interpolation referred to as Vegard's law is performed between the binary ingredients as presented in Section A.1. Some parameters like bandgap or refractive index cannot be interpolated directly but by the incorporation of auxiliary variables. Unfortunately, knowledge of relaxed ternary or quaternary material parameters is not sufficient for practical application purposes. Compound semiconductors are often deposited in thin layers on a substrate material. Up to a critical thickness, the lattice constant of the overgrown layer changes as to match the lattice constant of the substrate material. This lattice mismatch causes strain that will in turn affect the band lineup as presented in Section A.2. Additionally, thin layers with thicknesses in the range of the electron wavelength form quantum mechanical systems that will influence the energy states by adding confinement energy. Finally, the interaction between two or more particles may result in additional energy states. Both effects are described in Sections A.3 and A.4, respectively.

This chapter provides only a brief overview of solid-state theory. It will predict input parameters for the simulations on absorption, gain and waveguiding. A more detailed treatment of optoelectronic related semiconductor physics is given by [12]. All typical values in this chapter correspond to a 6.5 nm thick AlGaInAs quantum well (QW) for 1310 nm operating wavelength, sandwiched between 1100 nm photoluminescence wavelength AlGaInAs barriers on an InP substrate.

A.1 III-V Compound Semiconductors

For ternary or higher order compound materials, important semiconductor parameters can be interpolated from their binary compounds by a linear or quadratic law [47]. For three group III and one group V element as for $\text{Al}_x\text{Ga}_y\text{In}_{1-x-y}\text{As}$, it is written as:

$$\mathbf{z} = 1 - \mathbf{x} - \mathbf{y} \quad (\text{A.1})$$

$$\begin{aligned} \text{par}_{\text{A}_x\text{B}_y\text{C}_z\text{D}} &= \mathbf{x} \cdot \text{par}_{\text{AD}} + \mathbf{y} \cdot \text{par}_{\text{BD}} + \mathbf{z} \cdot \text{par}_{\text{CD}} + \\ &\quad \mathbf{xy} \cdot \text{bow}_{\text{ABD}} + \mathbf{xz} \cdot \text{bow}_{\text{ACD}} + \mathbf{yz} \cdot \text{bow}_{\text{BCD}} \end{aligned} \quad (\text{A.2})$$

A,B,C	group III element, e.g. Al, Ga, In
D	group V element, e.g. P, As
$\mathbf{x}, \mathbf{y}, \mathbf{z}$	compound fractions
par	semiconductor parameter, e.g. bandgap, electron mass
bow	bowing value corresponding to par

Appendix G lists important parameters of binary semiconductors. For the majority of cases, a simple linear interpolation expressed by the first three terms in equation (A.2) is sufficient. This behavior was originally identified by Vegard concerning the lattice constant (A.2). Other cases diverge from this straight behavior and must be fitted with a second order parabolic term represented by the so-called bowing value. Often, zero bowing will be used in the absence of exact measurement data. With some exceptions, most parameters are calculated directly. Usually, the effective masses m_{hh}^z and m_{lh}^z are interpolated rather than the Luttinger parameters γ_i . In the same way, the Adachi parameters A and B are interpolated, not the refractive index n . Finally, the zero degree bandgap E_{g0} and the Varshni bandgap temperature dependence constants α and β are interpolated instead of $E_g(T)$. The interrelation between these parameters is given in the following equations (A.3) to (A.7). The relation between the valence band curvature and the effective hole masses is expressed by the characteristic Luttinger parameters [20]:

$$\gamma_1 = \frac{m_0}{2} \left(\frac{1}{m_{\text{lh}}^z} + \frac{1}{m_{\text{hh}}^z} \right) \quad (\text{A.3})$$

$$\gamma_2 = \frac{m_0}{4} \left(\frac{1}{m_{\text{lh}}^z} - \frac{1}{m_{\text{hh}}^z} \right) \quad (\text{A.4})$$

γ_1, γ_2	Luttinger parameter, ≈ 8.6 and 3.0 , respectively
m_0	free electron mass, $= 9.11 \cdot 10^{-31} \text{ kg}$
$m_{\text{hh}}^z, m_{\text{lh}}^z$	heavy and light hole mass in growth direction, $\approx 0.38, 0.06 m_0$, respectively

The temperature dependence of the bandgap is described by the empiric Varshni equation [20]:

$$E_g(T) = E_{g0} - \frac{\alpha \cdot T^2}{T + \beta} \quad (\text{A.5})$$

E_g	semiconductor bandgap energy, ≈ 0.86 eV at 300 K
E_{g0}	semiconductor bandgap energy at 0 K, ≈ 0.94 eV
α	1st Varshni parameter, ≈ 0.43 meV/K
β	2nd Varshni parameter, ≈ 191 K

There are many empirical and theoretically derived expressions for the refractive index. Within this work, the Adachi equation [44] was identified to yield excellent values compared to waveguide measurements:

$$f(x) = \frac{1}{x^2} \left(2 - \sqrt{1+x} - \sqrt{1-x} \right) \quad (\text{A.6})$$

$$n_R^2(\hbar\omega) = A \left[f\left(\frac{\hbar\omega}{E_g}\right) + \frac{1}{2} f\left(\frac{\hbar\omega}{E_g + \Delta_{\text{SO}}}\right) \left(\frac{E_g}{E_g + \Delta_{\text{SO}}}\right)^{1.5} \right] + B \quad (\text{A.7})$$

n_R	refractive index (real part)
A	1st Adachi parameter, ≈ 9.1
B	2nd Adachi parameter, ≈ 8.0
$\hbar\omega$	photon energy, = 0.947 eV for 1310 nm wavelength
Δ_{SO}	split-off band distance, ≈ 0.33 eV

The Adachi equations are only valid in the transparent spectral regime, that is for wavelengths longer than the bandgap wavelength. This poses a problem in QW layers. Here, the index must be determined from the absorption or gain spectrum via the Kramers-Kronig relation of Chapter 3.5. As a rule of thumb, material indices are reduced by roughly 0.3 in an amplifying QW. Similarly, doped layers show a reduction in refractive index by 0.02 for a doping concentration of $|N_D| = 10^{18}/\text{cm}^3$ because of free carrier interaction.

A.2 Strained Semiconductor Layers

A thin semiconductor layer will be deformed if it is epitaxially grown on a substrate with a different lattice constant. This usually results in compression or tension in the substrate plane (biaxial) accompanied by opposing behavior in the growth direction (normal), see Fig. A.1.

The lattice mismatch compared to the bulk material is defined as:

$$\text{biaxial strain : } \varepsilon_{xx} = \varepsilon_{yy} = \frac{a_0}{a_1} - 1 \quad (\text{A.8})$$

$$\text{normal strain : } \varepsilon_{zz} = -2 \frac{c_{12}}{c_{11}} \varepsilon_{xx} \quad (\text{A.9})$$

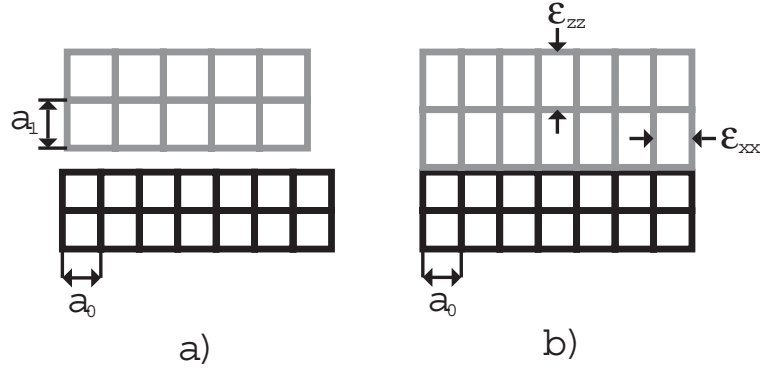


Fig. A.1: Compressive strain of a thin semiconductor layer with an intrinsic lattice constant a_1 grown on a substrate with a smaller lattice constant a_0 .

$\epsilon_{xx}, \epsilon_{yy}$	in-plane (biaxial) lattice tension (mismatch), $\approx 0.5\%$ (Bar), $\approx -0.95\%$ (QW)
ϵ_{zz}	in growth (normal) lattice tension (mismatch)
a_0	substrate lattice constant, = 5.8696 Å for InP
a_1	grown material natural lattice constant, ≈ 5.9259 Å
c_{12}, c_{11}	elastic constants, $\approx 484, 966$ GPa

Depending on their sign, two types of strain are distinguished [12]:

- (biaxial) tensile: $\epsilon_{xx} > 0$
- (biaxial) compressive: $\epsilon_{xx} < 0$

Note that the notation is often interchanged in other literature sources.

In the energy space, deformations result in a shift of the semiconductor band edges. The strain caused by lattice mismatch has two components, namely hydrostatic and shear. Hydrostatic (‘uniform in all directions’) compression lowers the average lattice constant and increases the bandgap energy, since the bandgap and lattice constant are inversely proportional to each other. Hydrostatic strain has the same sign as in-plane strain, affecting two lattice dimensions. The shear strain component accounts for the difference in normal and transversal lattice constant that breaks the lattice symmetry and therefore the degeneration of light and heavy holes. Fig. A.2 [12] illustrates the energy levels of different band edges for tensile and compressive strain present in barriers and QWs, respectively. In the barriers, the tensile strain decreases the overall bandgap and the light hole band edge lies above the heavy hole band edge. In contrast, the compressive strain in the QWs increases the bandgap and the heavy hole subband lies above the light hole subband.

The figure indicates that in compressively strained QWs with tensile strain compensated barriers the heavy hole subband offset is increased and the light hole subband becomes almost flat. The shift of the different band edges in a bulk-like semiconductor at the Γ point ($\vec{k} = 0$) is derived from quantum mechanical $\vec{k}\vec{p}$ calculations [12]:

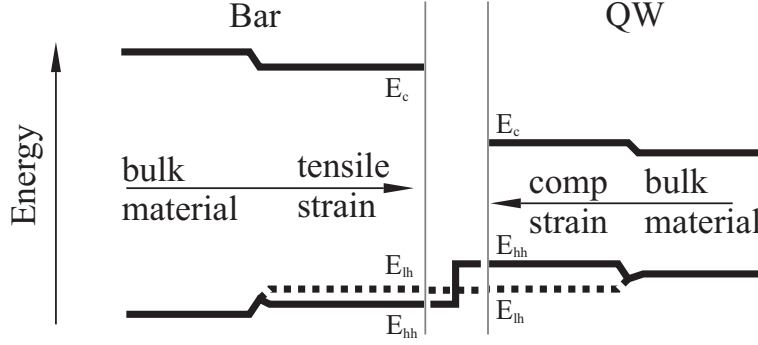


Fig. A.2: Band shifts of tensile strained barriers (left) and compressively strained QWs (right).

$$P_c = a_c \cdot (\varepsilon_{xx} + \varepsilon_{yy} + \varepsilon_{zz}) \quad (\text{A.10})$$

$$P_v = a_v \cdot (\varepsilon_{xx} + \varepsilon_{yy} + \varepsilon_{zz}) \quad (\text{A.11})$$

$$Q_e = \frac{b}{2} \cdot (\varepsilon_{xx} + \varepsilon_{yy} + \varepsilon_{zz}) \quad (\text{A.12})$$

$$E_c = E_g + P_c + VBO \quad (\text{A.13})$$

$$E_{hh} = -P_v - Q_e + VBO \quad (\text{A.14})$$

$$E_{lh} = -P_v + \frac{1}{2} \left(Q_e - \Delta_{SO} + \sqrt{\Delta_{SO}^2 + 2\Delta_{SO}Q_e + 9Q_e^2} \right) + VBO \quad (\text{A.15})$$

P_c	conduction band shift due to hydrostatic strain, $\approx 53 \text{ meV}$ for -0.95% mismatch
P_v	neg. valence band shift due to hydrostatic strain, $\approx 12 \text{ meV}$ for -0.95% mismatch
Q_e	heavy hole subband shift due to shear strain, $\approx 9 \text{ meV}$ for -0.95% mismatch
a_c	hydrostatic conduction band shift constant, $\approx -5.56 \text{ eV}$
a_v	hydrostatic valence band shift constant, $\approx -1.30 \text{ eV}$
b	shear shift constant, $\approx -1.92 \text{ eV}$
E_c	abs. energy level of conduction band edge, $\approx 0.27 \text{ eV}$
E_{hh}	abs. energy level of heavy hole band edge, $\approx -0.62 \text{ eV}$
E_{lh}	abs. energy level of light hole band edge, $\approx -0.68 \text{ eV}$
VBO	unstrained material absolute valence band level, $\approx -0.64 \text{ eV}$

The energy values refer to an absolute energy system suitable for all III-V semiconductors in which the energy level of the bulk InP valence band is at -0.94 eV [20]. Note that the sign of a_v may differ in literature. After the material growth, low excitation photoluminescence (PL) measurement is applied to characterize the semiconductor layers. Electrons and holes are generated by the absorption of high-energy photons ($E_{ph} > E_g$), relax to the lowest bandgap region and recombine radiatively. In strained bulk semiconductors, the PL wavelength is determined by:

$$\lambda_{\text{PL,bulk}} = \frac{1240 \text{ eV nm}}{E_{\text{c}} - \max(E_{\text{hh}}, E_{\text{lh}}) - E_{\text{Stokes}}} \quad (\text{A.16})$$

E_{Stokes}	Stoke's shift due to local fluctuations, $\approx 1 - 2 \text{ meV}$
---------------------	--

The Stoke's shift accounts for the fact that excited carriers relax to local bandgap minima before recombination. Therefore, the PL measurement detects the minimum and not the average bandgap.

Besides its absolute energy position, the curvature of the energy bands and hence effective hole masses are affected by strain [12]. Close to the Γ Point, the $\vec{k}\vec{p}$ method yields the following results:

$$f_1 = \frac{Q_e}{\Delta_{\text{SO}}} - 1 + \sqrt{1 + 2\frac{Q_e}{\Delta_{\text{SO}}} + 9\left(\frac{Q_e}{\Delta_{\text{SO}}}\right)^2} \quad (\text{A.17})$$

$$f_2 = \frac{2\frac{Q_e}{\Delta_{\text{SO}}}\left(1 + \frac{3}{2}f_1\right) + 6\left(\frac{Q_e}{\Delta_{\text{SO}}}\right)^2}{\frac{3}{4}f_1^2 + f_1 - 3\left(\frac{Q_e}{\Delta_{\text{SO}}}\right)^2} \quad (\text{A.18})$$

$$m_{\text{hh}}^z = \frac{m_0}{\gamma_1 - 2\gamma_2} \quad (\text{A.19})$$

$$m_{\text{hh}}^t = \frac{m_0}{\gamma_1 + \gamma_2} \quad (\text{A.20})$$

$$m_{\text{lh}}^z = \frac{m_0}{\gamma_1 + 2f_2\gamma_2} \quad (\text{A.21})$$

$$m_{\text{lh}}^t = \frac{m_0}{\gamma_1 - f_2\gamma_2} \quad (\text{A.22})$$

$m_{\text{hh}}^z, m_{\text{hh}}^t$	heavy hole masses in growth ($\approx 0.38 m_0$) and in-plane direction ($\approx 0.08 m_0$)
$m_{\text{lh}}^z, m_{\text{lh}}^t$	light hole masses in growth ($\approx 0.08 m_0$) and in-plane ($\approx 0.13 m_0$) direction

A.3 Two-Dimensional Electron States

If a quantum mechanical particle is trapped in a potential whose extension is in the range of the De-Broglie wavelength (e.g. a few nanometers for electrons), its energy is divided into a ladder of discrete levels in growth direction. This is equivalent to the forming of discrete

modes in a waveguide. In a semiconductor, the confining potential usually arises from the different conduction and valence band levels of the epitaxial layers. In the perpendicular layer plane, the parabolic dispersion relationship of a quasi-free particle applies.

In a simple approach, the energy states are calculated using the effective mass theory. This approach divides the structure into bulk-like layers with infinite extensions. Only effective masses and energy positions of the band edges of these layers are preserved for further calculations. Thus, it is equivalent to the effective index method for optical waveguides presented in Chapter 5. The procedure is sketched in the following paragraph:

- Effective mass theory (EMT): The particle wavefunction is separated into a product of a fast oscillating part $\Phi(\vec{r})$ with lattice period and a slowly varying envelope $\Psi(\vec{r})$ [12].
- Solving the equation for the lattice periodic part Φ results in effective masses $m_e^z(z)$ and band edges $E_c(z)$ of the different layers. This calculation equals that for a bulk semiconductor.
- The Schrödinger equation for the envelope function Ψ includes effective masses and band edge potentials (‘effective mass theory’) of the different layers. It yields the confinement energies [12]:

$$-\frac{\hbar^2}{2} \frac{d}{dz} \frac{1}{m_e^z(z)} \frac{d}{dz} \Psi(z) + E_c(z) \Psi(z) = E_e \Psi(z) \quad (\text{A.23})$$

$\Psi(z)$	electron envelope wavefunction in $[\text{m}^{-0.5}]$, eigenfunction of the problem
E_e	absolute state energy, eigenvalue of the problem
$m_e^z(z)$	layer effective mass, $\approx 0.05 m_0$ for electrons in AlGaInAs
$E_c(z)$	layer conduction band energy position, $\approx 0.44 - 0.26 \text{ eV}$ for barrier and QW

Similar expressions are applied to light and heavy holes, respectively.

- For a multiplication approach of eigenfunctions, the corresponding eigenvalue is a sum of the individual eigenvalues: $E = E_\Psi + E_\Phi$. For example, the potential energy of the electron ground state is $E = E_c + E_{e1}$, with E_c evaluated at the center of the QW.
- Standard EMT including band-to-band coupling uses an $[8 \times 8]$ Hamiltonian [12]. For the investigated structures, a single-band approximation assuming parabolic subbands is sufficient. This simplification is valid since the light and heavy hole subbands of the bulk materials are sufficiently separated by strain already. Thus, QW anti-crossing effects for in-plane movement are shifted to high k_t values as shown in Fig. A.3. Close to the Γ point, parabolic bands are a reasonable approximation ¹.

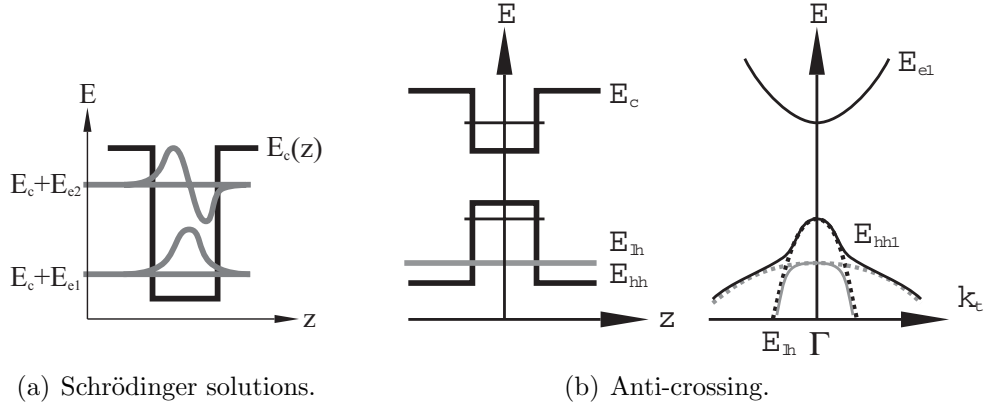


Fig. A.3: (a) 2D electron states for a single energy band. (b) Resulting subband structure and energy dispersion relationship for particle movement in the QW layer plane. The dashed lines indicate the approximation of parabolic subbands. This approximation is valid for small k_t values only.

The rectangular potential is a good approximation for forward current injection resulting in flat energy bands. For reverse bias operation, semiconductor band edges in a pin-structure are tilted due to the sum of internal and external field as depicted in Fig. 2.1. The following expression describes the spatial energy level of the conduction band:

$$E_c(z) = E_g(z) + P_c(z) + VBO(z) + \frac{ez}{d_{pn}} (V_{bi} + V_{EAM}) \quad (\text{A.24})$$

d_{pn}	distance between p- and n-regions, $\approx 150 - 300$ nm
V_{bi}	built-in pin-junction voltage, $= -1.353$ V for highly doped InP
V_{EAM}	external bias voltage, negative sign for reverse operation

Appendix C describes the numerical method used to solve the Schrödinger eigenvalue problem.

Side Note: The heavier a particle, the smaller is the separation between its quantized ground state and the corresponding subband edge. Additionally, the light hole subband lies energetically above the heavy hole subband according to equations (A.14) and (A.15) for tensile strain. Thus, the ground states of heavy and light hole can coincide in a tensile strained QW layer. As light and heavy hole transitions enhance different light polarizations [12], tensile strain is commonly used for stand-alone devices that are polarization independent such as modulators or amplifiers.

¹For increased band filling, the underlying Kröning-Penny model for a single particle in a lattice periodic potential is not a proper approximation anyway. Many particle approaches have to be used

A.4 Excitonic Transitions

The Kröning-Penny model underlies most band structure calculations. It is only valid for a single particle in a lattice periodic potential. In contrast, a semiconductor contains numerous electrons and holes. Although weak, their interaction has to be taken into account for certain investigations, e.g. calculations of absorption spectra close to the band edge. Theoretically, there is no energy state within the bandgap. In contrast, a sharp peak is observed slightly below the band edge. It is explained by an excitonic transition as illustrated in Fig. A.4. This quasi-particle is a construct of an electron and a hole orbiting each other by electrostatic attraction. Its binding energy is the energy missing for a complete excitation into the conduction band.

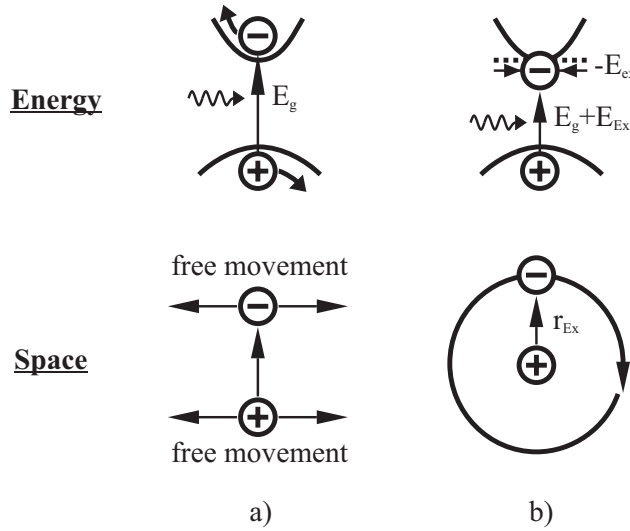


Fig. A.4: Particle transitions. (a) Band-to-band transition resulting in unbound carriers, (b) transition to quasi-free exciton state. Both transitions are shown in energy (top) and spatial (bottom) dimensions.

The exciton energy is calculated by a variational method [12]:

- Initial point: effective mass theory (EMT).
- Approach: compound envelope function $\Psi(\vec{r}_e, \vec{r}_h)$ describing positions of electron \vec{r}_e and hole \vec{r}_h .
- Transition to center-of-mass \vec{R} and distance \vec{r} coordinate system $\Psi(\vec{r}_e, \vec{r}_h) \rightarrow \Psi(\vec{r}, \vec{R})$. The exciton energy is independent on the center-of-mass position \vec{R} in the QW layer plane.
- The envelope wavefunction is separated in two independent functions in growth direction and a distance function: $\Psi(\vec{r}, \vec{R}) = \Psi_e(z_e) \Psi_h(z_h) \Phi(r)$.

- The z functions Ψ are solved by the two-dimensional QW states for electron and hole, respectively.
- The distance function Φ is solved by the characteristic eigenfunctions for hydrogen atoms with an effective radius r_{Ex} .
- The effective radius r_{Ex} is determined by a variational method: $E_{\text{Ex}}(r_{\text{Ex}}) \rightarrow \min_{r_{\text{Ex}}}$. The exciton binding energy depends on parameters such as effective masses, barrier heights, QW thickness and electric field.
- Exciton binding energy and radius are approximately constant for the investigated structures: $E_{\text{Ex}} \approx -5.3 \text{ meV}$, $r_{\text{Ex}} \approx 17.5 \text{ nm}$. Figure A.5 shows the simulation results for the exciton binding energy for different combinations of QW parameters and internal electric fields.

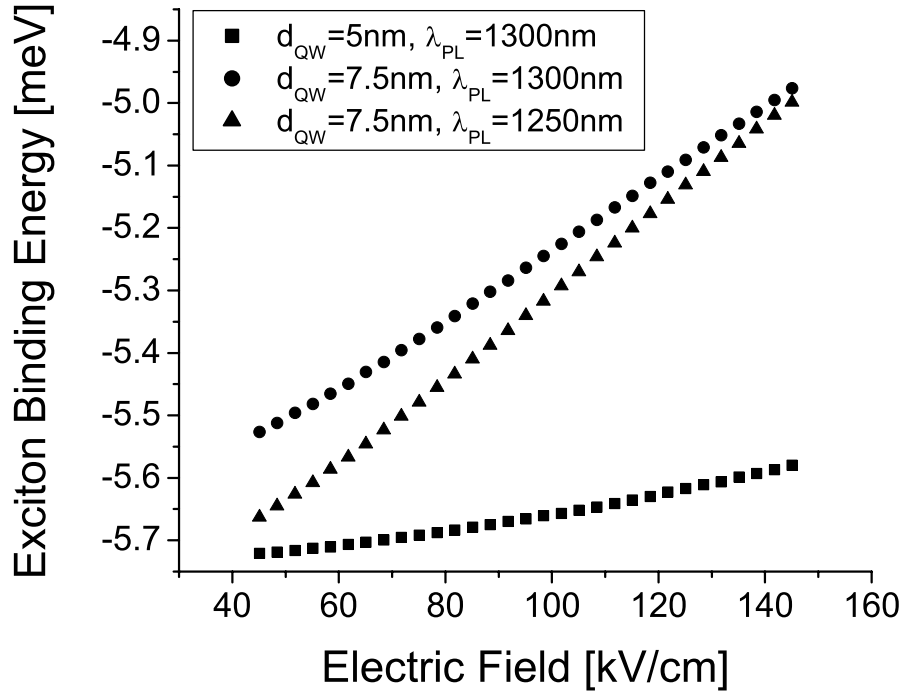


Fig. A.5: Calculated 1S e1-hh1 exciton binding energy for typical QWs.

The three-dimensional continuum and every two-dimensional subband features an excitonic transition. Additionally, every exciton has excited states apart from the S-like ground state [12]. For practical purposes, it is not necessary to solve for all of these transitions. At room temperature, the excited exciton states are within the linewidth broadening of the ground state. They will not be observed unless the experiment is conducted at very low

temperatures. For the treatment of EAM characteristics, mainly the absorption contributions below the bandgap energy are of interest. This regime is dominated by the 1S e1-hh1 exciton transition. All other contributions are negligible. Figure 3.4 on page 15 shows a typical absorption spectrum with the dominant exciton peak close to the bandgap wavelength. For a compressively strained QW, the low excitation PL wavelength is determined by the bandgap energy, the confinement energy and the exciton binding energy:

$$\lambda_{\text{PL,QW}} = \frac{1240 \text{ eV nm}}{E_{\text{c}} - E_{\text{hh}} + E_{\text{e1}} + E_{\text{hh1}} + E_{\text{Ex}} - E_{\text{Stokes}}} \quad (\text{A.25})$$

E_{hh1}	heavy hole confinement energy, field dependent, $\approx 2 - 10 \text{ meV}$
E_{e1}	electron confinement energy, field dependent, $\approx 10 - 80 \text{ meV}$
E_{Ex}	exciton binding energy, $\approx -5.3 \text{ meV}$

A.5 Determination of QW Composition

Quaternary material systems such as $\text{Al}_x\text{Ga}_y\text{In}_{1-x-y}\text{As}$ feature two degrees of freedom. Therefore, two independent measurements are required to determine their composition x, y . For practical purposes, x-ray diffraction measurements on the layer strain ε_{xx} and the photoluminescence wavelength λ_{PL} are used. Unfortunately, the QW PL data include confinement and exciton energy and thus depend on the barrier composition. A preliminary bulk-like test growth ($d > 30 \text{ nm}$) of the barrier material is used to extract the barrier composition. For characterization of the QW, the whole epitaxial structure including barriers and wells is deposited.

To derive the composition from strain and photoluminescence data, an implicit problem has to be solved using the following algorithm:

- Start with a good initial guess for the gallium concentration y !
- Calculate the aluminum concentration x from strain data:

$$\mathbf{x} = \frac{\frac{\mathbf{a}_0}{1+\varepsilon_{xx}} - \mathbf{y} (\mathbf{a}_{\text{GaAs}} - \mathbf{a}_{\text{InAs}}) - \mathbf{a}_{\text{InAs}}}{\mathbf{a}_{\text{AlAs}} - \mathbf{a}_{\text{InAs}}} \quad (\text{A.26})$$

- Calculate the PL wavelength λ_{PL} using equation (A.16) for barrier and equation (A.25) for QW layers!
- Iterate until the error $|\lambda_{\text{PL}} - \lambda_{\text{PL}}|$ has converged!

Appendix B

Absorption and Transition Probability

A general expression for the absorption coefficient in any material is derived from Fermi's Golden Rule of transition probabilities in the presence of a perturbation operator [12]:

$$\alpha(\hbar\omega) = C_0 \frac{2}{dwl} \sum_{\Psi_1, \Psi_2} \left| \langle \Psi_1 | e^{i\vec{k}_{\text{op}}\vec{r}} \vec{e} \vec{p} | \Psi_2 \rangle \right|^2 \delta(E_1 - E_2 - \hbar\omega) [f(E_1) - f(E_2)] * \mathcal{L}_{12}(\hbar\omega) \quad (\text{B.1})$$

$$C_0 = \frac{\pi e^2}{n_{\text{eff}} c_0 \varepsilon_0 m_0^2 \omega} \quad (\text{B.2})$$

C_0	physical constants, $= 7.6 \cdot 10^9 \text{ m}^2/\text{kg}$ at 1300 nm wavelength
n_{eff}	optical wave effective index, ≈ 3.29 for this work's designs
dwl	absorbing volume in $[\text{m}^3]$
$\Psi_{1,2}$	initial and final state envelope functions, corresponding energy $E_{1,2}$, 1D in $[\text{m}^{-\frac{1}{2}}]$
$e^{i\vec{k}_{\text{op}}\vec{r}} \vec{e} \vec{p}$	light perturbation operator $\tilde{H}(\vec{r})$ (except for constants)
\vec{k}_{op}	light wave vector in $[\text{m}^{-1}]$
\vec{e}	unit vector in light polarization direction
\vec{p}	momentum operator $\hbar/i\nabla$ in $[\text{Js/m}]$
$\langle f_1 f_2 \rangle$	function scalar product, projection, overlap $= \int f_1(x) f_2(x) \dots dx$
$ \langle \rangle $	transition matrix element in $[(\text{Js/m})^2]$, [12]
$\delta(E)$	delta function in $[\text{J}^{-1}]$, expresses transition energy conservation
$f(E)$	occupation probability at initial or final state, respectively, no [unit]
$\mathcal{L}_{12}(\hbar\omega)$	linewidth broadening function of the transition, no [unit]

The quantum mechanical picture of absorption given in equation (B.1) is interpreted as follows. A continuous absorption spectrum is composed of individual transitions. This is expressed by the infinite sums including all initial and final states possible. Each transition has its distinct initial and final state and a spectral position according to their energy difference (δ operator). Thus, energy and momentum conservation is included implicitly. The absorption amplitude of a transition is given by its transition probability $\frac{2\pi}{\hbar} |\langle \text{final state} | \text{perturbation} | \text{initial state} \rangle|^2 \delta(E_f - E_i - E_{\text{per}})$ according to Fermi's golden rule and

the initial and final state's occupation probabilities $f_{1,2}$. Transitions show energy broadening expressed by convolutions with individual linewidth functions \mathcal{L} . This represents Heisenberg's energy uncertainty relation and fluctuations of the semiconductor composition.

In bulk or QW semiconductors, 'initial' and 'final' states include electron to heavy hole (ex-hhx) and electron to light hole (ex-lhx) subband transitions and their corresponding excitons. Close to the band edge, only transitions with low energy separation make a significant absorption contribution. For AlGaInAs QWs with +0.5% tensile strained barriers and -0.9% compressively strained wells (compare Fig. B.1), the three major transitions are written as e1-hh1 continuum, e1-hh1 1S exciton and e1-lh continuum. The associated nomenclature is listed in Table B.1. The e-lh exciton is not visible at room temperature as there is no confinement of the light holes.

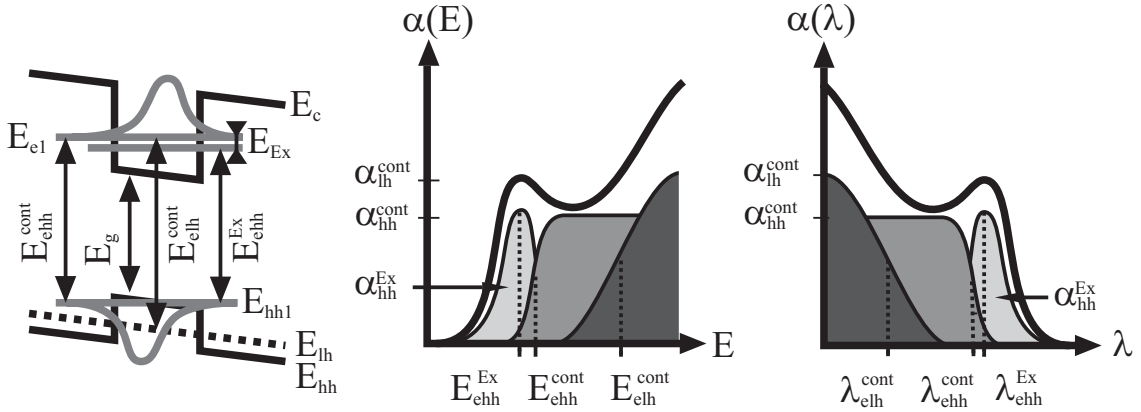


Fig. B.1: Absorption contribution of the three major transitions.

Transition	Transition energy difference	Transition wavelength	Absorption contribution	Absorption amplitude	Linewidth broadening
Electron-heavy hole 2D ground states	$E_{\text{ehh}}^{\text{cont}} = E_g + E_{\text{e1}} - E_{\text{hh1}}$	$\lambda_{\text{ehh}}^{\text{cont}}$	$\alpha_{\text{ehh}}^{\text{cont}}(\hbar\omega), \alpha_{\text{ehh}}^{\text{cont}}(\lambda)$	α_{HH}	$\Delta\lambda_{\text{ehh}}^{\text{cont}}, \mathcal{L}_{\text{ehh}}^{\text{cont}}(E)$
Electron-heavy hole 1S exciton	$E_{\text{ehh}}^{\text{ex}} = E_g + E_{\text{e1}} - E_{\text{hh1}} + E_{\text{ex}}$	$\lambda_{\text{ehh}}^{\text{ex}}$	$\alpha_{\text{ehh}}^{\text{ex}}(\hbar\omega), \alpha_{\text{ehh}}^{\text{ex}}(\lambda)$	α_{EX}	$\Delta\lambda_{\text{ehh}}^{\text{ex}}, \mathcal{L}_{\text{ehh}}^{\text{ex}}(E)$
Electron-light hole 2D ground state - 3D	$E_{\text{elh}}^{\text{cont}} = E_g + E_{\text{e1}} - E_{\text{lh}}$	$\lambda_{\text{elh}}^{\text{cont}}$	$\alpha_{\text{elh}}^{\text{cont}}(\hbar\omega), \alpha_{\text{elh}}^{\text{cont}}(\lambda)$	α_{LH}	$\Delta\lambda_{\text{elh}}^{\text{cont}}, \mathcal{L}_{\text{elh}}^{\text{cont}}(E)$

Tab. B.1: Nomenclature of the three major transitions.

With this simplification, the absorption expression for transversal electric (TE, electric field in QW plane) light polarization is written after performing several mathematical steps [12] as:

$$\alpha(\hbar\omega) = [\alpha_{\text{ehh}}^{\text{cont}}(\hbar\omega) + \alpha_{\text{elh}}^{\text{cont}}(\hbar\omega) + \alpha_{\text{ehh}}^{\text{ex}}(\hbar\omega)] [f_v(E_1) - f_c(E_2)] \quad (\text{B.3})$$

$$\alpha_{\text{ehh}}^{\text{cont}}(\hbar\omega) = C_0 M_b^2 \frac{1}{\pi \hbar^2 d_{\text{QW}}} \left[\frac{3}{2} m_{\text{ehh}}^r |\langle \Psi_e | \Psi_{\text{hh}} \rangle|^2 \sigma(\hbar\omega - E_{\text{ehh}}^{\text{cont}}) \right] * \mathcal{L}_{\text{ehh}}^{\text{cont}}(E) \quad (\text{B.4})$$

$$\alpha_{\text{elh}}^{\text{cont}}(\hbar\omega) = C_0 M_b^2 \frac{1}{\pi \hbar^2 d_{\text{QW}}} \left[\frac{1}{2} m_{\text{elh}}^r |<\Psi_e|\Psi_{\text{lh}}>|^2 \sigma(\hbar\omega - E_{\text{elh}}^{\text{cont}}) \right] * \mathcal{L}_{\text{elh}}^{\text{cont}}(E) \quad (\text{B.5})$$

$$\alpha_{\text{ehh}}^{\text{Ex}}(\hbar\omega) = C_0 M_b^2 \frac{4}{\pi r_{\text{Ex}}^2 d_{\text{QW}}} \left[\frac{3}{2} |<\Psi_e|\Psi_{\text{hh}}>|^2 \delta(\hbar\omega - E_{\text{ehh}}^{\text{Ex}}) \right] * \mathcal{L}_{\text{ehh}}^{\text{Ex}}(E) \quad (\text{B.6})$$

with

$$M_b^2 = \frac{m_0^2 E_g (E_g + \Delta_{\text{SO}})}{6m_e (E_g + 2\Delta_{\text{SO}}/3)} \quad (\text{B.7})$$

$$\frac{1}{m_{\text{eh}}^r} = \frac{1}{m_e} + \frac{1}{m_{\text{h}}^t} \quad (\text{B.8})$$

M_b	bulk matrix element, $\approx 4.3 \cdot 10^{-49}$ J kg for InP system [12]
r_{Ex}	effective exciton radius, ≈ 17.5 nm for this work's designs
m^r	reduced effective mass, $\approx 0.03 m_0$ for e-hh transitions in this thesis
$ <\Psi_e \Psi_{\text{hh}}> ^2$	state overlap, $ \int \Psi_e(z)\Psi_{\text{h}}(z)dz ^2 \approx 0.5 - 0.9$ in this thesis
$\sigma(E)$	step function, $=0$ for $E < 0$ and $=1$ for $E \geq 0$, no [unit]
$f_c(E), f_v(E)$	semiconductor (quasi-)Fermi functions, $0 < f_{c,v} < 1$, no [unit]

Unfortunately, linewidth broadening factors \mathcal{L} are still present in the simplified expression. Even with the incorporation of very sophisticated models, it is not possible to predict these terms as they strongly depend on characteristics of individual epitaxial materials.

Equation (B.3) is tailored to the investigated structures by adding empirical linewidth expressions determined by the comparison to measured data:

$$\alpha(\lambda) = \alpha_0 \left[\frac{\alpha_{\text{HH}}}{1 + \exp\left(\frac{\lambda - \lambda_{\text{ehh}}^{\text{cont}}}{\Delta\lambda_{\text{ehh}}^{\text{cont}}}\right)} + \frac{\alpha_{\text{LH}}}{1 + \exp\left(\frac{\lambda - \lambda_{\text{elh}}^{\text{cont}}}{\Delta\lambda_{\text{elh}}^{\text{cont}}}\right)} + \alpha_{\text{EX}} \exp\left[-\frac{1}{2} \left(\frac{\lambda - \lambda_{\text{ehh}}^{\text{Ex}}}{\Delta\lambda_{\text{ehh}}^{\text{Ex}}}\right)^2\right] \right] \quad (\text{B.9})$$

$$\alpha_0 = C_0 M_b^2 \frac{1}{\pi \hbar^2 d_{\text{QW}}} \frac{3}{2} m_{\text{ehh}}^r = 7.8 \cdot 10^3 \frac{1}{\text{cm}} \cdot \frac{5 \text{ nm}}{d_{\text{QW}}} \quad (\text{B.10})$$

$\lambda_{\text{ehh}}^{\text{cont}}, \lambda_{\text{ehh}}^{\text{Ex}}, \lambda_{\text{lh}}^{\text{cont}}$	transition wavelengths in [nm] according to Chapter A.3 and A.4
$\Delta\lambda_{\text{ehh}}^{\text{cont}}, \Delta\lambda_{\text{ehh}}^{\text{Ex}}, \Delta\lambda_{\text{lh}}^{\text{cont}}$	linewidth broadening in [nm], see Section 3.3
$\alpha_{\text{HH}}, \alpha_{\text{LH}}, \alpha_{\text{EX}}$	relative absorption amplitudes, see Section 3.3, no [unit]
α_0	absorption amplitude in $[\text{cm}^{-1}]$, summary of eqn. (B.4) to (B.6)
d_{QW}	QW width in [nm]

Appendix C

Method of Finite Differences

The finite difference method is one of the most simple procedures to solve differential equations. The definition area and boundary conditions are divided into discrete sampling points as illustrated in Fig.C.1. Thus, the differential equation turns into a matrix equation or matrix eigenvalue problem. These can be solved by numerical methods like Gaussian (LR) factorization or iterative procedures [48].

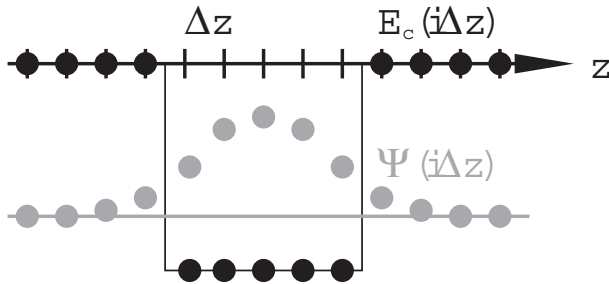


Fig. C.1: Discretization of particle wavefunction (gray) and QW potential (black).

In principle, the finite difference method is applied to all kinds of problems in arbitrary dimensions, e.g. carrier or heat transport, static or dynamic electromagnetic fields and waveguide eigenfunctions [49]. As an example, the solution of a one-dimensional Schrödinger equation in effective mass theory is discussed:

$$-\frac{\hbar^2}{2} \frac{d}{dz} \frac{1}{m(z)} \frac{d}{dz} \Psi(z) + E_c(z) \Psi(z) = E_e \Psi(z) \quad (C.1)$$

$\Psi(z)$	envelope wavefunction in $[m^{-0.5}]$, eigenfunction of the problem
E_e	absolute state energy, ≈ -0.2 eV for QWs, eigenvalue of the problem
$m(z)$	layer effective mass, $\approx 0.05 m_0$ for electrons in AlGaInAs
$E_c(z)$	layer conduction band energy level, ≈ 0 to -0.3 eV for QWs

The finite difference expression approximates derivatives by differences:

$$\frac{d}{dz}f(z) \approx \frac{f(z + \Delta z/2) - f(z - \Delta z/2)}{\Delta z} =: \frac{f_{i+1} - f_i}{\Delta z} \quad (\text{C.2})$$

This is equivalent to the original definition of derivatives for $\Delta z \rightarrow 0$. After substituting the continuous functions in equation (C.1) by point-wise defined functions, the differential equation becomes a difference equation for all i :

$$\frac{\Psi_{i+1} - \Psi_i}{m_{i+0.5}} - \frac{\Psi_i - \Psi_{i-1}}{m_{i-0.5}} - \frac{2\Delta z^2}{\hbar^2} (E_{ci} - E_e) \Psi_i = 0 \quad (\text{C.3})$$

Equation (C.3) can be expressed in matrix formulation. The matrix is symmetric and contains only the main and secondary diagonals:

$$\frac{\hbar^2}{\Delta z^2} \begin{bmatrix} \frac{1}{m_1+m_2} + \frac{1}{m_0+m_1} + \frac{\Delta z^2 m_0}{\hbar^2} E_{c1} & -\frac{1}{m_1+m_2} & 0 & 0 \\ -\frac{1}{m_1+m_2} & \frac{1}{m_2+m_3} + \frac{1}{m_1+m_2} + \frac{\Delta z^2 m_0}{\hbar^2} E_{c2} & -\frac{1}{m_2+m_3} & 0 \\ 0 & -\frac{1}{m_2+m_3} & \ddots & \ddots \\ 0 & 0 & -\frac{1}{m_3+m_4} & \ddots \\ 0 & 0 & 0 & \ddots \\ \vdots & \vdots & \vdots & \vdots \end{bmatrix} \vec{\Psi} = E_e \vec{\Psi}$$

A matrix eigenvalue problem is generated. The eigenvector $\vec{\Psi} = (\Psi_1, \Psi_2, \Psi_3, \dots, \Psi_N)$ contains the particle wavefunction at the sampling points and the corresponding eigenvalue E_e the state's energy level. The effective masses on intermediate points are averaged from their nearest neighbors. The boundary conditions $\Psi_0 = \Psi_{N+1} = 0$ for bound states are already included in the matrix expression.

The accuracy of the calculation depends on the discretization interval. For wave-like problems (2nd derivative plus function value equals zero), usually 10 to 12 cells per wavelength are sufficient.

Appendix D

Semiconductor Drift/Diffusion Equations

The distribution of carriers among different QWs of a multi-QW stack is a fundamental problem in designing active laser material. Too few QWs will result in insufficient modal gain, while too many QWs will cause inhomogeneous pumping. There is still a debate about proper simulation approaches for quantum mechanical carrier transport in literature. A quite simple variant is a semi-classical drift/diffusion and Poisson model [44]. Unknowns are the electrostatic potential φ and the two quasi-Fermi levels $E_{fc, fv}$ for conduction and valence band, respectively. In this thesis, the equations were solved by the commercially available finite element solver FEMLAB. The high nonlinearity of the equations demands a good initial guess and iterative solving.

The fundamental drift/diffusion equations are:

$$\nabla [\varepsilon_r \nabla \varphi] = \frac{e}{\varepsilon_0} (N - P - N_D + N_A) \quad (D.1)$$

$$\frac{1}{e} \nabla J_N = \underbrace{\hat{A} \frac{NP - N_i^2}{N + P + 2N_i}}_{\text{SRH}} + \underbrace{\hat{B} (NP - N_i^2)}_{\text{bimolecular}} + \underbrace{\hat{C} (N + P) (NP - N_i^2)}_{\text{Auger}} + \underbrace{\frac{c_0}{n_{\text{eff}}} \tilde{g} S}_{\text{stimulated}} \quad (D.2)$$

$$-\frac{1}{e} \nabla J_P = \underbrace{\hat{A} \frac{NP - N_i^2}{N + P + 2N_i}}_{\text{SRH}} + \underbrace{\hat{B} (NP - N_i^2)}_{\text{bimolecular}} + \underbrace{\hat{C} (N + P) (NP - N_i^2)}_{\text{Auger}} + \underbrace{\frac{c_0}{n_{\text{eff}}} \tilde{g} S}_{\text{stimulated}} \quad (D.3)$$

The unknowns are only implicitly contained in equations (D.1) to (D.3). For example, the carrier densities depend on Fermi level and band edge energy level. The currents are a function of the Fermi level's slope. All variables are explained in the next sections.

The Poisson equation (D.1) describes the static electric field distribution originating from charged particles. These are free electrons N , holes P and donor and acceptor concentrations N_D , N_A .

The drift/diffusion equations (D.2) and (D.3) for electrons and holes, respectively, originate from continuity principles. Changes in current densities J_N and J_P are caused by recombination processes as a result of particle conservation. The recombination mechanisms are mono-molecular (Shockley-Read-Hall, SRH, proportional to charge density), bimolecular (spontaneous emission, proportional to charge density squared), Auger (proportional to the third power of charge density) and stimulated recombination processes (proportional to photon density).

To solve the Poisson and drift/diffusion system of equations, the variables of equations (D.1) to (D.3) are substituted by physical expressions including only unknowns and boundary conditions (Section D.1), material parameters and auxiliary variables calculated during execution (Section D.4). Material parameters can be layer dependent as a function of the position z in growth direction (Section D.2).

- Carrier densities [26]¹:

$$N = \underbrace{N_c^{3D} e^{\frac{E_{fc}-E_c}{k_B T}}}_{N^{3D}} + \underbrace{N_c^{2D} \sum_i \ln \left(e^{\frac{E_{fc}-E_c-\tilde{E}_{ei}}{k_B T}} + 1 \right)}_{\text{Additional term in QW layers}} \quad (D.4)$$

$$P = \underbrace{N_{lh}^{3D} e^{\frac{E_{lh}-E_{fv}}{k_B T}} + N_{hh}^{3D} e^{\frac{E_{hh}-E_{fv}}{k_B T}}}_{P^{3D}} + \underbrace{N_{hh}^{2D} \sum_i \ln \left(e^{\frac{E_{hh}-\tilde{E}_{hhi}-E_{fv}}{k_B T}} + 1 \right)}_{\text{Additional term in QW layers}} \quad (D.5)$$

- Band edges [26]:

$$E_c = -e\varphi + \frac{E_g^{\text{CLAD}}}{2} + \frac{k_B T}{2} \ln \left(\frac{N_c^{\text{CLAD}}}{N_v^{\text{CLAD}}} \right) + \Delta E_c \quad (D.6)$$

$$E_{hh, lh} = -e\varphi - \frac{E_g^{\text{CLAD}}}{2} + \frac{k_B T}{2} \ln \left(\frac{N_c^{\text{CLAD}}}{N_v^{\text{CLAD}}} \right) + \Delta E_{hh, lh} \quad (D.7)$$

- Electrical current densities [26]:

$$J_N = \mu_N N^{3D} \nabla E_{fc} \quad (D.8)$$

$$J_P = \mu_P P^{3D} \nabla E_{fv} \quad (D.9)$$

- Gain and photon density [10]:

$$\tilde{g} = \max_{\lambda} \left[\sum_i \Gamma_{QWi} g_{QWi}(\lambda) \right] \quad \text{for BA laser} \quad (D.10)$$

¹3D in Boltzmann's approximation, 2D exact, use barrier CB level for QW 3D states

$$\tilde{g} = \sum_i \Gamma_{\text{QW}i} g_{\text{QW}i}(\lambda_{\text{DFB}}) \quad \text{for DFB laser} \quad (\text{D.11})$$

$$S = \frac{\Gamma \beta_{\text{sp}} \hat{B} (NP - N_i^2)}{\frac{c_0}{n_{\text{eff}}} (\tilde{g}_{\text{th}} - \tilde{g})} \quad (\text{D.12})$$

- Output power [10]:

$$P_{\text{LD}} = \hbar\omega \frac{d_{\text{QW}} l_{\text{LD}} w}{\Gamma} \frac{c_0}{n_{\text{eff}}} \tilde{\alpha}_m \quad (\text{D.13})$$

The system of equations is solved by a one-dimensional finite element method in growth direction. In principle, the model is valid for broad area lasers only. For ridge lasers, an empiric factor of 2.3 connecting ridge and active area current densities is taken into account, as the effective width of the active region is wider than the ridge itself.

Material parameters are calculated prior to execution. Dependencies of these parameters on temperature or optical field are not included in a self-consistent way. Thus, the algorithm is only suitable for low excitation conditions at room temperature. Longitudinal and transversal carrier distribution (spatial hole burning), thermal heating (roll-over) and thermal or carrier induced index change (gain guiding) is not included.

D.1 Unknowns and Boundary Conditions

The unknowns and boundary conditions of equations (D.1) to equation (D.12) are listed in Table D.1. All other terms are constants given by the layer structure or auxiliary variables.

Tab. D.1: Unknowns and boundary conditions.

Variable	Description	Unit
$\varphi(z)$	Coulomb potential	V
$E_{\text{fc}}(z)$	CB quasi-Fermi level	J
$E_{\text{fv}}(z)$	VB quasi-Fermi level	J
z_0	p-side boundary position	m
z_1	n-side boundary position	m
V_{LD}	Laser voltage ²	V
S	Photon density ³	1/m ³

The boundary condition employed describes ohmic contacts. At the contact surface, the semiconductor is in thermal equilibrium due to an infinite recombination speed. Both Fermi levels coincide and the band structure is determined by the doping concentration. This is equivalent to a bulk semiconductor in thermal equilibrium. For high doping concentrations

²boundary condition below laser threshold

³boundary condition above laser threshold

($|N_{D,A}| \gg N_i$), this yields:

$$\varphi(z_0) = \frac{k_B T}{e} \ln \left(\frac{N_i}{N_A} \Big|_{z_0} \right) + V_{LD} \quad (D.14)$$

$$E_{fc,fv}(z_0) = -e V_{LD} \quad (D.15)$$

$$\varphi(z_1) = \frac{k_B T}{e} \ln \left(\frac{N_D}{N_i} \Big|_{z_1} \right) \quad (D.16)$$

$$E_{fc,fv}(z_1) = 0 \quad (D.17)$$

For low current values, the voltage across the laser diode is chosen as the boundary condition. It is increased until the laser reaches threshold, yielding the photon density. Above threshold, the photon density acts as boundary condition and the external voltage is calculated.

D.2 Layer Dependent Input Parameters

Parameters for the different semiconductor layers are calculated by well-known semiconductor relationships. For example, the effective density of states of a two-dimensional QW is given by $N_{hh}^{QW} = m_{hh}^t k_B T / (\pi \hbar^2 d_{QW})$. They are given in Table D.2, calculated prior to execution and assumed to remain constant. In reality, there are slight changes due to coupling to temperature and optical power density. The typical values in Table D.2 are determined for intrinsic InP and a 5 nm $\text{Al}_{0.17}\text{Ga}_{0.16}\text{In}_{0.67}\text{As}$ QW ($\lambda_{PL} = 1290$ nm, embedded in an $d_{pn} = 280$ nm intrinsic region, $\varepsilon_{xx} = 0.95\%$ compressive strain) at room temperature. The parameters for other aluminum containing QW, SCH and barrier layers for unbound (3D) electrons are approximately equal to those in the AlGaInAs column. InGaAsP, InGaAs and AlGaAs layers have to be calculated separately using the equations presented in Appendix A.

Tab. D.2: Semiconductor layer parameters.

Variable	Description	Ref	Typical value	
			bulk InP	$\text{Al}_{0.17}\text{Ga}_{0.16}\text{In}_{0.67}\text{As}$ QW
$\varepsilon_r(z)$	Static permittivity	[50]	12.61	13.92
$N_D(z)$	Donor doping profile	-	$1 \cdot 10^{18} \text{ cm}^{-3}$	-
$N_A(z)$	Acceptor doping profile	-	$5 \cdot 10^{17} \text{ cm}^{-3}$	-
$N_i(z)$	Intrinsic carrier density	[26]	$8.65 \cdot 10^6 \text{ cm}^{-3}$	$6.62 \cdot 10^9 \text{ cm}^{-3}$
$N_c^{3D}(z)$	CB effective DOS	[26]	$5.63 \cdot 10^{17} \text{ cm}^{-3}$	$3.25 \cdot 10^{17} \text{ cm}^{-3}$
$N_{lh}^{3D}(z)$	LH band effective DOS	[26]	$2.51 \cdot 10^{18} \text{ cm}^{-3}$	$1.24 \cdot 10^{18} \text{ cm}^{-3}$
$N_{hh}^{3D}(z)$	HH band effective DOS	[26]	$2.74 \cdot 10^{18} \text{ cm}^{-3}$	$1.42 \cdot 10^{18} \text{ cm}^{-3}$
$N_c^{2D}(z)$	CB-QW effective DOS	[26]	-	$1.02 \cdot 10^{18} \text{ cm}^{-3}$
$N_{hh}^{2D}(z)$	HH-QW effective DOS	[26]	-	$1.69 \cdot 10^{18} \text{ cm}^{-3}$
$\Delta E_c(z)$	CB offset to cladding	[20]	0 eV	-0.1573 eV, 0.0248 eV ⁴

⁴Use barrier CB level for 3D states with lowest energy

Tab. D.2: Semiconductor layer parameters.

Variable	Description	Ref	Typical value	
			bulk InP	Al _{0.17} Ga _{0.16} In _{0.67} As QW
$\Delta E_{lh}(z)$	LH band offset to cladding	[20]	0 eV	+0.2642 eV ⁵
$\Delta E_{hh}(z)$	HH band offset to cladding	[20]	0 eV	+0.3284 eV, 0.2092 eV ⁶
$\tilde{E}_{el}(z)$	Electron confinement energy	A.3	-	0.0786 eV ⁷
$\tilde{E}_{hh1}(z)$	1st HH confinement energy	A.3	-	0.0207 eV ⁷
$\tilde{E}_{hh2}(z)$	2nd HH confinement energy	A.3	-	0.0775 eV ⁷
$\mu_N(z)$	Electron mobility	[26]	4700 cm ² /Vs	4700 cm ² /Vs ⁸
$\mu_P(z)$	Hole mobility	[25]	150 cm ² /Vs	50 cm ² /Vs ⁸
$\hat{A}(z)$	SRH recombination coeff	Fit	$5 \cdot 10^{-7}$ /s	$5 \cdot 10^{-7}$ /s
$\hat{B}(z)$	Bimolecular recombination coeff	Fit	$2.13 \cdot 10^{-10}$ cm ³ /s	$2.13 \cdot 10^{-10}$ cm ³ /s
$\hat{C}(z)$	Auger recombination coeff	Fit	$2.13 \cdot 10^{-28}$ cm ⁶ /s	$2.13 \cdot 10^{-28}$ cm ⁶ /s

References without brackets refer to the corresponding chapters in this thesis. The recombination terms are determined by the fitting procedure presented in Chapter 4.

D.3 Input Parameters for the whole Structure

Some parameters describe the layer structure as a whole. They form the boundary and optical mode parameters given in Table D.3. They are calculated prior to execution by waveguide simulations and assumed to remain constant.

Tab. D.3: Structure parameters.

Variable	Description	Ref	Typical value
Γ_{QWi}	i th QW confinement	5.1.3	1.1% (5 nm QW) 1.7% (7.5 nm QW)
n_{eff}	Waveguide effective index	7.1	3.28 (1300 nm) 3.19 (1550 nm)
E_g^{CLAD}	Cladding material (InP) bandgap	[20]	1.353 eV
N_c^{CLAD}	Cladding material CB effective DOS	[26]	$5.63 \cdot 10^{17}$ cm ⁻³
N_v^{CLAD}	Cladding material VB effective DOS	[26]	$5.25 \cdot 10^{18}$ cm ⁻³
β_{sp}	Spontaneous emission into lasing mode	[10]	0.01
\tilde{g}_{th}	Cavity modal threshold gain	[10]	47/cm ⁹
$\tilde{\alpha}_m$	Cavity modal mirror losses	[10]	32/cm ⁹

⁵(Almost) identical for QW and BAR layers due to strain effects

⁶Use barrier HH level for 3D states with highest energy

⁷Affected by bandgap shrinkage

⁸For intrinsic material at low electric fields and room temperature

⁹for 400 μ m long, uncoated BA laser, 15/cm intrinsic losses

D.4 Auxiliary Variables

The remaining auxiliary variables are shown in Table D.4. They are calculated during execution and give a better overview and physical insight into the equations. The material gain of a QW layer is given by the simplified gain equation (4.2) on page 29 and depends on the positions of both Fermi levels.

Tab. D.4: Auxiliary values calculated during execution.

Variable	Description	Unit
$N(z)$	Electron carrier density	$1/\text{m}^3$
$P(z)$	Hole carrier density	$1/\text{m}^3$
$J_N(z)$	Electrical current density due to electrons	A/m^2
$J_P(z)$	Electrical current density due to holes	A/m^2
S	Photon density	$1/\text{m}^3$
P_{LD}	Optical output power	W
g_{QWi}	Material gain of each QW	$1/\text{m}$

D.5 Algorithm

The drift/diffusion system of equations is highly nonlinear and imposes major challenges on the solution algorithm. Even with nonlinear solvers, the convergence strongly depends on the initial guess for $\varphi(z)$ and $E_{\text{fc},\text{fv}}(z)$. For equilibrium, $E_{\text{fc},\text{v}}(z) = 0$ and $\varphi(z) = \varphi(z_0)$ in the p-doped area, $\varphi(z) = \varphi(z_1)$ in the n-doped area and a linear behavior in the intermediate intrinsic region are chosen. The problem is solved in an iterative way, beginning with the equilibrium state and increasing the strength of injection step by step:

- Below threshold: increase the diode voltage V_{LD} in 0.05 V steps. Use the solutions for the potential $\varphi(z)$ and Fermi levels $E_{\text{fc},\text{fv}}(z)$ as an initial guess for the next voltage step ('parametric solving'). External current density $J = J_N(z_0) + J_P(z_0)$, optical power P_{LD} and modal gain \tilde{g} are monitored. Repeat the procedure until the modal gain \tilde{g} is close to the threshold gain \tilde{g}_{th} .
- Above threshold: increase the photon density S . Use the solutions for the potential $\varphi(z)$ and Fermi levels $E_{\text{fc},\text{fv}}(z)$ as an initial guess for the next voltage step ('parametric solving'). The modal gain $\tilde{g} = \tilde{g}_{\text{th}}$ is a so-called weak boundary condition. Diode voltage V_{LD} , optical power P_{LD} and current density J are monitored.

Appendix E

List of Symbols

A	Adachi parameter
\hat{A}	SRH recombination parameter
A_{pad}	Pad or feed line area
a_0	Lattice constant
a_c	Hydrostatic conduction band shift
a_v	Hydrostatic valence band shift
B	Adachi parameter
\hat{B}	Bimolecular recombination parameter
b	[001] shear shift
bow	Bowing parameter
C	Capacitance
C_i	(Central) intrinsic capacitance of pin-junction
C_l	Lateral intrinsic capacitance of pin-junction
C_{pad}	Bond-pad parasitic capacitance
C_{\square}	Capacitance per unit area
C'	Capacitance per unit length
C_0	Absorption constants
\hat{C}	Auger recombination parameter
c_0	Vacuum light velocity, $= 2.998 \cdot 10^8 \text{ m/s}$
c_{11}	Elastic constant
c_{12}	Elastic constant
D	Coplanar microwave waveguide stripe distance
$Disp$	Dispersion coefficient
d	Layer thickness
d_{BAR}	Barrier layer thickness
d_{BCB}	BCB passivation thickness
d_{Grat}	Grating layer thickness
d_{pn}	Intrinsic area layer thickness

d_{QW}	Quantum well layer thickness
d_{SCH}	SCH (waveguide) layer thickness
d_{sp}	Thickness of spacing layers between waveguide and DFB grating layer
d_{SUB}	Substrate thickness
E	Energy
$E_{1,2}$	Transition initial and final energy
E_{BA}	Broad area laser photon energy = $1240 \text{ eVnm}/\lambda_{\text{BA}}$
E_{c}	Energy level of conduction band edge at Γ point
E_{Ex}	Exciton binding energy
E_{ei}	Confinement energy of i th electron level relative to the center of the QW
\tilde{E}_{ei}	Confinement energy of i th electron level including bandgap shrinkage
$E_{\text{ehh}}^{\text{cont}}$	2D electron-heavy hole continuum transition energy = $1240 \text{ eVnm}/\lambda_{\text{ehh}}^{\text{cont}}$
$E_{\text{ehh}}^{\text{Ex}}$	2D electron-heavy hole exciton transition energy = $1240 \text{ eVnm}/\lambda_{\text{ehh}}^{\text{Ex}}$
$E_{\text{elh}}^{\text{cont}}$	2D electron-light hole continuum transition energy = $1240 \text{ eVnm}/\lambda_{\text{elh}}^{\text{cont}}$
$\tilde{E}_{\text{ehh}}^{\text{cont}}$	Renormalized 2D electron-heavy hole continuum transition energy
$\tilde{E}_{\text{elh}}^{\text{cont}}$	Renormalized 2D electron-light hole continuum transition energy
E_f	Fermi level for Fermi-Dirac statistic
E_{fc}	Semiconductor conduction band quasi-Fermi level
E_{fv}	Semiconductor valence band quasi-Fermi level
E_g	Bandgap at $T = 300 \text{ K}$ at Γ point
\tilde{E}_g	Renormalized Bandgap at $T = 300 \text{ K}$ at Γ point
E_{g0}	Bandgap at $T = 0 \text{ K}$ at Γ point
E_g^{CLAD}	Bandgap of laser diode cladding material
E_{hh}	Energy level of heavy hole subband edge at Γ point
E_{hhi}	Confinement energy of i th heavy hole level relative to the center of the QW
\tilde{E}_{hhi}	Confinement energy of i th heavy hole level including bandgap shrinkage
E_{lh}	Energy level of light hole subband edge at Γ point
E_{PL}	Material photoluminescence energy = $1240 \text{ eVnm}/\lambda_{\text{PL}}$
E_v	Energy level of valence band edge at Γ point
$ \vec{E} $	Electric field
$ \vec{E} _{\text{bi}}$	Built-in electric field of pin-junction
$ \vec{E} _{\text{bias}}$	Electric field due to external bias voltage
$ \vec{E} _{\text{dark}}$	Internal pin electric field without carrier generation
$ \vec{E} _{\text{scr}}$	Screening field of generated photo carriers
ER	Extinction ratio
e	Elemental charge, $= 1.602 \cdot 10^{-19} \text{ C}$
FoM	Figure of merit
f	Modulation frequency
$f(x)$	Function expression
$f_{\text{c}}(E)$	Quasi-Fermi distribution for conduction band
$f_{\text{v}}(E)$	Quasi-Fermi distribution for valence band

G	Carrier generation term
g	Material optical (power) gain
g_{QWi}	i -th QW material gain
\tilde{g}	Modal optical gain
\tilde{g}_{th}	Modal laser threshold gain
H	Magnetic field
\hbar	Planck's constant, $= 1.054 \cdot 10^{-34}$ Js
I	Current
I_{EAM}	Modulator current
I_{LD}	Laser current
I_{ph}	Photo generated current
I_{th}	Laser threshold current
i, j	Counting variable OR imaginary unit
J	Current density
J_{EAM}	Modulator current density
J_{LD}	Laser current density
J_{N}	Electric current density due to electrons
J_{P}	Electric current density due to holes
J_{th}	Laser threshold current density
k	Thermal conductivity
k_{B}	Boltzmann's constant, $= 1.381 \cdot 10^{-23}$ J/K
\vec{k}	Wave vector
\vec{k}_{t}	Transversal wave vector
\vec{k}_{z}	In growth wave vector
$\mathcal{L}(E), \mathcal{L}(\lambda)$	Line shape function
L	Self-inductivity
L'	Inductivity per length unit
L_{ridge}	Ridge inductivity
l	Length
l_{EAM}	Modulator length
l_{Grat}	Grating length
l_{pad}	Pad (feed line) length
l_{LD}	Laser length
M_{b}^2	Bulk matrix element
m_0	Free electron mass, $= 9.1095 \cdot 10^{-31}$ kg
m_{e}	Effective isotropic electron mass at Γ point
m_{hh}^{z}	Effective heavy hole in growth direction mass at Γ point
m_{hh}^{t}	Effective heavy hole transversal averaged mass at Γ point

m_{lh}^z	Effective light hole in growth direction mass at Γ point
m_{lh}^t	Effective light hole transversal averaged mass at Γ point
m^r	Reduced effective mass
m_{SO}	Effective Isotropic split-off band hole mass at Γ point
N	Electron carrier density
N_A	Acceptor doping profile
N^{3D}	Electron density in free 3D states
N_D	Donor doping profile
N_i	Semiconductor intrinsic carrier density
N^{QW}	Electron density in bound QW states
$N_{c,hh,lh}^{3D}$	Conduction / heavy / light hole band 3D effective density of states (DOS)
$N_{c,hh,lh}^{QW}$	Conduction / heavy / light hole band QW effective density of states (DOS)
$N_{c,v}^{CLAD}$	Cladding material conduction/valence band effective density of states (DOS)
n	Refractive index
n_{eff}	Waveguide effective refractive index
n_{eff}^{Ridge}	Effective index method 1D slab waveguide effective index under ridge
n_{eff}^{Side}	Effective index method 1D slab waveguide effective index to ridge side
$n_{eff,r}$	Real part of waveguide effective refractive index
$n_{eff,i}$	Imaginary part of waveguide effective refractive index
P	Optical power OR hole carrier density
P_{abs}	Absorbed optical power
P_{fiber}	Fiber coupled optical power
P_{in}	Optical power at device input
P_{LD}	Optical power emitted by laser diode
P_{out}	Optical power at device output
P_c	Hydrostatic conduction band shift
P_v	Hydrostatic valence band shift
par	Arbitrary semiconductor parameter, e.g. a_0
Q_e	Tensile/compressive valence band shift
Q	Electrical charge
q	Thermal power density source
q_{EAM}	Thermal power density source in modulator
q_{LD}	Thermal power density source in laser
R	Resistance
R_{LD}	Laser series resistance
R_l	Lateral resistance under ridge
R_{ridge}	Ridge resistance in EAM section
R_s	Source resistance
R_t	Termination resistance
r	(Power) Reflection coefficient
r^{Field}	Complex field reflection coefficient

r_f^{Field}	Complex field reflection coefficient of facet
\vec{r}, \vec{R}	Spatial position
r_{Ex}	Effective exciton radius
S	Cavity photon density
s_{11}	EAM electrical reflection scattering parameter
s_{21}	EAM electrical transmission scattering parameter
s_{eo}	EAM electro-optical transmission scattering parameter
s_{11}^{th}	Thermal self-heating of laser
s_{12}^{th}	Thermal crosstalk from modulator to laser
s_{21}^{th}	Thermal crosstalk from laser to modulator
s_{22}^{th}	Thermal self-heating of modulator
T	Temperature
t	Time
t^{Field}	Complex field transmission coefficient
V	Voltage
V_0	Diode turn-on voltage
V_{bi}	Built-in pin-junction voltage
V_{EAM}	External EAM bias voltage
V_{LD}	External laser bias voltage
V_{pp}	Modulator driver peak to peak voltage
V_{scr}	Voltage of screening field
VBO	Valence band offset at Γ point
v	Velocity
v_{ph}	Phase velocity
v_{gr}	Group velocity
v_s	Carrier saturation velocity
W	Coplanar microwave waveguide central stripe width
w	Width
w_{ridge}	Width of ridge
$w_{2\text{nd}}$	Width of 2nd mesa
x	Spatial coordinate in ridge direction
y	Transversal spatial coordinate
z	Spatial coordinate in growth direction
\mathbf{x}	Al compound concentration
\mathbf{y}	Ga compound concentration
\mathbf{z}	In compound concentration
Z	Microwave waveguide characteristic wave impedance

α	Material power absorption coefficient OR Varshni parameter
α_0	QW e-hh flat band absorption amplitude
$\alpha_{\text{ehh}}^{\text{cont}}(\hbar\omega)$	Spectral absorption contribution of electron-heavy hole continuum transition
$\alpha_{\text{ehh}}^{\text{Ex}}(\hbar\omega)$	Spectral absorption contribution of electron-heavy hole exciton transition
$\alpha_{\text{elh}}^{\text{cont}}(\hbar\omega)$	Spectral absorption contribution of electron-light hole exciton transition
α_{EX}	Relative electron-heavy hole exciton transition strength
α_{HH}	Relative electron-heavy hole continuum transition strength
α_{LH}	Relative electron-light hole continuum transition strength
$\alpha_{\text{QW}i}$	i th QW material absorption in MQW structure
α_{SUB}	Substrate absorption
α_{H}	Chirp parameter (Henry factor)
$\tilde{\alpha}$	Waveguide modal absorption
$\tilde{\alpha}_i$	Waveguide intrinsic modal scattering losses
$\tilde{\alpha}_{\text{m}}$	Laser cavity modal mirror losses
$\tilde{\alpha}_0$	Modulator modal residual absorption
β	Varshni parameter
β_{sp}	Part of spontaneous emission coupled into leasing mode
Γ	Confinement factor
$\Gamma_{\text{QW}i}$	Confinement factor of i th QW in MQW stack
Γ_{grat}	Grating confinement factor
$\gamma_{1,2,3}$	Luttinger parameter
Δ_{SO}	Split-off band distance at Γ point
ΔE_{c}	Layer conduction band offset to cladding material
ΔE_{hh}	Layer heavy hole band offset to cladding material
ΔE_{lh}	Layer light hole band offset to cladding material
Δn	Index contrast in grating or waveguide
$\Delta \bar{T}_{\text{EAM}}$	Mean temperature rise in modulator
$\Delta \bar{T}_{\text{LD}}$	Mean temperature rise in laser
$\Delta \alpha$	Material absorption change
$\Delta \tilde{\alpha}$	Modal absorption change
$\Delta \lambda$	Linewidth broadening parameter
$\Delta \lambda_{\text{ehh}}^{\text{cont}}$	Linewidth broadening of electron-heavy hole continuum transition
$\Delta \lambda_{\text{ehh}}^{\text{Ex}}$	Linewidth broadening of electron-heavy hole exciton transition
$\Delta \lambda_{\text{elh}}^{\text{cont}}$	Linewidth broadening of electron-light hole continuum transition
$\Delta \lambda_{\text{stop}}$	Spectral stop band width of DFB laser
$\delta(x)$	Phase or wave number detuning
$\delta(x)$	Dirac function, $\int \delta(x)f(x)dx = f(0)$
ε_0	Electric field constant, $= 8.854 \cdot 10^{-12}$ F/m
ε_{eff}	Effective permittivity of microwave guide, cmp. to n_{eff} for optical mode
ε_{r}	Static dielectric permittivity
$\varepsilon_{\text{r,BCB}}$	BCB Static dielectric permittivity

ε_{xx}	Biaxial strain in x-direction
ε_{yy}	Biaxial strain in y-direction
ε_{zz}	Normal strain in z-direction
Φ	Fast oscillating, lattice periodic part of wavefunction
φ	Electrostatic potential
η_d	External quantum efficiency of laser diode
η_f	Fiber coupling efficiency
η_i	Internal quantum efficiency of absorption process
κ	DFB coupling factor
λ	Free space wavelength
λ_{BA}	Broad area laser emission wavelength = $1240 \text{ eVnm}/E_{BA}$
$\lambda_{ehh}^{\text{cont}}$	2D Electron-heavy hole ground state transition wavelength = $1240 \text{ eVnm}/E_{ehh}^{\text{cont}}$
$\lambda_{ehh}^{\text{Ex}}$	2D Electron-heavy hole exciton transition wavelength = $1240 \text{ eVnm}/E_{ehh}^{\text{Ex}}$
$\lambda_{elh}^{\text{cont}}$	2D Electron-light hole ground state transition wavelength = $1240 \text{ eVnm}/E_{elh}^{\text{cont}}$
$\tilde{\lambda}_{ehh}^{\text{cont}}$	Renormalized 2D Electron-heavy hole ground state transition wavelength
$\tilde{\lambda}_{elh}^{\text{cont}}$	Renormalized 2D Electron-light hole ground state transition wavelength
λ_{DFB}	DFB laser wavelength
λ_{PL}	Material photoluminescence wavelength = $1240 \text{ eVnm}/E_{\text{PL}}$
μ_0	Magnetic field constant, $4\pi \cdot 10^{-7} \text{ H/m}$
μ_N	Electron mobility
μ_P	Hole mobility
ρ	Charge density OR specific resistance
ρ_f	Surface charge density
$\sigma(x)$	Step function, $=0 \ (x < 0)$, $=1 \ (x \geq 0)$
τ	Time constant
τ_{RC}	RC time constant
$\tau_{e,h}^{\text{esc}}$	Electron, hole QW escape time constant
ω	Angular frequency
Ψ	Slowly varying envelope function
Ψ_e	Electron envelope function
Ψ_h	Hole envelope function
Ψ_{hh}	Heavy hole envelope function
Ψ_{lh}	Light hole envelope function

Appendix F

List of Acronyms

AC	Alternating current
Al	Aluminum
As	Arsenic
BA	Broad area (laser)
Bar	Barrier
BCB	Benzocyclobutene passivation
CB	Conduction band
CW	Continuous wave
DC	Direct Current
DFB	Distributed feedback (laser)
DOS	Density of states
EAM	Electroabsorption modulator
EML	Electroabsorption modulated laser
Fig	Figure
Ga	Gallium
Gbps	Gigabit per second
HH	Heavy hole
In	Indium
LH	Light hole
Ni	Nickel
P	Phosphorus
PIN	p-doped – intrinsic – n-doped structure
PL	Photoluminescence
QCSE	Quantum-confined Stark effect
QW	Quantum well
RW	Ridge waveguide
SCH	Semi-confinement heterostructure
SCR	Space charge region
s.i.	semi-insulating (substrate)
SNR	Signal to noise ratio
SOA	Semiconductor optical amplifier
SRH	Shockley-Read-Hall (recombination)

SSMF	Standard single-mode fiber
TEM	Transversal electro magnetic (microwave waveguide)
VB	Valence band
Zn	Zinc

Appendix G

Material Data

G.1 InP

Tab. G.1: InP material parameters

Parameter	Sign	Value	Unit	Reference
Lattice Constant	a_0	$5.8697 + 2.79 \cdot 10^{-5}(T/[\text{K}] - 300)$	Å	[20]
Bandgap at T= 0K	E_{g0}	1.424	eV	[20]
Bandgap at T= 300K	E_g	1.353	eV	[20]
1st Varshni parameter	α	$0.363 \cdot 10^{-3}$	eV/K	[20]
2nd Varshni parameter	β	162	K	[20]
Split-off band distance	Δ_{SO}	0.108	eV	[20]
Electron mass	m_e	0.080	m_0	[20]
1st Luttinger parameter	γ_1	5.08	-	[20]
2nd Luttinger parameter	γ_2	1.60	-	[20]
3rd Luttinger parameter	γ_3	2.10	-	[20]
Split-off hole mass	m_{SO}	0.21	m_0	[20]
Valence band offset	VBO	-0.94	eV	[20]
Hydrostatic CB shift	a_c	-6.0	eV	[20]
Hydrostatic VB shift	a_v	-0.6	eV	[20]
[001] shear shift	b	-2.0	eV	[20]
1st elastic constant	c_{11}	1011	GPa	[20]
2nd elastic constant	c_{12}	561	GPa	[20]
Dielectric permittivity	ϵ_r	12.61	-	[50]
1st Adachi parameter	A	6.30	-	[44]
2nd Adachi parameter	B	9.40	-	[44]

G.2 GaAs

Tab. G.2: GaAs material parameters

Parameter	Sign	Value	Unit	Reference
Lattice Constant	a_0	$5.65325 + 3.88 \cdot 10^{-5}(T/[\text{K}] - 300)$	Å	[20]
Bandgap at T= 0K	E_{g0}	1.519	eV	[20]
Bandgap at T= 300K	E_g	1.422	eV	[20]
1st Varshni parameter	α	$0.5405 \cdot 10^{-3}$	eV/K	[20]
2nd Varshni parameter	β	204	K	[20]
Split-off band distance	Δ_{SO}	0.341	eV	[20]
Electron mass	m_e	0.067	m_0	[20]
1st Luttinger parameter	γ_1	6.98	-	[20]
2nd Luttinger parameter	γ_2	2.06	-	[20]
3rd Luttinger parameter	γ_3	2.93	-	[20]
Split-off hole mass	m_{SO}	0.172	m_0	[20]
Valence band offset	VBO	-0.80	eV	[20]
Hydrostatic CB shift	a_c	-7.17	eV	[20]
Hydrostatic VB shift	a_v	-1.16	eV	[20]
[001] shear shift	b	-2.0	eV	[20]
1st elastic constant	c_{11}	1221	GPa	[20]
2nd elastic constant	c_{12}	566	GPa	[20]
Dielectric permittivity	ε_r	12.91	-	[50]
1st Adachi parameter	A	6.30	-	[44]
2nd Adachi parameter	B	9.40	-	[44]

G.3 AlAs

Tab. G.3: AlAs material parameters

Parameter	Sign	Value	Unit	Reference
Lattice Constant	a_0	$5.6611 + 2.90 \cdot 10^{-5}(T/[\text{K}] - 300)$	Å	[20]
Bandgap at T= 0K	E_{g0}	3.099	eV	[20]
Bandgap at T= 300K	E_g	3.003	eV	[20]
1st Varshni parameter	α	$0.885 \cdot 10^{-3}$	eV/K	[20]
2nd Varshni parameter	β	530	K	[20]
Split-off band distance	Δ_{SO}	0.28	eV	[20]
Electron mass	m_e	0.15	m_0	[20]
1st Luttinger parameter	γ_1	3.76	-	[20]
2nd Luttinger parameter	γ_2	0.82	-	[20]
3rd Luttinger parameter	γ_3	1.42	-	[20]
Split-off hole mass	m_{SO}	0.28	m_0	[20]
Valence band offset	VBO	-1.33	eV	[20]
Hydrostatic CB shift	a_c	-5.64	eV	[20]
Hydrostatic VB shift	a_v	-2.47	eV	[20]
[001] shear shift	b	-2.3	eV	[20]
1st elastic constant	c_{11}	1250	GPa	[20]
2nd elastic constant	c_{12}	534	GPa	[20]
Dielectric permittivity	ϵ_r	10.06	-	[50]
1st Adachi parameter	A	25.30	-	[44]
2nd Adachi parameter	B	-0.80	-	[44]

G.4 InAs

Tab. G.4: InAs material parameters

Parameter	Sign	Value	Unit	Reference
Lattice Constant	a_0	$6.0583 + 2.74 \cdot 10^{-5}(T/[\text{K}] - 300)$	Å	[20]
Bandgap at T= 0K	E_{g0}	0.417	eV	[20]
Bandgap at T= 300K	E_g	0.3583	eV	[20]
1st Varshni parameter	α	$0.276 \cdot 10^{-3}$	eV/K	[20]
2nd Varshni parameter	β	93	K	[20]
Split-off band distance	Δ_{SO}	0.39	eV	[20]
Electron mass	m_e	0.026	m_0	[20]
1st Luttinger parameter	γ_1	20	-	[20]
2nd Luttinger parameter	γ_2	8.5	-	[20]
3rd Luttinger parameter	γ_3	9.2	-	[20]
Split-off hole mass	m_{SO}	0.14	m_0	[20]
Valence band offset	VBO	-0.59	eV	[20]
Hydrostatic CB shift	a_c	-5.08	eV	[20]
Hydrostatic VB shift	a_v	-1.00	eV	[20]
[001] shear shift	b	-1.8	eV	[20]
1st elastic constant	c_{11}	832.9	GPa	[20]
2nd elastic constant	c_{12}	452.6	GPa	[20]
Dielectric permittivity	ε_r	15.15	-	[50]
1st Adachi parameter	A	5.14	-	[44]
2nd Adachi parameter	B	10.15	-	[44]

G.5 Bowing Parameter

Tab. G.5: Ternary bowing parameters

Material system	Parameter	Bowing parameter	Reference
Al_xGaAs	E_{g0}	$-0.127 + 1.310x$	[20]
AlInAs	E_{g0}	0.700	[20]
	Δ_{SO}	0.15	[20]
	m_e	0.049	[20]
	VBO	-0.64	[20]
	a_c	-1.4	[20]
GaInAs	E_{g0}	0.477	[20]
	Δ_{SO}	0.15	[20]
	m_e	0.0091	[20]
	m_{hh}^z	-0.145	[20]
	m_{lh}^z	0.0202	[20]
	VBO	-0.38	[20]
	a_c	2.61	[20]

Publications

M. Peschke, T. Knoedl, and B. Stegmüller, "Simulation and design of an active MQW layer with high static gain and absorption modulation," in *Proc. IEEE/LEOS 3rd International Conference on Numerical Simulation of Semiconductor Optoelectronic Devices*, Oct. 14-16, pp. 15-16, 2003

B. Stegmüller, C. Hanke, T. Knoedl, M. Peschke, B. Saravanan, P. Garlach, and R. Schreiner, "Integrated DFB laser electro-absorption modulator based on identical MQW-double-stack active layer for high-speed modulation beyond 10 Gbit/s," in *Proc. IPRM Conference*, May. 31, pp. 236-238, 2004

C. Hanke, T. Knoedl, B. Saravanan, and M. Peschke, "Investigation of the high-frequency performance of monolithic integrated laser-modulators," in *Proc. SODC 04 Conference*, Mar. 21-30, 2004

T. Knoedl, C. Hanke, B. Saravanan, M. Peschke, R. Schreiner, and B. Stegmüller, "Integrated 1.3 μm InGaAlAs-InP laser-modulator with double-stack MQW layer structure," in *Proc. SPIE Conference Photonics Europe*, Apr. 26, pp. 1-7, 2004

M. Peschke, P. Gerlach, B. Saravanan, and B. Stegmüller, "Thermal crosstalk in integrated laser-modulators," *IEEE Photon. Technol. Lett.*, Vol. 16, No. 11, pp. 2508-2510, 2004

M. Peschke, B. Saravanan, C. Hanke, T. Knoedl, and B. Stegmüller, "Investigation of the capacitance of integrated DFB-EAMs with shared active layer for 40 GHz bandwidth," in *Proc. IEEE LEOS 2004*, Nov. 6-11, pp. 673-674, 2004

T. Knoedl, C. Hanke, B. Saravanan, M. Peschke, R. Macaluso, and B. Stegmüller, "40 GHz monolithic integrated 1.3 μm InGaAlAs-InP laser-modulator with double stack MQW layer structure," in *Proc. IEEE LEOS 2004*, Nov. 6-11, pp. 675-676, 2004

P. Gerlach, M. Peschke, and R. Michalzik, "High-frequency performance optimization of DFB laser integrated electroabsorption modulators," in *Proc. Semiconductor and Integrated Opto-Electronics Conference, SIE 2004*, Apr. ?, pp. ?-?, 2004

P. Gerlach, M. Peschke, C. Hanke, B. Saravanan, and R. Michalzik, "High-frequency analysis of laser-integrated lumped electroabsorption modulators," *IEE Proceedings Optoelectronics*, Vol. 152, No. ?, pp. ?, 2005

P. Gerlach, M. Peschke, B. Saravanan, T. Knoedl, C. Hanke, B. Stegmüller, and R. Michalzik, "40 Gbit/s operation of laser-integrated electroabsorption modulator using identical InGaAlAs

quantum wells,” in *Proc. 17th Indium Phosphide and Related Materials Conference, IPRM 2005*, submitted

P. Gerlach, M. Peschke, T. Knoedl, B. Saravanan, C. Hanke, B. Stegmüller, and R. Michalzik, “Complex coupled distributed feedback laser monolithically integrated with electroabsorption modulator at 1300 nm wavelength,” in *Proc. Conference on Lasers and Electro-Optics, CLEO 2005*, submitted

B. Saravanan, C. Hanke, T. Knoedl, M. Peschke, R. Macaluso, and B. Stegmüller, “Integrated InGaAlAs/InP laser-modulator using an identical multiple quantum well active layer,” in *Proc. SPIE 2005, Photonics West, San Jose, USA*, Jan. 22-27, 2005

References

- [1] K.-J. Ebeling, *Integrated Optoelectronics*. Berlin: Springer Verlag, 2006.
- [2] M.-C. Amann, *Tunable Laser Diodes*. 685 Canton Street, Norwood, MA 02062: Artech House, Inc., 1998.
- [3] A. Ramakrishnan, G. Steinle, D. Supper, C. Degen, and G. Ebbinghaus, “Electrically pumped 10 Gbit/s MOVPE grown monolithic 1.3 μm VCSEL with GaInNAs active region,” *Electron. Lett.*, vol. 38, no. 7, pp. 322–324, 2002.
- [4] K. Takagi, A. Shirai, Y. Tatsuoka, C. Watatani, T. Ota, T. Takiguchi, T. Aoyagi, T. Nishimura, and N. Tomita, “120° 10 Gb/s uncooled direct modulated 1.3 μm Al-GaInAs MQW DFB laser diodes,” *IEEE Photon. Technol. Lett.*, vol. 16, no. 11, pp. 2415–2417, 2004.
- [5] M. Meliga, C. Coriasso, and R. Paoletti, “Uncooled lasers for datacom and telecom applications,” in *LEOS-04*, Puerto Rico, Nov. 7-11 2004, pp. 92–93.
- [6] K. Tsuzuki, T. Ishibashi, T. Ito, S. Oku, Y. Shibata, R. Iga, Y. Kondo, and Y. Tohmori, “A 40 Gbit/s InP-based n-i-n mach-zehnder modulator with a π -voltage of 2.2 V,” *Electron. Lett.*, vol. 39, no. 20, pp. 1464–1466, 2003.
- [7] R. Lewen, S. Irmscher, U. Westergren, L. Thylen, and U. Eriksson, “Segmented transmission-line electroabsorption modulators,” *J. Lightwave Tech.*, vol. 22, no. 1, pp. 172–178, 2004.
- [8] H. Fukano, T. Yamanaka, M. Tamura, H. Nakajima, Y. Akage, Y. Kondo, and T. Saitoh, “40 Gbit/s electro absorption modulators with 1.1 V driving voltage,” *Electron. Lett.*, vol. 40, no. 18, pp. 1144–1146, 2004.
- [9] A. Ramdane, F. Devaux, N. Souli, D. Delprat, and Ougazzaden, “Monolithic integration of multi-quantum-well lasers and modulators for high-speed transmission,” *J. of Sel. Topics in Quantum Electron.*, vol. 2, no. 2, pp. 326–335, 1996.
- [10] L. Coldren and S. Corzine, *Diode Lasers and Photonic Integrated Circuits*. New York, NY 605 Third Avenue, USA: Wiley, 1995.
- [11] D. Miller, D. Chemla, T. Damen, A. Gossard, W. Wiegmann, T. Wood, and C. Burrus, “Electrical field dependence of optical absorption near the bandgap of quantum well structures,” *Phys. Rev. B*, vol. 32, no. 2, pp. 1043–1060, 1985.
- [12] S. L. Chuang, *Physics of Optoelectronic Devices*. New York, NY 605 Third Avenue, USA: Wiley, 1995.
- [13] H. Kuchling, *Taschenbuch der Physik*. Fachbuchverlag Leipzig, 2002.

- [14] M. R. Gokhale, P. V. Studenkov, J. Ueng-McHale, J. Thomson, J. Yao, and J. van Saders, "Uncooled, 10 Gb/s 1310nm electroabsorption modulated laser," in *Post-deadline paper (PD-42) OFC*, ASIP Inc, 25 World Fair Drive, Somerset, NJ 08873, 2003.
- [15] F. Koyama, K. Y. Liou, A. G. Dentai, G. Raybon, and C. A. Burrus, "GaInAs / GaInAsP strained quantum well monolithic electroabsorption modulator / amplifier by lateral bandgap control with non planar substrates," *Electron. Lett.*, vol. 29, no. 24, pp. 2104–2106, 1993.
- [16] K. Nakamura, S. Oshiba, and H. Horikawa, "Buried heterostructure DFB laser integrated with ridge waveguide electroabsorption modulator with over 20 GHz bandwidth," in *Proceedings of ECOC (Conference Publication No. 448)*, 1997, pp. 175–178.
- [17] M. Aoki, M. Suzuki, H. Sano, T. Kawano, T. Ido, T. Taniwatari, K. Uomi, and A. Takai, "InGaAs / InGaAsP MQW electroabsorption modulator integrated with a DFB laser fabricated by bandgap energy control selective area MOCVD," *IEEE J. Quantum Electron.*, vol. 29, pp. 2088–2096, 1993.
- [18] J. Barton, M. Dummer, A. Tauke-Pedretti, E. Skogen, J. Raring, M. Sysak, M. Masanovic, L. Johansson, and L. Coldren, "Simulation and design of an active MQW layer with high static gain and absorption modulation," in *LEOS-04*, Puerto Rico, Nov. 7-11 2004, pp. 169–170.
- [19] B. Stegmüller, M. Schier, F. Kunkel, and J. Rieger, "Monolithic integrated DFB laser with electroabsorption modulator by identical active layer structure composed of two different QW types," in *16th IEEE Intern. Semicon. Laser Conf. Proceedings TuE42*, Nara, Japan, Oct. 4-8 1998, pp. 177–178.
- [20] I. Vurgaftman and J. R. Meyer, "Band parameters for III-V compound semiconductors and their alloys," *J. Appl. Phys.*, vol. 89, no. 11, pp. 5815–5875, 2001.
- [21] G. B. Stringfellow, *Organometallic Vapor-Phase Epitaxy*. 1250 Sixth Avenue, San Diego, CA 92101: Academic Press, 1989.
- [22] W. Chow and S. Koch, *Semiconductor-laser fundamentals*. Berlin Heidelberg: Springer-Verlag, 1999.
- [23] P. Bradley, C. Rigo, and A. Stano, "Carrier induced transient electric fields in a p-i-n InP-InGaAs multiple QW modulator," *IEEE J. Quantum Electron.*, vol. 32, no. 1, pp. 43–52, 1996.
- [24] B. Saravanan, private communication at Infineon Technologies, CPR PH, Munich, Germany, 2003-2005.

- [25] J. Piprek, J. White, and A. Springthorpe, "What limits the maximum output power of long-wavelength AlGaInAs/InP laser diodes?" *IEEE J. Quantum Electron.*, vol. 38, no. 9, pp. 1–7, 2002.
- [26] S. M. Sze, *Physics of Semiconductor Devices*. New York, NY 605 Third Avenue, USA: Wiley, 1981.
- [27] A. Egorov, D. Bernklau, B. Borchert, S. Illek, D. Livshits, A. Rucki, M. Schuster, A. Kaschner, A. Hoffmann, G. Dumitras, A. Amann, and H. Riechert, *J. Cryst. Grow.*, no. 545, pp. 227–228, 2001.
- [28] A. Ramakrishnan, *MOVPE Wachstum und Charakterisierung von (GaIn)(NAs)-basierenden Heterostrukturen für langwellige Halbleiterlaserdioden*. to be published, 2005.
- [29] B. Hakki and T. Paoli, "Gain spectra in GaAs double heterostructure injection lasers," *J. Appl. Phys.*, vol. 46, no. 3, pp. 1299–1306, 1975.
- [30] J. Carroll, J. Whiteaway, and D. Plumb, *Distributed Feedback Semiconductor Lasers*. PO Box 10, Washington 98227-0010: SPIE Press, 1998.
- [31] C. Degen, private communication at Infineon Technologies, COM FO, Munich, Germany, 2004.
- [32] R. Schreiner, P. Nagele, M. Korbl, A. Groning, J. Gentner, and H. Schweizer, "Monolithically integrated tunable laterally coupled distributed-feedback lasers," *IEEE Photon. Technol. Lett.*, vol. 13, no. 12, pp. 1277–1279, 2001.
- [33] B. Stegmüller and C. Hanke, "Integrated 1.3 μm DFB laser electroabsorption modulator based on identical MQW double-stack active layer with 25 GHz modulation performance," *IEEE Photon. Technol. Lett.*, vol. 15, no. 8, pp. 1029–1031, 2003.
- [34] S. Chen, J. Maehnss, and H. Unger, "Scattering losses of optical waveguides due to edge imperfections," *AEU*, vol. 43, no. 6, pp. 400–404, 1989.
- [35] *ITU-T*, ITU Std. G.959.1, 2001.
- [36] *ITU-T*, ITU Std. G.952.A-D.
- [37] M. Pallec, C. Kazmierski, E. Vergnol, S. Perrin, J. Provost, P. Doussiere, G. Glastre, D. Carpentier, and S. Fabre, "New integrated buried laser-ridge modulator with identical active layer," *IEEE Photon. Technol. Lett.*, vol. 15, no. 3, pp. 362–364, 2003.
- [38] P. Gerlach, private communication at University of Ulm, Ulm, Germany, 2003-2005.

- [39] S. Sivoththaman, R. Jeyakumar, L. Ren, and A. Nathan, "Characterization of low permittivity (low-k) polymeric dielectric films for low temperature device integration," *J. Vac. Sci. Technol.*, vol. 20, no. 3, pp. 1149–1153, 2002.
- [40] R. Collin, *Foundations for Microwave Engineering*. 445 Hoes Lane, 1331 Piscataway, NJ, USA: IEEE Press, 2001.
- [41] C. Hanke, private communication at Infineon Technologies, CPR PH, Munich, Germany, 2003-2005.
- [42] M. Suzuki, H. Tanaka, H. Taga, S. Yamamoto, and Y. Matsushima, " $\lambda/4$ shifted DFB laser / electroabsorption modulator integrated light source for multigigabit transmission," *Trans. on Lightwave Tech.*, vol. 10, no. 1, pp. 90–95, 1992.
- [43] S. Murata, H. Nakada, and T. Abe, "Theoretical and experimental evaluation of the effect of adding a heat bypass structure to a laser diode array," *Jpn. J. Appl. Phys.*, vol. 32, no. 3A, pp. 1112–1119, 1993.
- [44] J. Piprek, *Semiconductor Optoelectronic Devices*. San Diego, California 92101-4495, USA: Academic Press, 2003.
- [45] A. Uskov, J. Karin, R. Nagarajan, and J. Bowers, "Dynamics of carrier heating and sweepout in waveguide saturable absorbers," *J. of Sel. Topics in Quantum Electron.*, vol. 1, no. 2, pp. 552–561, 1995.
- [46] M. Koch, *Dynamik von monolithisch integrierten Halbleiter Laser-Modulator-Verstaerkern*. Munich: Herbert Utz Verlag, 1999.
- [47] M. P. C. M. Krijn, "Heterojunction band offsets and effective masses in III-V quaternary alloys," *Semicond. Sci. Technol.*, vol. 6.
- [48] I. N. Bronstein and K. A. Semendyayev, *Handbook of Mathematics*. Springer-Verlag Telos.
- [49] J. Strikwerda, *Finite Differences And Partial Differential Equations*. Society for Industrial and Applied Mathematic; 2nd edition.
- [50] O. Madelung, *Landolt-Bornstein: Intrinsic properties of group IV elements and III-V, II-VI and I-VII compounds*. Berlin: Springer Verlag, 1982.

Curriculum Vitae

10/13 1976	Born in Mutlangen, Germany
09/83 – 08/87	Grauleshof Elementary School in Aalen, Germany
09/87 – 07/96	Theodor-Heuss High School in Aalen, Germany (degree: Abitur)
09/96 – 09/97	Alternative national service
10/97 – 04/02	Electrical Engineering Diploma (M.Sc. equivalent) at University of Ulm, Germany
06/02 – 03/05	Ph.D. at Optoelectronics department, University of Ulm, Germany and Infineon Technologies AG, Munich, Germany
since 04/05	Rohde & Schwarz GmbH, Munich, Germany
10/00 – 02/01	Optoelectronics department, University of Ulm, Germany Simulation on vertical laser diodes (VCSELs)
04/00 – 07/00	Tutor on ‘Electromagnetic fields & waves’
10/99 – 02/00	Tutor on ‘Signals & Systems’
04/99 – 07/99	Tutor on ‘General Electric Engineering I’
05/01 – 09/01	Fiber-Optics Communication Department, Infineon Technologies AG, Munich, Germany (internship)

Acknowledgments

First of all, I would like to express my gratitude to my girlfriend Marlis and the friends in Munich for providing me with the essential recreation time and all the other pleasures besides my Ph.D. work.

I am very much indebted to Prof. Dr. K.-J. Ebeling for giving me the possibility to perform this work under his supervision.

Naturally, I owe a lot to everybody at former Infineon Technologies Corporate Research and Communication Fiber Optics and at the University of Ulm. For scientific help and discussion, I would like to specifically thank my tutor Bernhard Stegmüller. The gain in experience during the last three years would have been marginal without the excellent measurement results and valuable discussions with Brem Kumar Saravanan, Philipp Gerlach, Christian Hanke and Thomas Wenger, formerly known as Thomas Knödl. The semiconductor material was provided by Josef Rieger, Michael Popp and Jörg Adler and the sophisticated chip technology was performed by the careful hands of Thomas Wenger and Roberto Macaluso. My measurement setups would still be in the workshop without the electrical and mechanical tips of Harald “Harry” Hedrich and Christian Degen. I would like to thank Henning Riechert for his administration efforts. Without them, it would have been impossible to keep up work during the turbulent times.

On the publication side, I am very grateful to Bernhard Stegmüller and Thomas Wenger for editing many publication drafts and Brem Kumar Saravanan, Mr. Colin Newberry, Thomas Wenger, Arun Ramakrishnan and Christian Hanke for helping me weed out the errors in my manuscript and thesis.

Finally, I would like to acknowledge the interesting debates with Robert Averbeck, Christian Giuliani, Marc Ilzhöfer, Christof Jalics, Rainer Michalzik, Jürgen Müller, Arun Ramakrishnan, Gunther Steinle and Daniel Supper to name only a few.

This work is dedicated to Bernhard Stegmüller.